Unsteady-state catalytic systems for direct CO_2 capture and reduction

（直接 CO_2 回収・還元に有効な非定常触媒反応プロセスの開発）

Shinta Miyazaki

Graduate School of Chemical Sciences and Engineering
Hokkaido University

2025

Table of contents

Chapter 1

General Introduction

1.1 Environmental impact of CO_2 emission

Carbon dioxide (CO_2), one of the main constituents of greenhouse gases, is widely considered to be the primary driver of global warming and climate change. CO_2 accounts for approximately 76% of global greenhouse gases emissions, mainly from the usage of fossil fuels and industrial processes.[1]

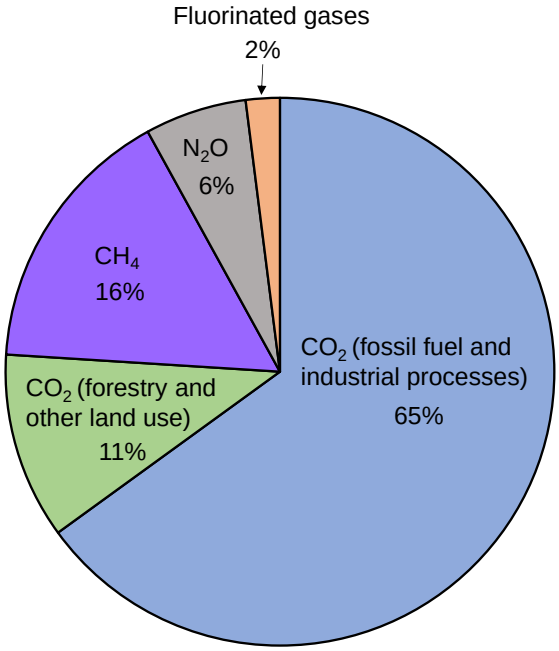

Figure 1. Global anthropogenic greenhouse gas emission by group of gases. Based on data from 2010. Source : IPCC 5th assessment report (2014).

The Paris Agreement has called on nations to limit global warming to well below 2°C, preferably 1.5 °C compared to pre-industrial levels. Anthropogenic CO_2 emission has been rising exponentially ever since the dawn of the industrial revolution. According to the special report on global warming of the Intergovernmental Panel on Climate Change (IPCC), human activities are estimated to have caused approximately 1.0 °C of global warming above pre-industrial levels, and is likely to reach 1.5 °C if the rate of increasing follows the current trajectory.[2] Therefore, the common consensus is that the global carbon emission has to be greatly reduced before reaching a point of no return in order to prevent catastrophic climate disaster that will potentially threaten the very existence of human species.

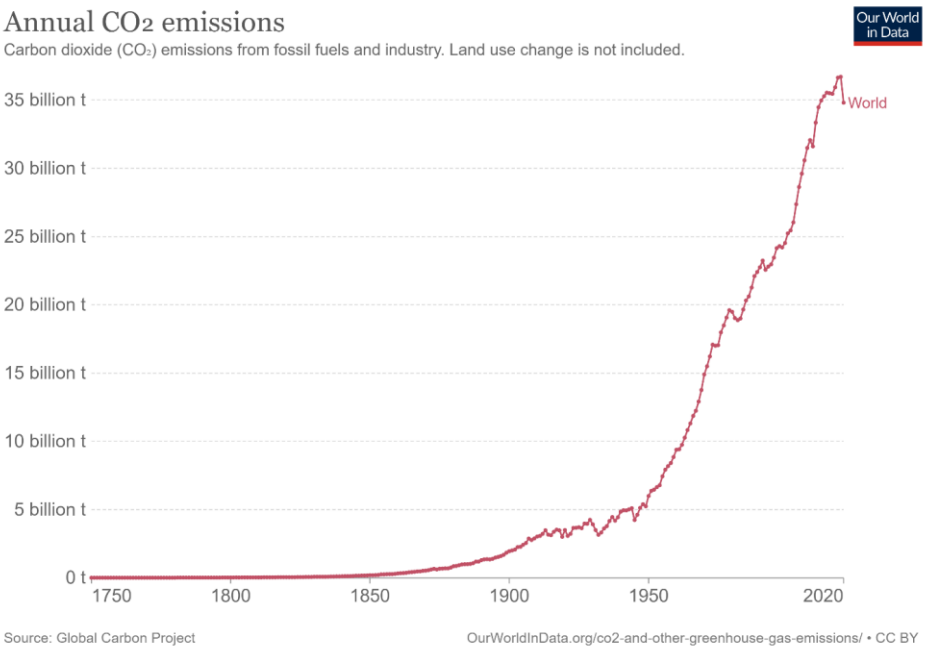

Figure 2. Annual production-based emissions of CO_2. Data from 1750 to 2021 is shown. Source: Hannah Ritchie, Max Roser and Pablo Rosado (2020) - "CO_2 and Greenhouse Gas Emissions". Published online at OurWorldInData.org. Retrieved from: 'https://ourworldindata.org/co2-and-other-greenhouse-gas-emissions'.

1.2 Carbon capture, utilization, and storage (CCUS)

Carbon capture and sequestration, or more commonly known as carbon capture and storage (CCS),[3–10] together with carbon capture and utilization (CCU)[11–19] have become increasingly important for the reduction of carbon emission. CCS technologies involve mainly 3 steps: CO_2 capture, transportation, and storage. In essence, CO_2 is captured from point sources with high carbon emissions such as power plants and industrial plants, and is transported mainly using pipelines to a suitable geological site for permanent storage. However, there are major issues associated with CCS technology that have to be solved for it to become mainstream. From an economic point of view, the deployment of CCS infrastructure requires high capital investment for something that offers virtually little to no profitability, due to the fact that permanent storage of CO_2 itself does not offer much in terms of business opportunity. Moreover, on the technical aspect, CCS is not always a viable option due to geographical constraints, since finding a suitable storage site is a challenging task.[20,21]

Amidst the ever-growing concern on climate change and depletion of fossil resources, CCU technology has garnered broad attention in both academic and industrial sectors due to the prospect of converting CO_2 into valuable products such as fuels or chemicals, while simultaneously contributing to climate change mitigation. The implementation of CO_2 as C_1 source in the petrochemical industries as an alternative to non-renewable fossil feedstock is

promising for the realization of a closed carbon cycle, and it is potentially more profitable than CCS due to the fact that value-added products can be sold commercially. Although it may sound like CCU is the "dream" technology to reduce CO_2 emissions, converting CO_2 into various products is a challenging task as the process is extremely energy intensive due to the high thermodynamic stability of CO_2 ($\Delta_f H^\circ_{298K}$ = -393.47 kJ mol^{-1}). Furthermore, at current stage, the largest scale chemical utilization of CO_2 is for the production of urea, which consumes approximately 140 Mt CO_2 yr^{-1}.[18] This is merely a drop in the ocean when compared to the annual CO_2 emission of more than 30 Gt CO_2 yr^{-1} (*vide infra*) in current era. Nevertheless, effective utilization of CO_2 as a carbon feedstock remains a highly attractive prospect for truly enabling a sustainable future, and both CCS and CCU can be integrated and developed in tandem to achieve this goal.

1.3 Catalytic hydrogenation of CO_2

Utilization of CO_2 as a feedstock for the production of chemicals and fuels requires a reduction process to turn CO_2 into various oxygenates and hydrocarbons. Catalytic hydrogenation of CO_2 has been studied extensively because hydrogenation process is arguably the most practical method for CO_2 conversion; the process is straightforward and effective when compared to other methods such as photochemical or electrochemical conversion, and the process is essentially carbon-neutral on the premise that H_2 originates from renewable energy sources (i.e., green hydrogen).[22–29] Furthermore, effective utilization of H_2 is also in line with the concept of "Hydrogen Society" as advocated by the Government of Japan.[30–33]

The synthesis of value-added products via CO_2 hydrogenation follows several possible upgrade pathways as shown in **Figure 3**. Considerable progress has been made in the research for CO_2 hydrogenation to C_1 products. Among them, CO_2 hydrogenation to methanol[34–41] has received widespread attention owing to the concept of "methanol economy" as proposed by the late Nobel prize laureate, George A. Olah.[42] Methanol, as the simplest alcohol, is one of the most important commodity chemicals in the world. Methanol is used as a precursor to many other important chemicals such as formaldehyde, acetic acid, and methyl methacrylate. Methanol can also be used for the production of synthetic fuels such as ethylene and propylene via the methanol-to-hydrocarbons (MTH) process,[43–47] or employed as a fuel itself by mixing with gasoline. Additionally, methanol can be converted to dimethyl ether (DME), a clean fuel that is non-toxic and non-corrosive, via dehydration.[48–51] Similar to methanol, DME is also an important building block for the production of many commonly used

chemicals such as methyl acetate, dimethyl sulphate, and can also be converted to light olefins and gasoline. Therefore, the direct synthesis of DME via CO_2 hydrogenation has also been studied alongside CO_2-to-methanol.

CO_2 hydrogenation to higher alcohols, especially ethanol, have also been gaining attention lately,[52–58] albeit to a lesser extent than CO_2-to-methanol as ethanol synthesis is a far more challenging process which requires C−C coupling. The same could be said about Fischer-Tropsch (FT) synthesis using CO_2 to produce synthetic fuels,[59–64] which usually occurs in parallel with CO_2 hydrogenation to higher alcohols, and as a consequence, lowering the selectivity of the desired product(s). For these processes, the ability to maintain a high yield and selectivity remains a daunting task, and more studies are needed for these technologies to become viable.

Another classical example of CO_2 hydrogenation is methanation reaction, also known as the Sabatier reaction.[65–69] Since methane is the primary component of natural gas, there was a growing interest in CO_2 methanation as a way to produce synthetic natural gas (SNG) in the past. In recent years however, against the backdrop of shale revolution in the USA, the synthesis of methane via CO_2 hydrogenation simply does not make much sense economically, leading to the diminishing of interest in large scale production of SNG.

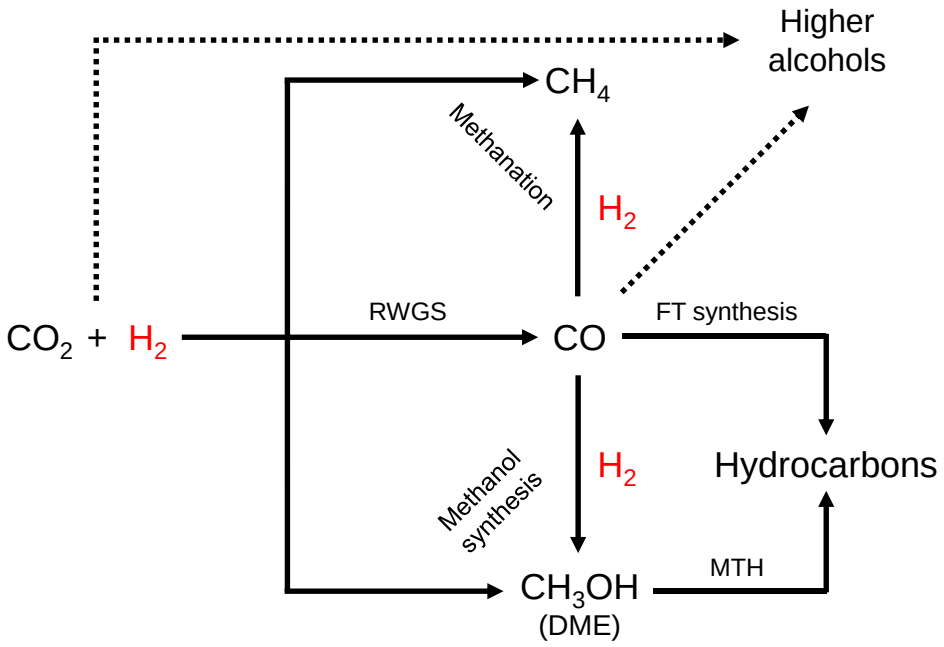

Figure 3. Various pathway for the hydrogenation of CO_2 into value-added products.

1.4 Unsteady-state catalytic systems for CO_2 utilization

Dual functional materials (DFMs) represent a promising approach to enhance the energy efficiency of carbon capture and utilization (CCU) by CO_2 capture and reduction into a single operation, which is one of the unsteady-state catalytic systems. By leveraging waste heat and reducing the complexity of operations, CCR offers potential economic and environmental benefits over conventional CCU processes. DFMs, such as calcium oxide combined with methanation catalysts, can produce value-added products like methane, carbon monoxide, or methanol. However, the practical implementation of CCR requires addressing challenges related to material performance, energy efficiency, and process optimization.

The success of CCR depends on identifying optimal DFM operating conditions, such as balancing temperature swings and isothermal processes. While temperature swings can enhance CO_2 capture and product yield, they impose energy penalties and may degrade materials. Current research highlights that the hydrogen-to-CO_2 ratio significantly impacts the thermodynamics and kinetics of CCR, with high ratios often being inefficient due to the wastage of renewable hydrogen. Furthermore, the choice of product—methane, carbon monoxide, or methanol—must align with the operational context, as each has distinct advantages and challenges.

Advancing DFM technology also requires deeper insights into the adsorbent-catalyst interface and the reaction mechanisms. High temperatures (e.g., ~300 °C) are necessary for effective CO_2 hydrogenation, which poses challenges for material durability, especially for components like calcium oxide prone to sintering.

To accelerate DFM research and implementation, the scientific community must establish consistent benchmarking standards and reporting practices. Clear definitions of performance metrics, such as CO_2 conversion and hydrogen utilization, are essential to facilitate meaningful comparisons across studies. Additionally, incorporating realistic industrial conditions, such as gas composition and temperature, will bridge the gap between laboratory research and practical applications, ultimately driving the commercialization of DFMs for sustainable carbon utilization.

1.5 Thesis outline

This thesis focuses on several unsteady-state catalytic systems for CO_2 utilization, which have the potential to contribute to a carbon-neutral society. This thesis will be divided into the following chapters:

Chapter 2: CO_2 capture and hydrogenation to CO over Pt-based and Cs-based DFMs.

Chapter 3: CO_2 capture and hydrogenation to CH_4 over Ni-based DFMs.

Chapter 4: Unsteady-state tandem catalytic systems for CO_2 capture and reduction.

Chapter 5: CO_2 reforming by CH_4 via chemical looping technology

1.6 References

(1) Eickemeier, P.; Schlömer, S.; Farahani, E.; Kadner, S.; Brunner, S.; Baum, I.; Kriemann, B. *IPCC, 2012: Summary for Policymakers*; 2019. https://doi.org/10.4324/9781351201117-15.

(2) Masson-Delmotte, V. . P. Z. H.-O. P. D. R. J. S. P. R. S. A. P. W. M.-O. C. P. R. P. S. C. J. B. R. M. Y. C. X. Z. M. I. G. E. L. T. M. M. T. and T. W. (eds. . Summary for Policymakers. In Global Warming of 1.5°C: IPCC Special Report on Impacts of Global Warming of 1.5°C above Pre-Industrial Levels in Context of Strengthening Response to Climate Change, Sustainable Development, and Efforts to Eradicate Poverty (. *Glob. Warm. 1.5°C* **2018**, 1–24.

(3) Bui, M.; Adjiman, C. S.; Bardow, A.; Anthony, E. J.; Boston, A.; Brown, S.; Fennell, P. S.; Fuss, S.; Galindo, A.; Hackett, L. A.; et al. Carbon Capture and Storage (CCS): The Way Forward. *Energy Environ. Sci.* **2018**, *11* (5), 1062–1176. https://doi.org/10.1039/c7ee02342a.

(4) Anderson, S.; Newell, R. Prospects for Carbon Capture and Storage Technologies. *Annu. Rev. Environ. Resour.* **2004**, *29*, 109–142. https://doi.org/10.1146/annurev.energy.29.082703.145619.

(5) Boot-Handford, M. E.; Abanades, J. C.; Anthony, E. J.; Blunt, M. J.; Brandani, S.; Mac Dowell, N.; Fernández, J. R.; Ferrari, M. C.; Gross, R.; Hallett, J. P.; et al. Carbon Capture and Storage Update. *Energy Environ. Sci.* **2014**, *7* (1), 130–189. https://doi.org/10.1039/c3ee42350f.

(6) Lau, H. C.; Ramakrishna, S.; Zhang, K.; Radhamani, A. V. The Role of Carbon Capture and Storage in the Energy Transition. *Energy and Fuels* **2021**, *35* (9), 7364–7386. https://doi.org/10.1021/acs.energyfuels.1c00032.

(7) Gibbins, J.; Chalmers, H. Carbon Capture and Storage. *Energy Policy* **2008**, *36* (12), 4317–4322. https://doi.org/10.1016/j.enpol.2008.09.058.

(8) Roussanaly, S.; Berghout, N.; Fout, T.; Garcia, M.; Gardarsdottir, S.; Nazir, S. M.; Ramirez, A.; Rubin, E. S. Towards Improved Cost Evaluation of Carbon Capture and Storage from Industry. *Int. J. Greenh. Gas Control* **2021**, *106* (January), 103263. https://doi.org/10.1016/j.ijggc.2021.103263.

(9) Heddle, G.; Herzog, H.; Klett, M. The Economics of Carbon Dioxide Storage. **2003**, 115.

(10) Rackley, S. Carbon Capture and Storage. *Carbon Capture and Storage* **2009**, *325* (September), 1–392. https://doi.org/10.1016/C2009-0-19306-6.

(11) Aresta, M.; Dibenedetto, A.; Angelini, A. The Changing Paradigm in CO2 Utilization. *J. CO2 Util.* **2013**, *3–4*, 65–73. https://doi.org/10.1016/j.jcou.2013.08.001.

(12) Cuéllar-Franca, R. M.; Azapagic, A. Carbon Capture, Storage and Utilisation Technologies: A Critical Analysis and Comparison of Their Life Cycle Environmental Impacts. *J. CO2 Util.* **2015**, *9*, 82–102. https://doi.org/10.1016/j.jcou.2014.12.001.

(13) Meylan, F. D.; Moreau, V.; Erkman, S. CO2 Utilization in the Perspective of Industrial Ecology, an Overview. *J. CO2 Util.* **2015**, *12*, 101–108. https://doi.org/10.1016/j.jcou.2015.05.003.

(14) Psarras, P. C.; Comello, S.; Bains, P.; Charoensawadpong, P.; Reichelstein, S.; Wilcox, J. Carbon Capture and Utilization in the Industrial Sector. *Environ. Sci. Technol.* **2017**, *51* (19), 11440–11449. https://doi.org/10.1021/acs.est.7b01723.

(15) Gabrielli, P.; Gazzani, M.; Mazzotti, M. The Role of Carbon Capture and Utilization, Carbon Capture and Storage, and Biomass to Enable a Net-Zero-CO2 Emissions Chemical Industry. *Ind. Eng. Chem. Res.* **2020**, *59* (15), 7033–7045. https://doi.org/10.1021/acs.iecr.9b06579.

(16) Thonemann, N.; Pizzol, M. Consequential Life Cycle Assessment of Carbon Capture and Utilization Technologies within the Chemical Industry. *Energy Environ. Sci.* **2019**, *12* (7), 2253–2263. https://doi.org/10.1039/c9ee00914k.

(17) Mac Dowell, N.; Fennell, P. S.; Shah, N.; Maitland, G. C. The Role of CO2 Capture and Utilization in Mitigating Climate Change. *Nat. Clim. Chang.* **2017**, *7* (4), 243–249. https://doi.org/10.1038/nclimate3231.

(18) Hepburn, C.; Adlen, E.; Beddington, J.; Carter, E. A.; Fuss, S.; Mac Dowell, N.; Minx, J. C.; Smith, P.; Williams, C. K. The Technological and Economic Prospects for CO2 Utilization and Removal. *Nature* **2019**, *575* (7781), 87–97. https://doi.org/10.1038/s41586-019-1681-6.

(19) Zhu, Q. Developments on CO2-Utilization Technologies. *Clean Energy* **2019**, *3* (2), 85–100. https://doi.org/10.1093/ce/zkz008.

(20) Bachu, S. CO2 Storage in Geological Media: Role, Means, Status and Barriers to Deployment. *Prog. Energy Combust. Sci.* **2008**, *34* (2), 254–273. https://doi.org/10.1016/j.pecs.2007.10.001.

(21) Bachu, S.; Bonijoly, D.; Bradshaw, J.; Burruss, R.; Holloway, S.; Christensen, N. P.; Mathiassen, O. M. CO2 Storage Capacity Estimation: Methodology and Gaps. *Int. J. Greenh. Gas Control* **2007**, *1* (4), 430–443. https://doi.org/10.1016/S1750-5836(07)00086-2.

(22) Saeidi, S.; Najari, S.; Hessel, V.; Wilson, K.; Keil, F. J.; Concepción, P.; Suib, S. L.; Rodrigues, A. E. Recent Advances in CO2 Hydrogenation to Value-Added Products — Current Challenges and Future Directions. *Prog. Energy Combust. Sci.* **2021**, *85*, 100905. https://doi.org/10.1016/j.pecs.2021.100905.

(23) Álvarez, A.; Bansode, A.; Urakawa, A.; Bavykina, A. V.; Wezendonk, T. A.; Makkee, M.; Gascon, J.; Kapteijn, F. Challenges in the Greener Production of Formates/Formic Acid, Methanol, and DME by Heterogeneously Catalyzed CO2 Hydrogenation Processes. *Chem. Rev.* **2017**, *117* (14), 9804–9838. https://doi.org/10.1021/acs.chemrev.6b00816.

(24) Yang, H.; Zhang, C.; Gao, P.; Wang, H.; Li, X.; Zhong, L.; Wei, W.; Sun, Y. A Review of the Catalytic Hydrogenation of Carbon Dioxide into Value-Added Hydrocarbons. *Catal. Sci. Technol.* **2017**, *7* (20), 4580–4598. https://doi.org/10.1039/c7cy01403a.

(25) Ye, R. P.; Ding, J.; Gong, W.; Argyle, M. D.; Zhong, Q.; Wang, Y.; Russell, C. K.; Xu, Z.; Russell, A. G.; Li, Q.; et al. CO2 Hydrogenation to High-Value Products via Heterogeneous Catalysis. *Nat. Commun.* **2019**, *10* (1). https://doi.org/10.1038/s41467-019-13638-9.

(26) Nezam, I.; Zhou, W.; Gusmão, G. S.; Realff, M. J.; Wang, Y.; Medford, A. J.; Jones, C. W. Direct Aromatization of CO2via Combined CO2hydrogenation and Zeolite-Based Acid Catalysis. *J. CO2 Util.* **2021**, *45* (December 2020). https://doi.org/10.1016/j.jcou.2020.101405.

(27) Wang, W.-H.; Himeda, Y.; Muckerman, J. T.; Manbeck, G. F.; Fujita, E. CO 2 Hydrogenation to Formate and Methanol as an Alternative to Photo- and Electrochemical CO 2 Reduction . *Chem. Rev.* **2015**, *115* (23), 12936–12973. https://doi.org/10.1021/acs.chemrev.5b00197.

(28) Roy, S.; Cherevotan, A.; Peter, S. C. Thermochemical CO2 Hydrogenation to Single Carbon Products: Scientific and Technological Challenges. *ACS Energy Lett.* **2018**, *3* (8), 1938–1966. https://doi.org/10.1021/acsenergylett.8b00740.

(29) Kattel, S.; Liu, P.; Chen, J. G. Tuning Selectivity of CO2 Hydrogenation Reactions at the Metal/Oxide Interface. *J. Am. Chem. Soc.* **2017**, *139* (29), 9739–9754. https://doi.org/10.1021/jacs.7b05362.

(30) Behling, N.; Williams, M. C.; Managi, S. Fuel Cells and the Hydrogen Revolution: Analysis of a Strategic Plan in Japan. *Econ. Anal. Policy* **2015**, *48*, 204–221. https://doi.org/10.1016/j.eap.2015.10.002.

(31) Matsuda, S.; Kubota, H. The Feasibility of a “Hydrogen Society.” *Glob. J. Res. Eng.* **2016**, *16* (3).

(32) Nagashima, M. *Japan’s Hydrogen Strategy and Its Economic and Geopolitical Implications*; 2018.

(33) Yoshida, T.; Kojima, K. Toyota MIRAI Fuel Cell Vehicle and Progress toward a Future Hydrogen Society. *Electrochem. Soc. Interface* **2015**, *24* (2), 45–49. https://doi.org/10.1149/2.F03152if.

(34) Khan, M. U.; Wang, L.; Liu, Z.; Gao, Z.; Wang, S.; Li, H.; Zhang, W.; Wang, M.; Wang, Z.; Ma, C.; et al. Pt3Co Octapods as Superior Catalysts of CO2Hydrogenation. *Angew. Chemie - Int. Ed.* **2016**, *55* (33), 9548–9552. https://doi.org/10.1002/anie.201602512.

(35) Wesselbaum, S.; Vom Stein, T.; Klankermayer, J.; Leitner, W. Hydrogenation of Carbon Dioxide to Methanol by Using a Homogeneous Ruthenium-Phosphine Catalyst. *Angew. Chemie - Int. Ed.* **2012**, *51* (30), 7499–7502. https://doi.org/10.1002/anie.201202320.

(36) Huff, C. A.; Sanford, M. S. Cascade Catalysis for the Homogeneous Hydrogenation of CO2 to Methanol. *J. Am. Chem. Soc.* **2011**, *133* (45), 18122–18125. https://doi.org/10.1021/ja208760j.

(37) Jessop, P. G.; Ikariya, T.; Noyori, R. Homogeneous Hydrogenation of Carbon Dioxide. *Chem. Rev.* **1995**, *95* (2), 259–272. https://doi.org/10.1021/cr00034a001.

(38) Gothe, M. L.; Pérez-Sanz, F. J.; Braga, A. H.; Borges, L. R.; Abreu, T. F.; Bazito, R. C.; Gonçalves, R. V.; Rossi, L. M.; Vidinha, P. Selective CO2hydrogenation into Methanol in a Supercritical Flow Process. *J. CO2 Util.* **2020**, *40* (May), 101195. https://doi.org/10.1016/j.jcou.2020.101195.

(39) Kar, S.; Sen, R.; Goeppert, A.; Prakash, G. K. S. Integrative CO2Capture and Hydrogenation to Methanol with Reusable Catalyst and Amine: Toward a Carbon Neutral Methanol Economy. *J. Am. Chem. Soc.* **2018**, *140* (5), 1580–1583. https://doi.org/10.1021/jacs.7b12183.

(40) Rodriguez, J. A.; Liu, P.; Stacchiola, D. J.; Senanayake, S. D.; White, M. G.; Chen, J. G. Hydrogenation of CO2to Methanol: Importance of Metal-Oxide and Metal-Carbide Interfaces in the Activation of CO2. *ACS Catal.* **2015**, *5* (11), 6696–6706. https://doi.org/10.1021/acscatal.5b01755.

(41) Ting, K. W.; Toyao, T.; Siddiki, S. M. A. H.; Shimizu, K. I. Low-Temperature Hydrogenation of CO 2 to Methanol over Heterogeneous TiO 2 -Supported Re Catalysts. *ACS Catal.* **2019**, *9* (4), 3685–3693. https://doi.org/10.1021/acscatal.8b04821.

(42) Olah, G. A. Beyond Oil and Gas: The Methanol Economy. *Angew. Chemie - Int. Ed.* **2005**, *44* (18), 2636–2639. https://doi.org/10.1002/anie.200462121.

(43) Sto, M. Methanol-to-Hydrocarbons : Catalytic Materials and Their Behavior1. *Microporous Mesoporous Mater.* **1999**, *29*, 3–48.

(44) Keil, F. J. Methanol-to-Hydrocarbons: Process Technology. *Microporous Mesoporous Mater.* **1999**, *29* (1–2), 49–66. https://doi.org/10.1016/S1387-1811(98)00320-5.

(45) Tian, P.; Wei, Y.; Ye, M.; Liu, Z. Methanol to Olefins (MTO): From Fundamentals to Commercialization. *ACS Catal.* **2015**, *5* (3), 1922–1938. https://doi.org/10.1021/acscatal.5b00007.

(46) Olsbye, U.; Svelle, S.; Bjrgen, M.; Beato, P.; Janssens, T. V. W.; Joensen, F.; Bordiga, S.; Lillerud, K. P. Conversion of Methanol to Hydrocarbons: How Zeolite Cavity and Pore Size Controls Product Selectivity. *Angew. Chemie - Int. Ed.* **2012**, *51* (24), 5810–5831. https://doi.org/10.1002/anie.201103657.

(47) Yang, M.; Fan, D.; Wei, Y.; Tian, P.; Liu, Z. Recent Progress in Methanol-to-Olefins (MTO) Catalysts. *Adv. Mater.* **2019**, *31* (50), 1–15. https://doi.org/10.1002/adma.201902181.

(48) Xu, M.; Lunsford, J. H.; Goodman, D. W.; Bhattacharyya, A. Synthesis of Dimethyl Ether (DME) from Methanol over Solid-Acid Catalysts. *Appl. Catal. A Gen.* **1997**, *149* (2), 289–301. https://doi.org/10.1016/S0926-860X(96)00275-X.

(49) Pontzen, F.; Liebner, W.; Gronemann, V.; Rothaemel, M.; Ahlers, B. CO2-Based Methanol and DME - Efficient Technologies for Industrial Scale Production. *Catal. Today* **2011**, *171* (1), 242–250. https://doi.org/10.1016/j.cattod.2011.04.049.

(50) Fu, Y.; Hong, T.; Chen, J.; Auroux, A.; Shen, J. Surface Acidity and the Dehydration of Methanol to Dimethyl Ether. *Thermochim. Acta* **2005**, *434* (1–2), 22–26. https://doi.org/10.1016/j.tca.2004.12.023.

(51) Yaripour, F.; Baghaei, F.; Schmidt, I.; Perregaard, J. Catalytic Dehydration of Methanol to Dimethyl Ether (DME) over Solid-Acid Catalysts. *Catal. Commun.* **2005**, *6* (2), 147–152. https://doi.org/10.1016/j.catcom.2004.11.012.

(52) Bai, S.; Shao, Q.; Wang, P.; Dai, Q.; Wang, X.; Huang, X. Highly Active and Selective Hydrogenation of CO2 to Ethanol by Ordered Pd-Cu Nanoparticles. *J. Am. Chem. Soc.* **2017**, *139* (20), 6827–6830. https://doi.org/10.1021/jacs.7b03101.

(53) Kusama, H.; Okabe, K.; Sayama, K.; Arakawa, H. Ethanol Synthesis by Catalytic Hydrogenation of CO2 over Rh-Fe/SiO2 Catalysts. *Energy* **1997**, *22* (2–3), 343–348. https://doi.org/10.1016/S0360-5442(96)00095-3.

(54) Wang, L.; Wang, L.; Zhang, J.; Liu, X.; Wang, H.; Zhang, W.; Yang, Q.; Ma, J.; Dong, X.; Yoo, S. J.; et al. Selective Hydrogenation of CO2 to Ethanol over Cobalt Catalysts. *Angew. Chemie - Int. Ed.* **2018**, *57* (21), 6104–6108. https://doi.org/10.1002/anie.201800729.

(55) He, Z.; Qian, Q.; Ma, J.; Meng, Q.; Zhou, H.; Song, J.; Liu, Z.; Han, B. Water-Enhanced Synthesis of Higher Alcohols from CO2 Hydrogenation over a Pt/Co3O4 Catalyst under Milder Conditions. *Angew. Chemie - Int. Ed.* **2016**, *55* (2), 737–741. https://doi.org/10.1002/anie.201507585.

(56) Xu, D.; Yang, H.; Hong, X.; Liu, G.; Edman Tsang, S. C. Tandem Catalysis of Direct CO2Hydrogenation to Higher Alcohols. *ACS Catal.* **2021**, *11* (15), 8978–8984. https://doi.org/10.1021/acscatal.1c01610.

(57) Schemme, S.; Breuer, J. L.; Samsun, R. C.; Peters, R.; Stolten, D. Promising Catalytic Synthesis Pathways towards Higher Alcohols as Suitable Transport Fuels Based on H2 and CO2. *J. CO2 Util.* **2018**, *27* (July), 223–237. https://doi.org/10.1016/j.jcou.2018.07.013.

(58) Zeng, F.; Mebrahtu, C.; Xi, X.; Liao, L.; Ren, J.; Xie, J.; Heeres, H. J.; Palkovits, R. Catalysts Design for Higher Alcohols Synthesis by CO2 Hydrogenation: Trends and Future Perspectives. *Appl. Catal. B Environ.* **2021**, *291* (March), 120073. https://doi.org/10.1016/j.apcatb.2021.120073.

(59) Liu, J.; Zhang, A.; Jiang, X.; Liu, M.; Sun, Y.; Song, C.; Guo, X. Selective CO2 Hydrogenation to Hydrocarbons on Cu-Promoted Fe-Based Catalysts: Dependence on Cu-Fe Interaction. *ACS Sustain. Chem. Eng.* **2018**, *6* (8), 10182–10190. https://doi.org/10.1021/acssuschemeng.8b01491.

(60) Zhou, W.; Cheng, K.; Kang, J.; Zhou, C.; Subramanian, V.; Zhang, Q.; Wang, Y. New Horizon in C1 Chemistry: Breaking the Selectivity Limitation in Transformation of Syngas and Hydrogenation of CO2 into Hydrocarbon Chemicals and Fuels. *Chem. Soc. Rev.* **2019**, *48* (12), 3193–3228. https://doi.org/10.1039/c8cs00502h.

(61) Guo, L.; Sun, J.; Ge, Q.; Tsubaki, N. Recent Advances in Direct Catalytic Hydrogenation of Carbon Dioxide to Valuable C2+ Hydrocarbons. *J. Mater. Chem. A* **2018**, *6* (46), 23244–23262. https://doi.org/10.1039/c8ta05377d.

(62) Ding, F.; Zhang, A.; Liu, M.; Zuo, Y.; Li, K.; Guo, X.; Song, C. CO2 Hydrogenation to Hydrocarbons over Iron-Based Catalyst: Effects of Physicochemical Properties of Al2O3 Supports. *Ind. Eng. Chem. Res.* **2014**, *53* (45), 17563–17569. https://doi.org/10.1021/ie5031166.

(63) Guo, L.; Sun, S.; Li, J.; Gao, W.; Zhao, H.; Zhang, B.; He, Y.; Zhang, P.; Yang, G.; Tsubaki, N. Boosting Liquid Hydrocarbons Selectivity from CO2 Hydrogenation by Facilely Tailoring Surface Acid Properties of Zeolite via a Modified Fischer-Tropsch Synthesis. *Fuel* **2021**, *306* (August), 121684. https://doi.org/10.1016/j.fuel.2021.121684.

(64) Zhang, Z.; Huang, G.; Tang, X.; Yin, H.; Kang, J.; Zhang, Q.; Wang, Y. Zn and Na Promoted Fe Catalysts for Sustainable Production of High-Valued Olefins by CO2 Hydrogenation. *Fuel* **2022**, *309* (July 2021), 122105. https://doi.org/10.1016/j.fuel.2021.122105.

(65) Guerra, L.; Rossi, S.; Rodrigues, J.; Gomes, J.; Puna, J.; Santos, M. T. Methane Production by a Combined Sabatier Reaction/Water Electrolysis Process. *J. Environ. Chem. Eng.* **2018**, *6* (1), 671–676. https://doi.org/10.1016/j.jece.2017.12.066.

(66) Su, X.; Xu, J.; Liang, B.; Duan, H.; Hou, B.; Huang, Y. Catalytic Carbon Dioxide Hydrogenation to Methane: A Review of Recent Studies. *J. Energy Chem.* **2016**, *25* (4), 553–565. https://doi.org/10.1016/j.jechem.2016.03.009.

(67) Miguel, C. V.; Soria, M. A.; Mendes, A.; Madeira, L. M. Direct CO2 Hydrogenation to Methane or Methanol from Post-Combustion Exhaust Streams - A Thermodynamic Study. *J. Nat. Gas Sci. Eng.* **2015**, *22*, 1–8. https://doi.org/10.1016/j.jngse.2014.11.010.

(68) Aziz, M. A. A.; Jalil, A. A.; Triwahyono, S.; Mukti, R. R.; Taufiq-Yap, Y. H.; Sazegar, M. R. Highly Active Ni-Promoted Mesostructured Silica Nanoparticles for CO2 Methanation. *Appl. Catal. B Environ.* **2014**, *147*, 359–368. https://doi.org/10.1016/j.apcatb.2013.09.015.

(69) Ashok, J.; Pati, S.; Hongmanorom, P.; Tianxi, Z.; Junmei, C.; Kawi, S. A Review of Recent Catalyst Advances in CO2 Methanation Processes. *Catal. Today* **2020**, *356* (November 2019), 471–489. https://doi.org/10.1016/j.cattod.2020.07.023.

(70) Beydoun, K.; Thenert, K.; Streng, E. S.; Brosinski, S.; Leitner, W.; Klankermayer, J. Selective Synthesis of Trimethylamine by Catalytic N-Methylation of Ammonia and Ammonium Chloride by Utilizing Carbon Dioxide and Molecular Hydrogen. *ChemCatChem* **2016**, *8* (1), 135–138. https://doi.org/10.1002/cctc.201501116.

(71) Toyao, T.; Siddiki, S. M. A. H.; Morita, Y.; Kamachi, T.; Touchy, A. S.; Onodera, W.; Kon, K.; Furukawa, S.; Ariga, H.; Asakura, K.; et al. Rhenium-Loaded TiO2: A Highly Versatile and Chemoselective Catalyst for the Hydrogenation of Carboxylic Acid Derivatives and the N-Methylation of Amines Using H2 and CO2. *Chem. - A Eur. J.* **2017**, *23* (59), 14848–14859. https://doi.org/10.1002/chem.201702801.

(72) Auer, S. M.; Gredig, S. V.; Köppel, R. A.; Baiker, A. Synthesis of Methylamines from CO2, H2 and NH3 over Cu-Mg-Al Mixed Oxides. *J. Mol. Catal. A Chem.* **1999**, *141* (1–3), 193–203. https://doi.org/10.1016/S1381-1169(98)00263-5.

(73) Gredig, S. V.; Koeppel, R. A.; Baiker, A. Comparative Study of Synthesis of Methylamines from Carbon Oxides and Ammonia over Cu/Al2O3. *Catal. Today* **1996**, *29* (1–4), 339–342. https://doi.org/10.1016/0920-5861(95)00301-0.

(74) Cabrero-Antonino, J. R.; Adam, R.; Beller, M. Catalytic Reductive N-Alkylations Using CO2 and Carboxylic Acid Derivatives: Recent Progress and Developments. *Angew. Chemie - Int. Ed.* **2019**, *58* (37), 12820–12838. https://doi.org/10.1002/anie.201810121.

(75) Gredig, S. V.; Koeppel, R. A.; Baiker, A. Synthesis of Methylamines from Carbon Dioxide and Ammonia. *J. Chem. Soc. Chem. Commun.* **1995**, *46* (1), 73–74. https://doi.org/10.1039/C39950000073.

(76) Lin, W.; Cheng, H.; Wu, Q.; Zhang, C.; Arai, M.; Zhao, F. Selective N-Methylation of N-Methylaniline with CO2 and H2 over TiO2-Supported PdZn Catalyst. *ACS Catal.* **2020**, *10* (5), 3285–3296. https://doi.org/10.1021/acscatal.9b04677.

(77) Lin, S.; Liu, J.; Ma, L. A Review on Recent Developments in N-Methylation Using CO2. *J. CO2 Util.* **2021**, *54* (August), 101759. https://doi.org/10.1016/j.jcou.2021.101759.

(78) Tlili, A.; Frogneux, X.; Blondiaux, E.; Cantat, T. Creating Added Value with a Waste: Methylation of Amines with CO 2 and H2. *Angew. Chemie - Int. Ed.* **2014**, *53* (10), 2543–2545. https://doi.org/10.1002/anie.201310337.

(79) Li, Y.; Yan, T.; Junge, K.; Beller, M. Catalytic Methylation of C-H Bonds Using CO2 and H2. *Angew. Chemie - Int. Ed.* **2014**, *53* (39), 10476–10480. https://doi.org/10.1002/anie.201405779.

(80) Wang, Z.; Chang, H.; Zhang, J.; Sun, Z.; Wu, Y.; Liu, Y.; Zhu, Y.; He, H.; Cao, Y.; Bao, X. Tandem Catalytic Methylation of Naphthalene Using CO2 and H2†. *Chem. Commun.* **2022**, *58* (23), 3779–3782. https://doi.org/10.1039/d2cc00190j.

(81) Shang, X.; Liu, G.; Su, X.; Huang, Y.; Zhang, T. Preferential Synthesis of Toluene and Xylene from CO2Hydrogenation in the Presence of Benzene through an Enhanced Coupling Reaction. *ACS Catal.* **2022**, 13741–13754. https://doi.org/10.1021/acscatal.2c04314.

(82) Zuo, J.; Chen, W.; Liu, J.; Duan, X.; Ye, L.; Yuan, Y. Selective Methylation of Toluene Using CO2and H2to Para-Xylene. *Sci. Adv.* **2020**, *6* (34), 1–9. https://doi.org/10.1126/sciadv.aba5433.

(83) Toyao, T.; Siddiki, S. M. A. H.; Touchy, A. S.; Onodera, W.; Kon, K.; Morita, Y.; Kamachi, T.; Yoshizawa, K.; Shimizu, K. I. TiO2-Supported Re as a General and Chemoselective Heterogeneous Catalyst for Hydrogenation of Carboxylic Acids to Alcohols. *Chem. - A Eur. J.* **2017**, *23* (5), 1001–1006. https://doi.org/10.1002/chem.201604762.

(84) Yoshino, K.; Kajiwara, Y.; Takaishi, N.; Inamoto, Y.; Tsuji, J. Hydrogenation of Carboxylic Acids by Rhenium-Osmium Bimetallic Catalyst. *J. Am. Oil Chem. Soc.* **1990**, *67* (1), 21–24. https://doi.org/10.1007/BF02631383.

(85) Tomishige, K.; Nakagawa, Y.; Tamura, M. Taming Heterogeneous Rhenium Catalysis for the Production of Biomass-Derived Chemicals. *Chinese Chem. Lett.* **2020**, *31* (5), 1071–1077. https://doi.org/10.1016/j.cclet.2019.07.014.

(86) Nakagawa, Y.; Shinmi, Y.; Koso, S.; Tomishige, K. Direct Hydrogenolysis of Glycerol into 1,3-Propanediol over Rhenium-Modified Iridium Catalyst. *J. Catal.* **2010**, *272* (2), 191–194. https://doi.org/10.1016/j.jcat.2010.04.009.

(87) Nakagawa, Y.; Tamura, M.; Tomishige, K. Recent Development of Production Technology of Diesel- and Jet-Fuel-Range Hydrocarbons from Inedible Biomass. *Fuel Process. Technol.* **2019**, *193* (May), 404–422. https://doi.org/10.1016/j.fuproc.2019.05.028.

(88) Nakagawa, Y.; Tamura, M.; Tomishige, K. Catalytic Reduction of Biomass-Derived Furanic Compounds with Hydrogen. *ACS Catal.* **2013**, *3* (12), 2655–2668. https://doi.org/10.1021/cs400616p.

(89) Xiao, J.; Puddephatt, R. J. Pt-Re Clusters and Bimetallic Catalysts. *Coord. Chem. Rev.* **1995**, *143* (C), 457–500. https://doi.org/10.1016/0010-8545(94)07008-8.

(90) Prestvik, R.; Moljord, K.; Grande, K.; Holmen, A. The Influence of Pretreatment on the Metal Function of a Commercial Pt-Re/Al2O3 Catalyst. *J. Catal.* **1998**, *174* (2), 119–129. https://doi.org/10.1006/jcat.1998.1956.

Chapter 2

CO_2 capture and hydrogenation to CO

over Pt-based and Cs-based DFMs

2.1 Introduction

Since the Industrial Revolution in the late 18th century, fossil fuels such as coal, oil, and natural gas have been widely consumed in large quantities around the world, mainly as energy sources and raw materials for chemical products. It is no exaggeration to say that human activities and prosperity would not be possible without fossil fuels. This dependence on fossil fuels is directly linked not only to the depletion of finite fossil resources, but also to the massive release of carbon dioxide, the main cause of global warming (Fig. 1). The reduction in greenhouse gases emissions is of utmost significant as a global issue.CO_2 is one of the main components in greenhouse gases. In recent years, the synthesis of general-purpose chemical products and chemical energy carriers by carbon dioxide conversion has been actively studied worldwide as a means of addressing these two global problems. To reduce CO_2 emissions, considerable effort devoted to the development of CO_2 capture and storage (CCS)[1–7] and CO_2 utilization[8-40] over several decades. CCS has great potential to store a large amount of CO_2, however, there is concern that CO_2 may be released into the atmosphere. For CO_2 utilization, catalytic reaction technologies are indispensable, and many catalytic technologies using heat, light, and electricity as activation sources have been reported. Some of these reactions have been industrialized,[8a] most of them require the separation and purification of CO_2, which are high energy process.

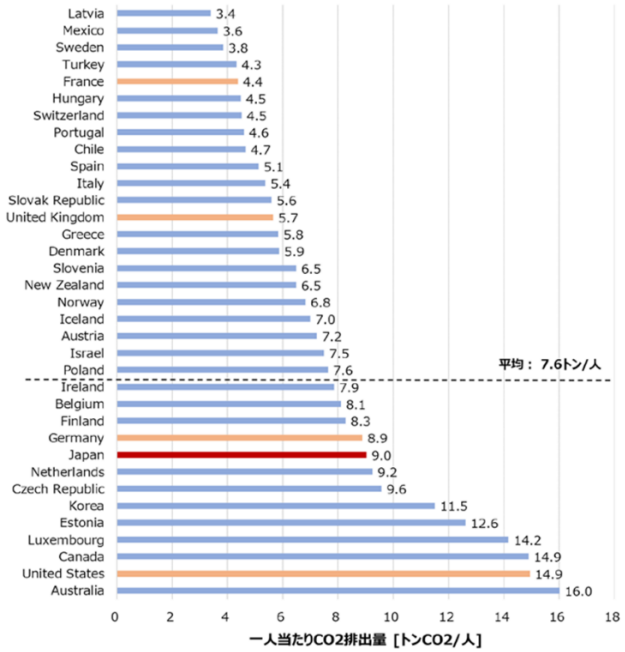

Figure 1 Per capita CO_2 emissions in 2016 for each country

Chemical looping (CL) has recently attracted attention as an alternative to avoid CO_2 separation/purification as it utilizes diluted CO_2 directly.[9–13] CO_2 capture and reduction with

H_2 (CCR) into CH_4/CO is one of the most effective CL processes.[21–23, 25–40]. CCR is theoretically applicable to CO_2 utilization in flow containing O_2, as chemical absorption of CO_2 is uninhibited by O_2; this is advantageous from a practical viewpoint. During this process, the reaction regulation (methanation or reverse water-gas shift reaction: RWGS) is necessary to selectively obtain CH_4 and CO. Several systems using CO_2 absorbents, such as CaO and MgO, with Ru-based CO_2 methanation catalysts have been reported.[21–23] However, the reported systems suffered from significant decrease in CO_2 capture capacity and CH_4 productivity after several cycles.[22,23] In addition, some of them required the temperature swing for efficient CO_2 absorption/desorption.[21,24]

To demonstrate CCR reactions under isothermal conditions, dual-functional materials (DFMs), consisting of basic promoters for CO_2 absorption and metal nanoparticles active for CO_2 hydrogenation, have been studied recently.[25-40] Farrauto et al. first developed Al_2O_3 supported Ru and Ca (Ru-Ca/Al_2O_3) as a DFM to demonstrate CO_2 capture from the mixture with O_2 and reduction with H_2 to form CH_4 under isothermal conditions of 350 °C (Fig. 2).[25,26] They observed that CO_2 adsorbs onto CaO disperses on Al_2O_3 and then spills to Ru during hydrogenation. Gonzalez-Velasco and co-workers revealed that Ru-Na/Al_2O_3 was more effective than Ru-Ca/Al_2O_3 for the CCR to form CH_4 at lower temperatures. This is because that the adsorbed CO_2 on Na_2O/NaOH was decomposed at a lower temperature compared to that on CaO/$Ca(OH)_2$.[27] A few patents have also appeared for CCR using Ru-based DFMs.[31,32]

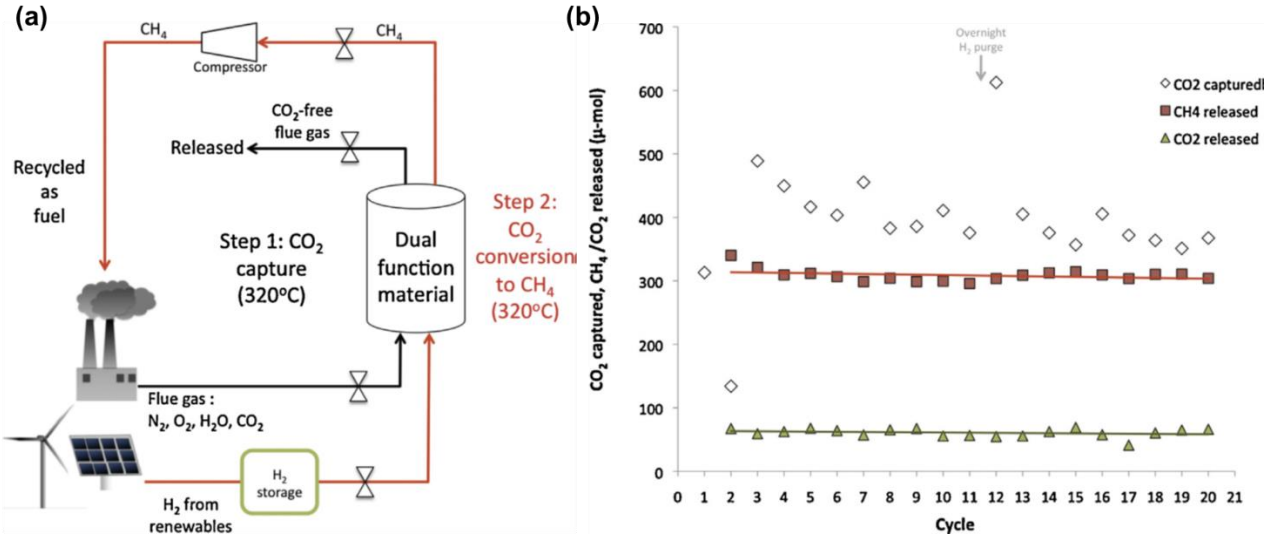

Figure 2 (a) Process diagram for CCR (b) The demonstration CO_2 capture from the mixture with O_2 and reduction with H_2 using Ru-Ca/Al_2O_3 by Farrauto et al.

As non-noble metal-based catalysts, K- or La-promoted Ni/ZrO_2 were investigated by the group of Urakawa. Ni-La/ZrO_2 showed the temperature-independent CO_2 capture capacity and rapid reduction of captured CO_2. Although the initial CO_2 capture capacity of Ni-K/ZrO_2 was larger, it decreased during cyclic unsteady-state reaction conditions[28]. Recently, Kuramoto et al. demonstrated the capture of diluted CO_2 from a mixture with O_2 and selective hydrogenation to CH_4 over Ni-Na/Al_2O_3 under pressurized conditions at 450 °C.[40] In the context of CO formation, Urakawa et al. developed FeCrCu/K/MgO-Al_2O_3 to synthesize CO selectively through CO_2 capture from a mixture with O_2 and successive RWGS at 450−550 °C [29]. A protocol for continuous CCR operation using two reactors has also been proposed. They investigated the effect of K on Cu based on the comparison between Cu/Al_2O_3 and K- or Ba-promoted catalysts, revealing that the K promoter suppressed the oxidation of metallic Cu by CO_2[30]. Ni-based DFMs for CO formation have been also reported by Wu et al.[33] and Kim et al.[34], respectively.

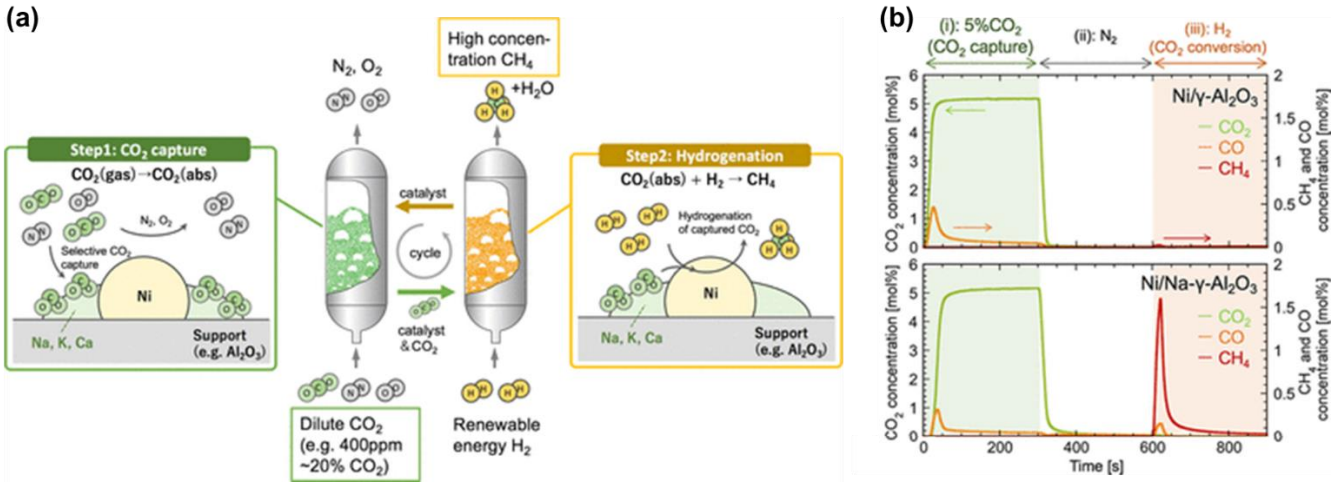

Figure 3 (a)Concept of CCR (b) Performances of Ni/γ-Al_2O_3 and Ni/Na-γ-Al_2O_3 for CO_2 capture and reduction into CH_4 at 450 °C

However, these systems required severe reaction conditions around 600−700 °C due to the endothermic character of RWGS.[41,42] Previous studies have developed effective DFMs and investigated the role of basic promoters. However, there are far few reports on selective CO formation, despite the fact that CO is more useful than CH_4 from the chemical synthesis perspective[43]. Thus, the development of DFMs effective for selective CO formation through CCR at lower temperature is still strongly demanded. In addition, although some previous studies indicated that basic promoters affect the selectivity of CO and CH_4,[30,40] the detailed

effect on surface structures of DFMs and its impact on CO/CH_4 formation remained unrevealed. Moreover, the durability of DFMs in long-term CCR operations has rarely been investigated.[29]

In this study, we developed a Na-promoted Pt nanoparticles (NPs) on Al_2O_3 (Pt-Na/Al_2O_3) as an effective DFM for selective CO production through CCR. The developed catalyst was efficient under isothermal conditions at 350 °C. Comprehensive characterizations were carried out including scanning transmission electron microscopy (STEM), energy-dispersive X-ray (EDX) spectroscopy, X-ray diffraction (XRD), X-ray absorption spectroscopy (XAS), X-ray photoelectron spectroscopy (XPS), and Fourier transform infrared (FTIR) spectroscopy with CO adsorption. These characterizations revealed the formation of Na-modified Pt NPs on Al_2O_3. *In situ* FTIR measurements during CCR showed that the adsorption of generated CO was inhibited over Pt-Na/Al_2O_3, resulting in selective CO formation. The relationship between the surface structure of Pt NPs and CO formation and the applicability in continuous CCR operation were also investigated.

2.2 Experimental Section

2.2.1 Sample Preparation

All catalysts were synthesized by wetness impregnation method. For Pt-Na/Al_2O_3, Al_2O_3 was first obtained by calcination of AlOOH at 900 °C for 3 h. Next, an appropriate amount of $NaNO_3$ aqueous solution was impregnated on Al_2O_3 (Na_2O: 3 wt%). After stirring for 3 h at room temperature, the suspension was evaporated at 50 °C over a vacuum pump and then dried at 100 °C overnight. The obtained solid was calcined at 600 °C for 2 h to afford Na-Al_2O_3. Afterwards, $(NH_3)_2Pt(NO_3)_2$ was impregnated over Na-Al_2O_3 (Pt: 1 wt%) in the same manner, giving the as-calcined Pt-Na/Al_2O_3. Finally, Pt-Na/Al_2O_3 was obtained by H_2 treatment of the as-calcined Pt-Na/Al_2O_3 at 350 °C. Other catalysts were synthesized using the same procedures with Pt-Na/Al_2O_3 catalyst as describe above.

2.2.2 CO_2 Capture from the mixture O_2 and reduction with H_2

The CCR was performed on a vertical quartz fixed-bed flow reactor. A 100 mg of catalyst was put on quartz wool in the middle of the reactor. The reactor set in an electric tube furnace was heated to 350 °C under a N_2 flow (95 mL/min), and then the catalyst was reduced under 5% H_2/N_2 (100 mL/min) for 30 min at 350 °C. Subsequently, a 1% CO_2/10% O_2/N_2 (100 mL/min) flow was fed into the reactor for 4 min to capture CO_2, and then the feeding gas was switched to 5% H_2/N_2 (100 mL/min) for 15 min to reduce the adsorbed CO_2. The composition (CO, CH_4, and CO_2) of effluent gas was quantitatively analyzed using a FTIR spectroscopy (JASCO FT/IR-4600) combined with a gas cell.

2.2.3 Characterization

XRD measurements were carried out on a Rigaku MiniFlex II/AP diffractometer with Cu Kα radiation. High-angle annular dark field STEM (HAADF-STEM) images were recorded on a FEI Titan G2 microscope equipped with an EDX analyzer. Pt L_3-edge XAS measurements were performed in transmittance mode at the BL14B2 beamline in SPring-8 with a Si (311) double-crystal monochromator. The all the spectra were recorded at room temperature. Note that the H_2-treated samples were sealed in the glove box under Ar atmosphere and then used for the measurements without exposure to air. The analysis of XAS spectra was conducted using Athena software ver. 0.9.25, included in the Demeter package.[44] Fourier-transform of the extended X-ray absorption fine structure (EXAFS) oscillation was obtained in the *k* range of 3−12 $Å^{-1}$. The back Fourier-transform obtained in

the *R* range of 1.9−3.4 Å was used for curve-fitting. FEFF8 was used for the calculation of the back-scattering amplitude and phase shift functions. XPS spectra were measured on a JEOL JPC-9010MC spectrometer having a modified UHV chamber employing Mg Kα radiation. The H_2-treated samples were transferred to the chamber without exposure to air. Charge correction was referenced using the O 1s peak at 532.0 eV. FTIR spectra of adsorbed CO were obtained using a JASCO FTIR-4100 spectrometer with a mercury-cadmium-telluride (MCT) detector in a transmission mode (resolution 4 cm^{-1}) under a dynamic condition. A 40 mg catalyst was pressed into a pellet set in a quartz cell equipped with CaF_2 windows and a Dewar vessel. The catalyst was purged with He for a few minutes, and then the fed gas switched to H_2 (20 mL/min) for reduction at 350 °C for 30 min. Next, the gas was switched back to He and the sample was cool down to room temperature followed by vacuum treatment. The background spectrum was taken after the temperature decreased to –100 °C by using the mixture of liquid nitrogen and ethanol. The sample was exposed to 10% CO/He (3 mL/min) and the gas pressure was kept at 100 Pa. Then, the cell was evacuated in vacuum to remove CO in gas phase and physiosorbed on the catalyst. *In situ* FTIR measurements for CCR was carried out using a JASCO FT/IR-4600 spectrometer with a MCT detector and a flow-type quartz IR cell connected to a flow system. The self-supported pellet samples were heated under flowing 10% H_2/N_2 (100 mL/min) at 350 °C for 30 min prior the measurement. The background spectrum was taken after switching the gas to pure N_2, followed by IR spectra recorded under a 1% CO_2/10% O_2/N_2 (100 mL/min) flow at 350 °C for 10 min. Afterwards, the IR cell was purged by pure N_2 (100 mL/min) for 1 min and then switched to 10% H_2/N_2 (100 mL/min) at 350 °C for 30 min.

2.2.4 Long-term Continuous CCR Operation

A long-term continuous CCR operation was performed using two fixed-bed flow reactors (reactor A and B). A 300 mg of Pt-Na/Al_2O_3 was put on quartz wool in the middle for both reactors. Two sides of tube were filled with sea sand. Two timer-control 4-way valves on the top and bottom of the reactors were switched at the same time to continuously change two gases for CO_2 capture and reduction as well as collect two effluent gases. Both reactors set in an electric tube furnace were heated to 350 °C under a N_2 flow (90 mL/min). Subsequently, 10% H_2/N_2 (100 mL/min) was introduced to the reactors for pretreatment for 20 min at 350 °C with one by one. After that, 100 mL/min of 0.5% CO_2/10% O_2/N_2 was fed to reactor A for 30 sec, and then the gas was switched to 100 mL/min of H_2 for the other 30 sec. Oppositely, 100 mL/min of pure H_2 was fed to reactor B for 30 sec, and then the gas was

switched to 100 mL/min of 0.5% CO_2/10% O_2/N_2 for the other 30 sec. The effluent gases containing uncaptured CO_2 (effluent 1) and generated CO, CH_4 and desorbed CO_2 (effluent 2) were continuously collected in each outlet line. The compositions of two effluent gases were continuously collected, as per the monitoring by FTIR spectroscopy (JASCO FT/IR-4600) with gas cells. The background spectrum was measured after H_2 pretreatment followed by N_2 purge. These gas switching were repeated 6000 cycles to evaluate the long-term durability for 100 h.

2.3. Results and Discussion

2.3.1 Results of catalytic activity test in CCR operation

Initially, Pt/Al_2O_3 (Pt: 1 wt%), Na/Al_2O_3 (Na: 3 wt%) and alkali/alkaline earth metal-promoted Pt/Al_2O_3 [Pt-M_1/Al_2O_3 (Pt: 1 wt%, M_1 = Na, K, Mg, or Ca, 3 wt% of Na_2O and MgO, 6 wt% of K_2O and CaO, M_1: 0.75–1.3 mmol/g)], were synthesized in a similar way. They were then evaluated for CO_2 capture from a mixture with O_2 (1% CO_2/10% O_2/N_2) and successive reduction with H_2 (5% H_2/N_2) under isothermal conditions at 350 °C (Table 1). Pt/Al_2O_3 showed a low CO_2 absorption ability (Abs_{CO2}: 0.08 mmol/g) and afforded a small amount of CO and CH_4 (1 and 6 μmol/g, respectively). The maximum CO concentration (C_{CO}max) was low (37 ppm) along with the low CO selectivity (Sel_{CO}: 11%). By contrast, Pt-Na/Al_2O_3 exhibited a higher Abs_{CO2} value (0.19 mmol/g) and yielded a much larger amount of CO (158 μmol/g) with a small amount of CH_4 (12 μmol/g). The Abs_{CO2} value was similar to that of Na/Al_2O_3 (0.21 mmol/g), indicating that Na species serves as CO_2 capture sites. The molar ratio of Abs_{CO2} and Na loading amount (3 wt% of Na_2O) was determined as 39%, which is comparable with the highest value in previously reported DFM form CH_4 formation. The C_{CO}max value had significantly risen to 1559 ppm, and S_{CO} reached 93%. The conversion of absorbed CO_2 ($Conv_{absCO2}$) based on the CO_{2ad} value and the amounts of CO and CH_4 produced was 89%. When Pt-K, Pt-Mg, or Pt-Ca/Al_2O_3 was used instead of Pt-Na/Al_2O_3, the C_{CO}max, Sel_{CO}, and $Conv_{absCO2}$ values decreased to 57–358 ppm, 31%–84%, and 5%–22%, respectively. Note that the Abs_{CO2} for Pt-Ca/Al_2O_3 was the highest (1.07 mmol/g) among Pt-M_1/Al_2O_3. As a control experiment, a physical mixture of Pt/Al_2O_3 and Na/Al_2O_3 was used for CCR. Although the CO_{max} and $Conc_{absCO2}$ increased by combining Na/Al_2O_3 with Pt/Al_2O_3, the amount of generated CO and Sel_{CO} values were much lower than those for Pt-Na/Al_2O_3, indicating that Na species serve as not only CO_2 capture sites but also act as a promotor to enhance the CO formation. Figure 4 shows the effluent concentration profiles of CO_2 and reduction products (CO and CH_4) for Pt/Al_2O_3, Pt-Na/Al_2O_3, and Pt-Mg/Al_2O_3. There was a

longer duration of CO_2 capture for Pt-Na/Al_2O_3 than Pt/Al_2O_3 and Pt-Mg/Al_2O_3, confirming the higher Abs_{CO2} of Pt-Na/Al_2O_3. During the reduction period, the duration of CH_4 formation was longer (>300 s) than that for CO formation (ca. 50–150 s) for Pt/Al_2O_3 and Pt-Mg/Al_2O_3. By contrast, the duration of CO formation was much longer (>500 s) for Pt-Na/Al_2O_3, and CH_4 formation was continuously suppressed for >500 s. These results clearly demonstrate that the basic promoters influence the formation of CO and CH_4 through the hydrogenation of absorbed CO_2 with H_2.

Additionally, other metal NPs supported on Na/Al_2O_3 (M_2-Na/Al_2O_3, M_2 = Pd, Ru, and Cu, 1 wt%) were also prepared and compared with those of Pt-Na/Al_2O_3. The total amounts of generated CO and CH_4 for Pd-, Ru-, and Cu-Na/Al_2O_3 were 19, 34, and 6 μmol/g, respectively; these were much lower than those for Pt-Na/Al_2O_3 (170 μmol/g). Their corresponding C_{CO}max, Sel_{CO}, and $Conv_{absCO2}$ values were also lower than those of Pt-Na/Al_2O_3. Furthermore, Na-modified MgO, SiO_2, and TiO_2 were synthesized and used to prepare other Pt and Na co-loaded materials. Although Abs_{CO2} was improved by using SiO_2 and TiO_2, these additions were not effective for CO synthesis, resulting in an inferior C_{CO}max, Sel_{CO}, and $Conv_{absCO2}$. Based on these results, Pt-Na/Al_2O_3 is the best among the DFMs tested in this study.

To get insights into the plausible Na species (Na_2O or NaOH) and carbonate species (Na_2CO_3 or $NaHCO_3$) under the reaction conditions, *ab initio* thermodynamics analysis was performed. Figure 5 shows the most stable Na species depending on partial pressure of CO_2 (p_{CO2}) and temperature (partial pressure of H_2O (p_{H2O}) is fixed at 3%). Na_2CO_3 is the most stable species below 700 °C at log(p_{CO2}) = -2 (corresponding to 1% CO_2). Under higher temperature conditions, the most stable species becomes Na_2O. Although NaOH becomes more stable than Na_2O in lower temperature regions, Na_2CO_3 is much more stable than NaOH. In all the region, $NaHCO_3$ is the most unstable among the considered Na compounds. These results indicate that both Na_2O and NaOH are possibly formed in the absence of CO_2 (H_2 flow) and that Na_2CO_3 is likely to be formed under CO_2 flow rather than $NaHCO_3$. Furthermore, the phase diagram depending on p_{H2O} and temperature was described to investigate the effect of H_2O (Figure 5b, p_{CO2} is fixed at 1%). NaOH becomes more stable with the increase of p_{H2O}. However, Na_2CO_3 is the most stable species below 700 °C in all the log(p_{H2O}) region investigated. This result suggests that Na species possibly serve as CO_2 absorption sites even in the presence of steam.

Table 1. Results of CO_2 capture from the mixture with O_2 and successive hydrogenation over

DFMs

Catalyst	Abs_{CO2}[a] [mmol/g]	CO[a] [μmol/g]	CH_4[a] [μmol/g]	Sel_{CO}[b] [%]	$C_{CO}max$[a] [ppm]	$Conv_{absCO2}$[c] [%]
Pt/Al_2O_3	0.08	1	6	11	37	9
$Pt\text{-}Na/Al_2O_3$	0.19	158	12	93	1559	89
$Pt\text{-}K/Al_2O_3$	0.12	7	16	31	57	19
$Pt\text{-}Mg/Al_2O_3$	0.12	13	13	51	98	22
$Pt\text{-}Ca/Al_2O_3$	1.07	41	8	84	310	5
Pt/Al_2O_3 + Na/Al_2O_3[d]	0.08	18	25	41	714	57
$Pd\text{-}Na/Al_2O_3$	0.21	14	5	75	61	8
$Ru\text{-}Na/Al_2O_3$	0.61	6	28	17	39	6
$Cu\text{-}Na/Al_2O_3$	0.13	3	3	50	20	8
$Pt\text{-}Na/MgO$	0.13	61	13	82	351	57
$Pt\text{-}Na/SiO_2$	0.32	6	7	48	64	4
$Pt\text{-}Na/TiO_2$	0.39	29	18	61	303	12

Reaction conditions: 100 mg of catalyst, 350 °C, 100 mL/min of 1% CO_2/10% O_2/N_2, followed by 100 mL/min of 5% H_2/N_2 for 15 min. [a] The composition of the effluent gas at the outlet was quantitatively analyzed using FTIR spectroscopy combined with a gas cell; these details are described in SI. [b] Based on the amount of CO and CH_4 generated during the reduction period. [c] The total amounts of generated CO and CH_4 were normalized by the amount of absorbed CO_2. [d] A physical mixture of Pt/Al_2O_3 (100 mg) and Na/Al_2O_3 (100 mg) was used. The amounts of absorbed CO_2 and generated CO/CH_4 were normalized to the total amount of Pt/Al_2O_3 and Na/Al_2O_3 (200 mg).

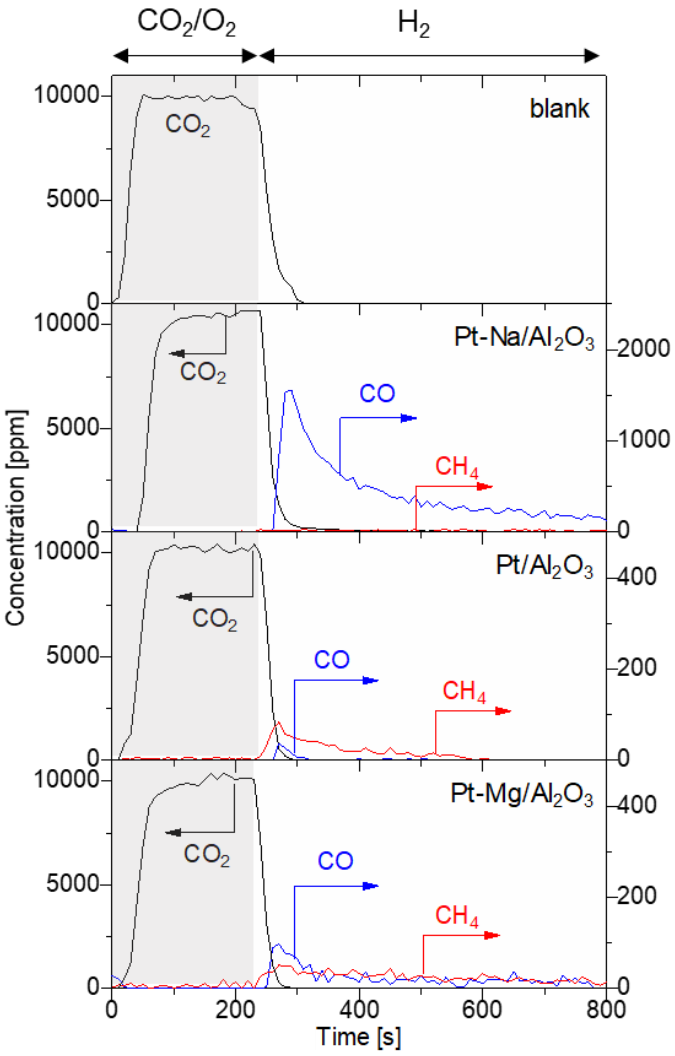

Figure 4. Effluent concentration profiles of CO_2 and reduction products (CO and CH_4) during CO_2 capture (1% CO_2/10% O_2/N_2, 100 mL/min) and reduction (5% H_2, 100 mL/min) over Pt/Al_2O_3, $Pt\text{-}Na/Al_2O_3$, and $Pt\text{-}Mg/Al_2O_3$.

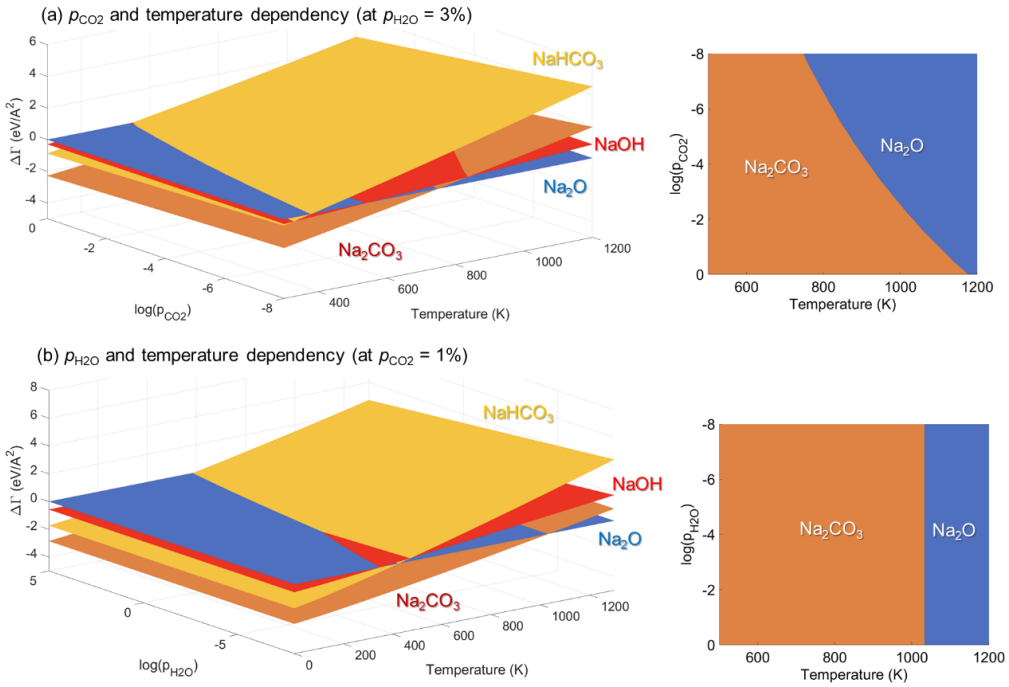

Figure 5. Free energy (ΔΓ) for the formation of possible Na compounds (left) and phase diagram showing the lowest-energy Na compound (right) (a) as a function of CO_2 partial pressure (p_{CO2}) and temperature (H_2O partial pressure (p_{H2O}) is fixed at 3%) and (b) as a function of p_{H2O} and temperature (p_{CO2} is fixed at 1%).

2.3.2 Structure and distribution of Pt NPs and basic promoters

To investigate the structure and distribution of Pt NPs and basic promoters, three DFMs (Pt/Al_2O_3, $Pt\text{-}Na/Al_2O_3$, and $Pt\text{-}Mg/Al_2O_3$) were characterized by STEM and EDX. The STEM images show the formation of small Pt NPs with mean diameters of 2.0, 2.1, and 1.9 nm for Pt/Al_2O_3, $Pt\text{-}Na/Al_2O_3$, and $Pt\text{-}Mg/Al_2O_3$, respectively (Figure 6, for size distribution, see Figure 7). Elemental mapping of $Pt\text{-}Na/Al_2O_3$ revealed that the Pt NPs were surrounded by Na species (Figure 8a, for additional STEM and EDX mapping images, see Figure 9). The quantitative analysis of elemental mapping showed that the Na/Al molar ratios in the areas where Pt NPs existed were higher than those in the areas where Pt NP was absent (Figure 10). These observations indicate that the Pt NPs were modified with the Na species. By contrast, the modified Pt NPs were scarcely observed in the EDX analysis of $Pt\text{-}Mg/Al_2O_3$ (Figure 8b). To support the formation of Na-modified Pt NPs, FTIR measurements with CO adsorption were conducted (Figure 11). For Pt/Al_2O_3, two small peaks at 2102 and 2082 cm^{-1}, assignable to the linearly adsorbed on-top CO on terracelike sites of Pt NPs[45] (corresponding to well-coordinated (WC) Pt sites[46]) were observed with a main band derived from the on-top CO on steplike sites of Pt NPs[45] (under-coordinated Pt sites[46]) at approximately 2065 cm^{-1}. For $Pt\text{-}Na/Al_2O_3$, the peak derived on terracelike sites was hardly observed. Besides, a broad band appeared at approximately 2000 cm^{-1}, which is assigned to the on-top CO adsorbed near edges and vertices[47] (highly under-coordinated Pt sites[46]). For $Pt\text{-}Mg/Al_2O_3$, the band derived from bridge CO on two Pt atoms was observed at about 1800 cm^{-1}.[46] Based on the EDX analysis results and the CO adsorption experiment, the Na species existed on both Al_2O_3 and Pt NPs, whilst the Mg species were mainly dispersed on the Al_2O_3 surface. The formation of Na-modified Pt NPs has been reported in a few previous papers using different supports.[48–50] To gain insight into the formation of Na-modified Pt NPs, XRD measurements were conducted for Na/Al_2O_3 and $Pt\text{-}Na/Al_2O_3$. The XRD pattern of Na/Al_2O_3 was similar to that of the parent Al_2O_3 and any diffraction peaks derived from $NaAlO_2$ were not observed (Figure 12), confirming the high dispersion of the Na species. The predominance diagram of O-Al-Na system (Figure 13) shows that Al_2O_3 is the stable phase at 600 °C, supporting no observation of $NaAlO_2$ phase. The predominance diagram of O-Al-Na system (Figure 13) shows that Al_2O_3 is the stable phase at 600 °C, supporting no observation of $NaAlO_2$ phase. Following the impregnation of Pt species and calcination ($Pt\text{-}Na/Al_2O_3$ before H_2 reduction), new small peaks were observed at 2θ of 22.1°, 35.3°, and 56.2°; these were assigned to the (110), (210), and (222) diffraction peaks of $NaPt_3O_4$,[51] respectively (Figure 14). This suggests that small ternary oxides of Na and Pt were formed

on Na/Al_2O_3.[52] We tried to prepare larger $NaPt_3O_4$ by increasing the loading amount with similar Pt to Na molar ratio (Pt: 3 wt%, Na_2O: 9 wt%), but the diffraction patterns derived from $NaPt_3O_4$ were unfortunately not observed (Figure 14). Upon H_2 treatment, these peaks derived from $NaPt_3O_4$ had disappeared, while peaks derived from metallic Pt were hardly observed, which is consistent with the formation of small Na-modified Pt NPs.

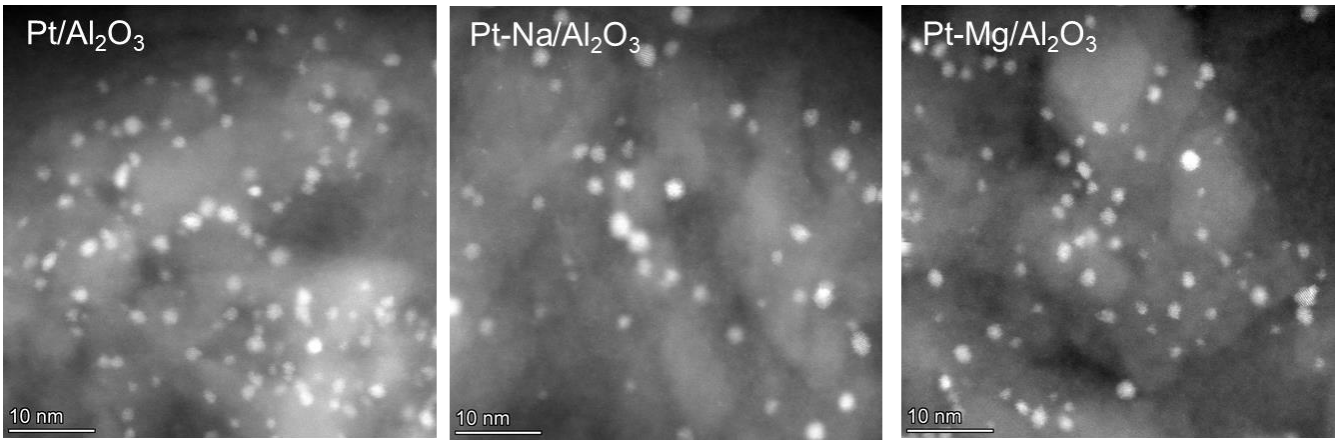

Figure 6. STEM images of Pt/Al_2O_3, $Pt\text{-}Na/Al_2O_3$, and $Pt\text{-}Mg/Al_2O_3$. The H_2-treated samples were exposed to air and then used for STEM observations.

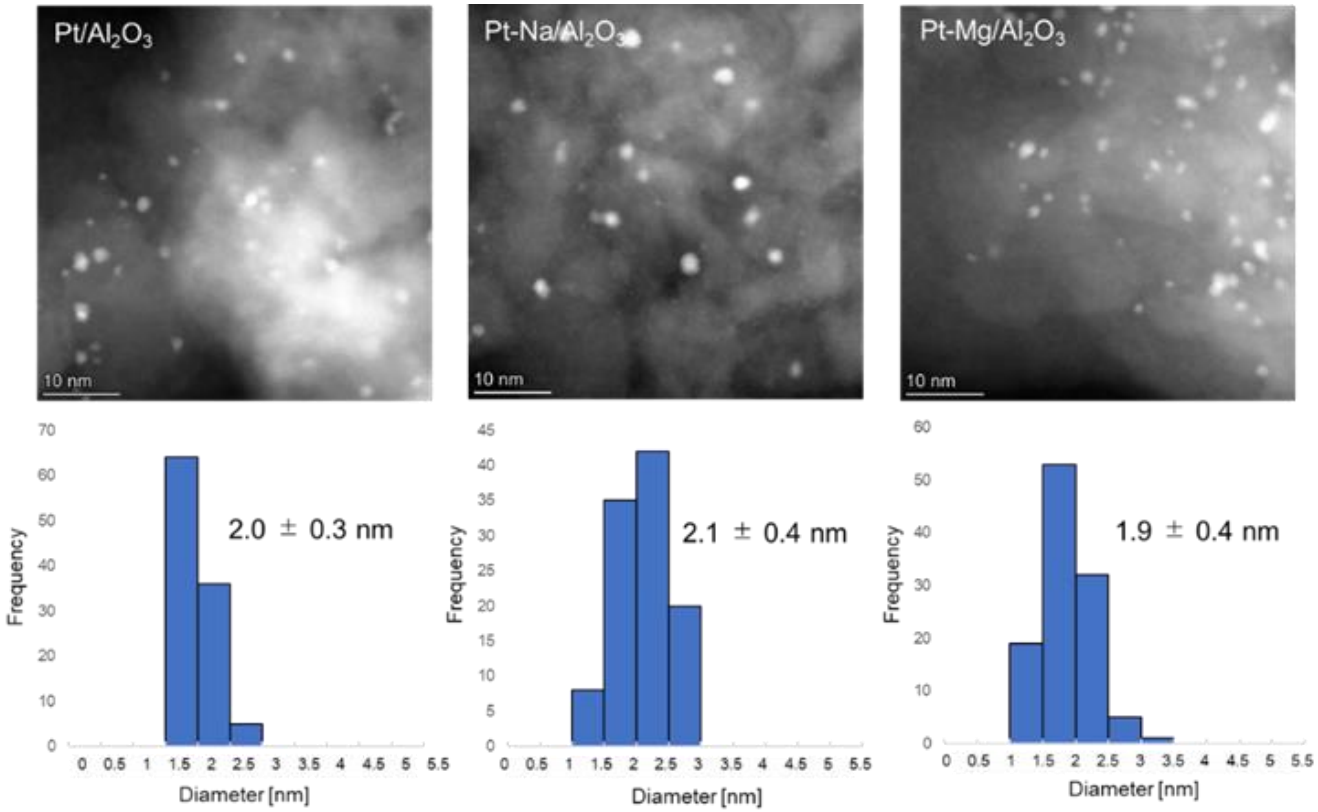

Figure 7. Different STEM images and size distribution of Pt/Al_2O_3, $Pt\text{-}Na/Al_2O_3$, and $Pt\text{-}Mg/Al_2O_3$.

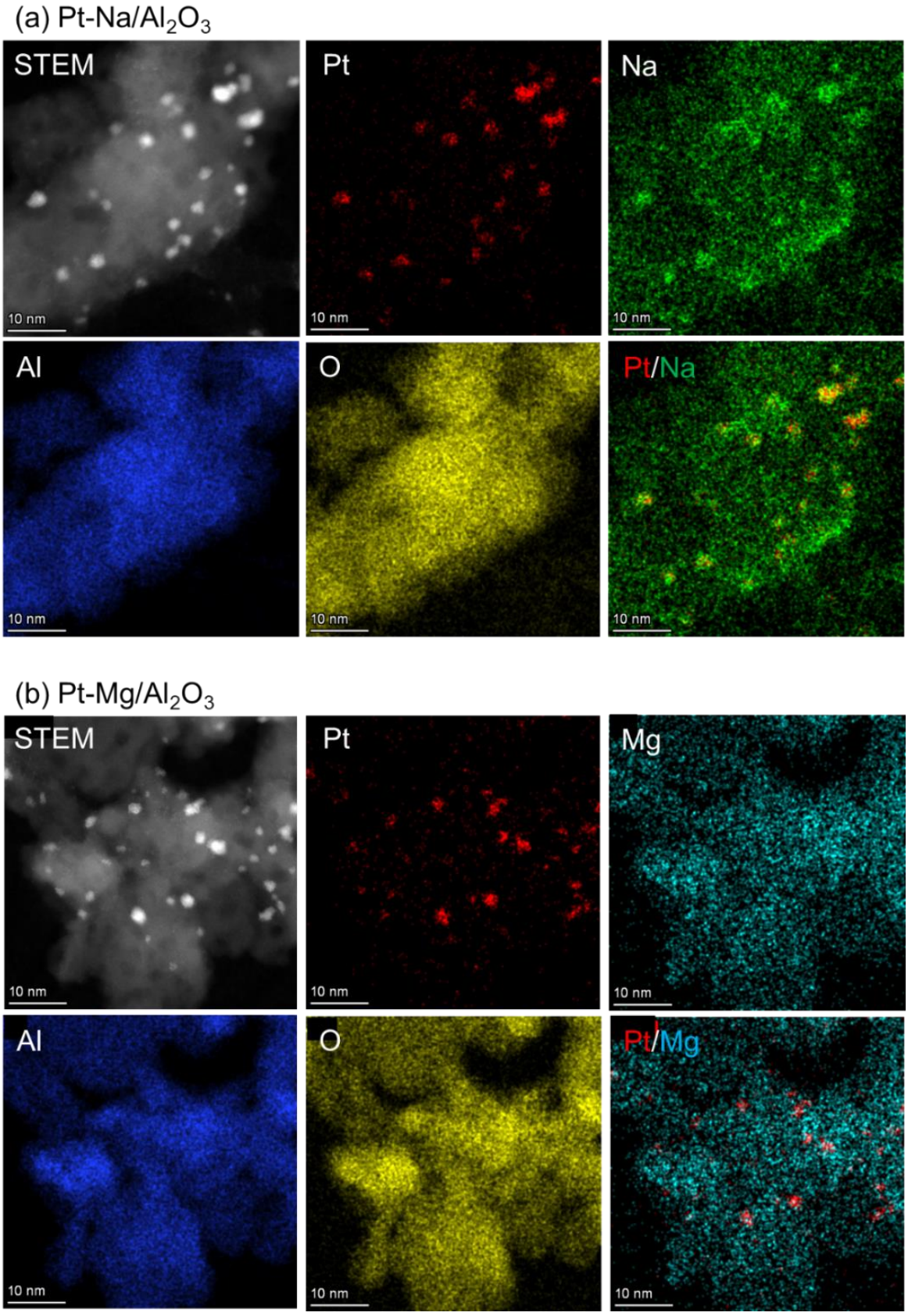

Figure 8. STEM image and elemental mapping obtained by EDX spectroscopy for (a) Pt-Na/Al_2O_3 and (b) Pt-Mg/Al_2O_3. The H_2-treated samples were exposed to air and then used for STEM observations and EDX mapping.

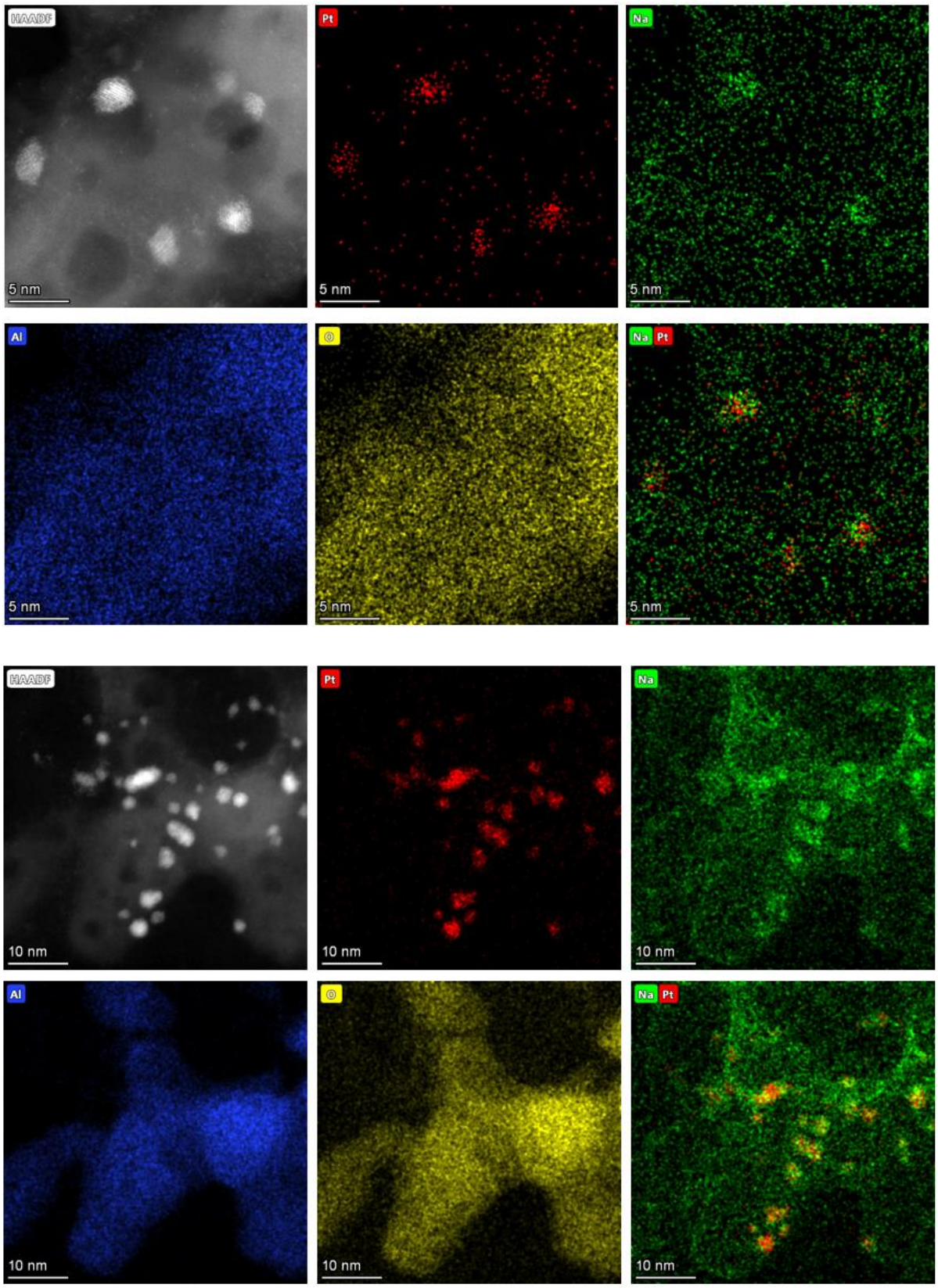

Figure 9. STEM image and elemental mapping obtained by EDX spectroscopy for different regions of Pt-Na/Al_2O_3.

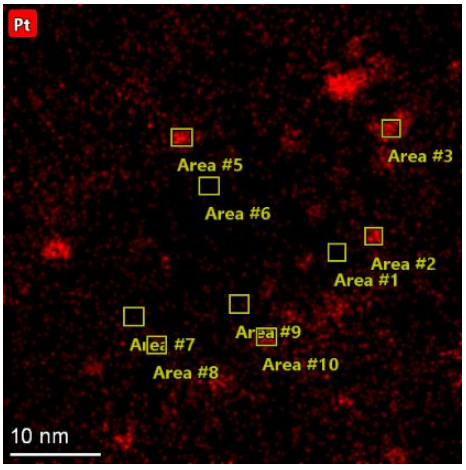

Area	Elements & Atomic (%)			Na/Al mole ratio (%)	Na/Pt mole ratio (%)
	Na	Al	Pt		
1	4.55	95.29	0.16	0.05	n. a.
2	18.32	72.25	9.43	0.25	1.94
3	8.81	78.54	12.66	0.11	0.70
5	29.50	61.46	9.04	0.48	3.26
6	4.91	94.97	0.12	0.05	n. a.*
7	1.49	98.41	0.10	0.02	n. a.
8	11.05	83.75	5.20	0.13	2.12
9	7.08	92.83	0.08	0.08	n. a.
10	16.36	73.92	9.72	0.22	1.68

* n. a. represent not available

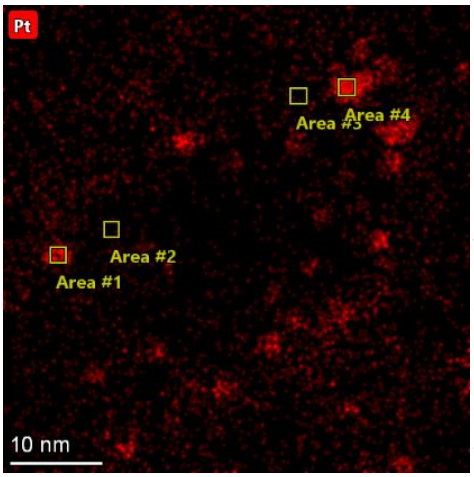

Area	Elements & Atomic (%)			Na/Al mole ratio (%)	Na/Pt mole ratio (%)
	Na	Al	Pt		
1	15.48	65.87	18.66	0.23	0.83
2	11.99	87.93	0.08	0.14	n. a.*
3	6.06	93.91	0.02	0.06	n. a.
4	10.90	67.69	21.41	0.16	0.51

*n. a. represent not available

Figure 10. EDS mapping for Pt and elements component of different areas of Pt-Na/Al_2O_3

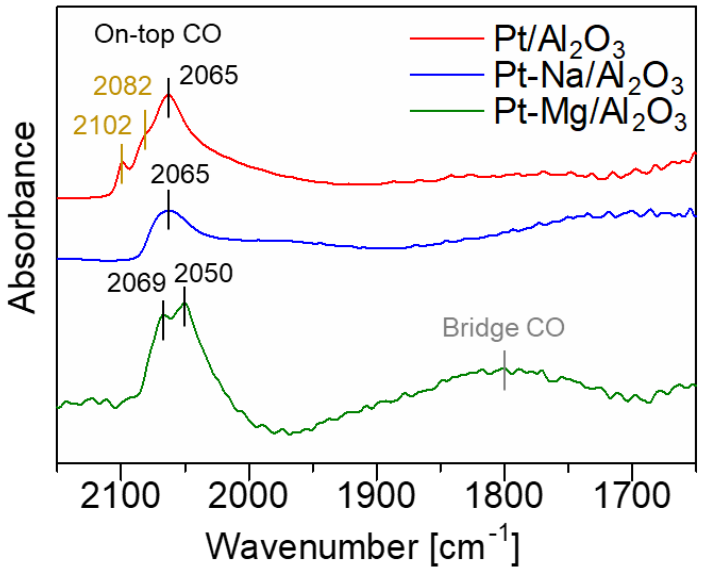

Figure 11. FTIR spectra of CO adsorption for Pt/Al_2O_3, Pt-Na/Al_2O_3, and Pt-Mg/Al_2O_3. Prior to CO adsorption, the catalyst was treated with H_2 and CO was introduced at –100 °C without exposure to air. Brown: on-top CO on well-coordinated (WC) Pt sites, Black: on-top CO on under-coordinated Pt sites, Gray: bridge CO on metallic Pt surface.

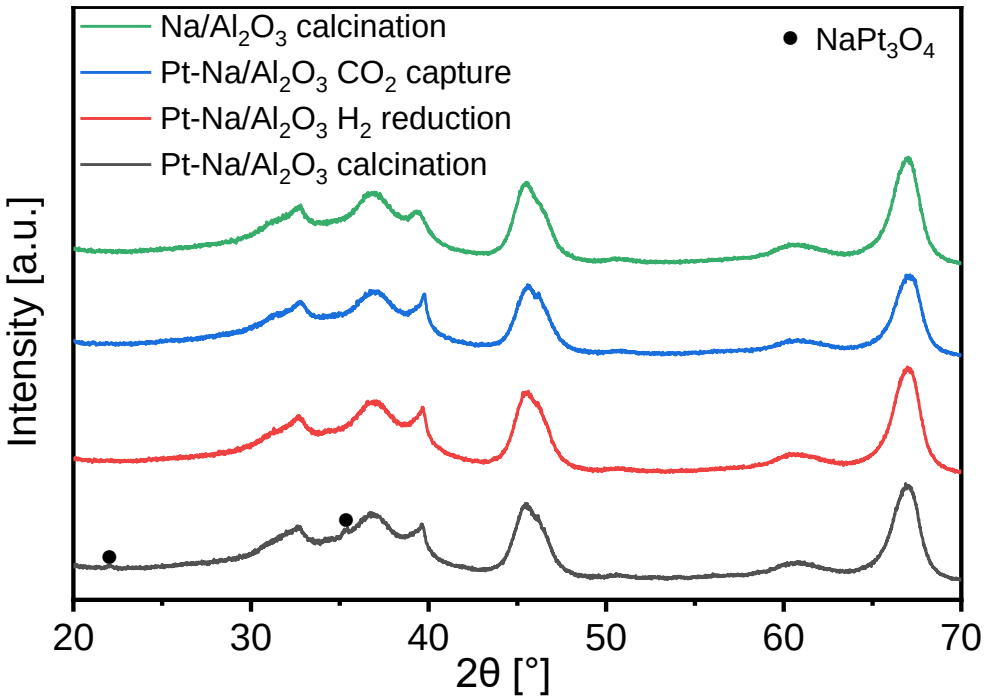

Figure 12. XRD patterns for Na/Al_2O_3 and $Pt\text{-}Na/Al_2O_3$ before H_2 treatment, after H_2 treatment, and after CO_2 capture.

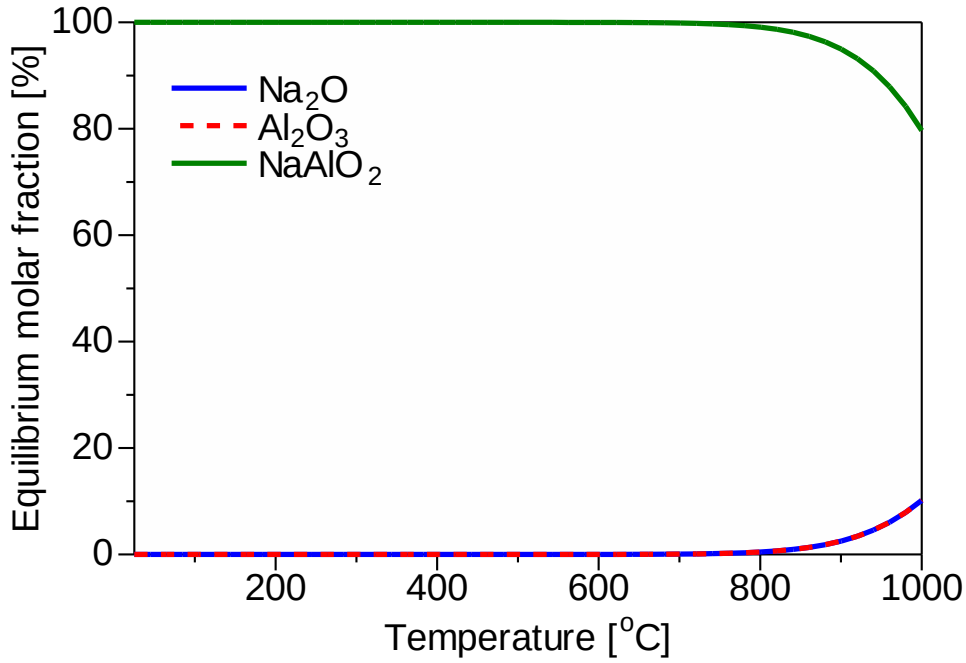

Figure 13. Equilibrium of formation of $NaAlO_2$ from Na_2O(s) and Al_2O_3(G) described using HSC Chemistry 9. Initial molar ratio is Na_2O : Al_2O_3 : $NaAlO_2$ = 1 : 1 : 0..

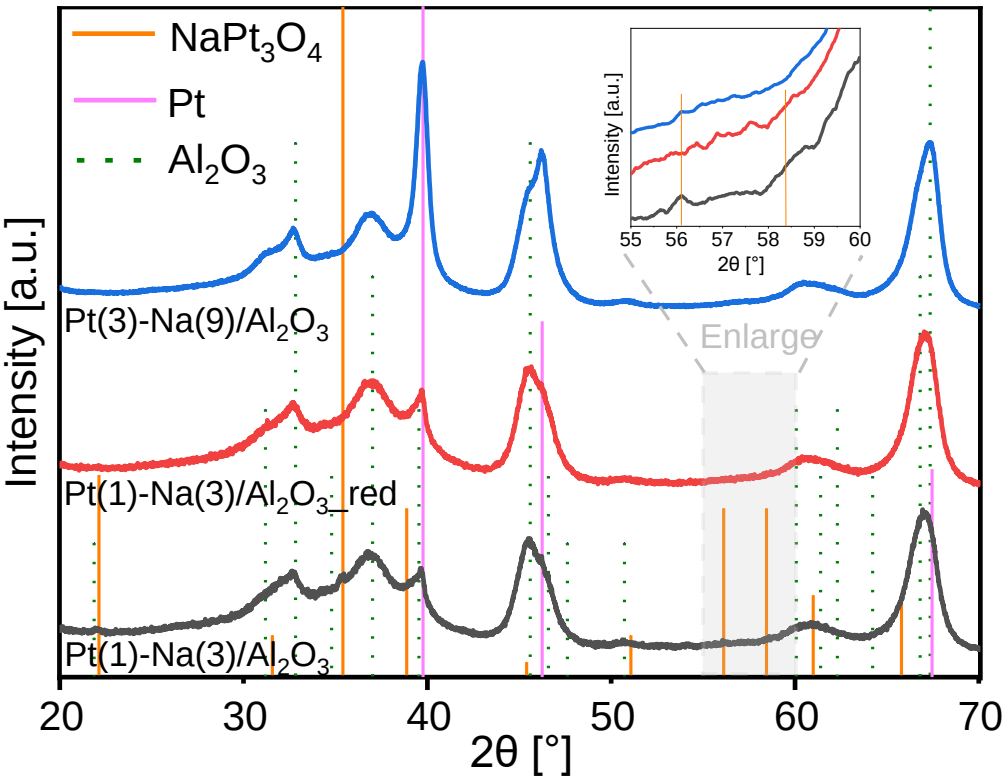

Figure 14. XRD patterns of Pt(1)-Na(3)/Al_2O_3 after calcination and reduction as well as Pt(3)-Na(9)/Al_2O_3 after calcination.

2.3.3 Electronic state of Pt NPs in Pt/Al_2O_3, $Pt\text{-}Na/Al_2O_3$, and $Pt\text{-}Mg/Al_2O_3$

It has been reported that Na promoters affect the electronic state of supported Pt NPs as indicated by spectroscopic techniques.[49,53,54] XAS and XPS measurements were performed to investigate the electronic state of Pt NPs in Pt/Al_2O_3, $Pt\text{-}Na/Al_2O_3$, and $Pt\text{-}Mg/Al_2O_3$. After H_2 treatment, samples were characterized without exposure to air in both measurements. In Pt L_3-edge XAS measurements, X-ray absorption near edge structure (XANES) spectra for the three DFMs were similar to those for Pt foil as opposed to PtO_2. The whiteline intensities for $Pt\text{-}Na$ and $Pt\text{-}Mg/Al_2O_3$ were slightly higher than those for Pt/Al_2O_3, indicating that Pt NPs in $Pt\text{-}Na$ and $Pt\text{-}Mg/Al_2O_3$ were slightly electron-deficient compared to Pt/Al_2O_3 (Figure 15). The whiteline energy of Pt/Al_2O_3 was 11564.6 eV, which is closer to that of Pt foil (11563.9 eV) than that of PtO_2 (11565.6 eV). For $Pt\text{-}Na$ and $Pt\text{-}Mg/Al_2O_3$, the energy values are slightly higher than that of Pt/Al_2O_3 (11564.9 and 11565.2 eV vs. 11564.6 eV, respectively). The FT of EXAFS spectra (Figure 15b) showed a Pt−Pt scattering peak at ~2.6 Å with coordination numbers 9.0, 8.0, and 8.1, respectively (for results of curve-fitting analysis, see Table 2). In the XPS measurements, the Pt 4d region exhibited a $4d_{5/2}$ peak at 315.0 eV, which was assigned to metallic Pt for three DFMs. The peak top for $Pt\text{-}Na$ and $Pt\text{-}Mg/Al_2O_3$ was slightly broad toward higher energy values (Figure 16a), supporting the results obtained in the XAS measurements. Note that the signals from Pt $4f_{5/2}$, $4f_{7/2}$, and $4d_{3/2}$ were potentially overlapped by signals from Al 2p, Na 2s, and Na KLL, respectively; thus, these regions are unsuitable to discuss the electronic state of Pt NPs. The XPS spectrum of the Na 1s region of $Pt\text{-}Na/Al_2O_3$ showed one signal at 1073.3 eV derived from monovalent Na (Figure 16b). This signal confirmed the presence of Na species in the oxidized state. In the spectrum of Mg 2p for $Pt\text{-}Mg/Al_2O_3$, main and shoulder signals, attributable to $MgAl_2O_4$ and $Mg(OH)_2$ were observed at 51.2 and 48.5 eV,[55] respectively (Figure 16c), which supports the presence of Mg species on Al_2O_3.

Furthermore, the effect of different supports (Al_2O_3, MgO, SiO_2, and TiO_2) was studied by N_2 adsorption, XRD, and CO_2 TPD. $Pt\text{-}Na/Al_2O_3$ and $Pt\text{-}Na/SiO_2$ (141 and 152 m^2/g) showed much larger specific surface area than those of Pt-Na/MgO and $Pt\text{-}Na/TiO_2$ (28 and 42 m^2/g). The XRD patters (Figure 17) showed that the diffraction peaks derived from metallic Pt and bulk Na_2O or Na_2CO_3 were hardly observed for $Pt\text{-}Na/SiO_2$, MgO, TiO_2. In CO_2 TPD measurement (Figure 18), there is almost no CO_2 desorption over Pt-Na/MgO and $Pt\text{-}Na/SiO_2$ below 600 °C whereas the CO_2 desorption peak for $Pt\text{-}Na/TiO_2$ was smaller than that for $Pt\text{-}Na/Al_2O_3$. From the results of N_2 adsorption, XRD, and CO_2 TPD measurements, the different CO_2 desorption property is the most plausible reason why $Pt\text{-}Na/Al_2O_3$ showed superior

performance to Pt-Na/SiO_2, MgO, TiO_2 rather than different surface areas and dispersion.

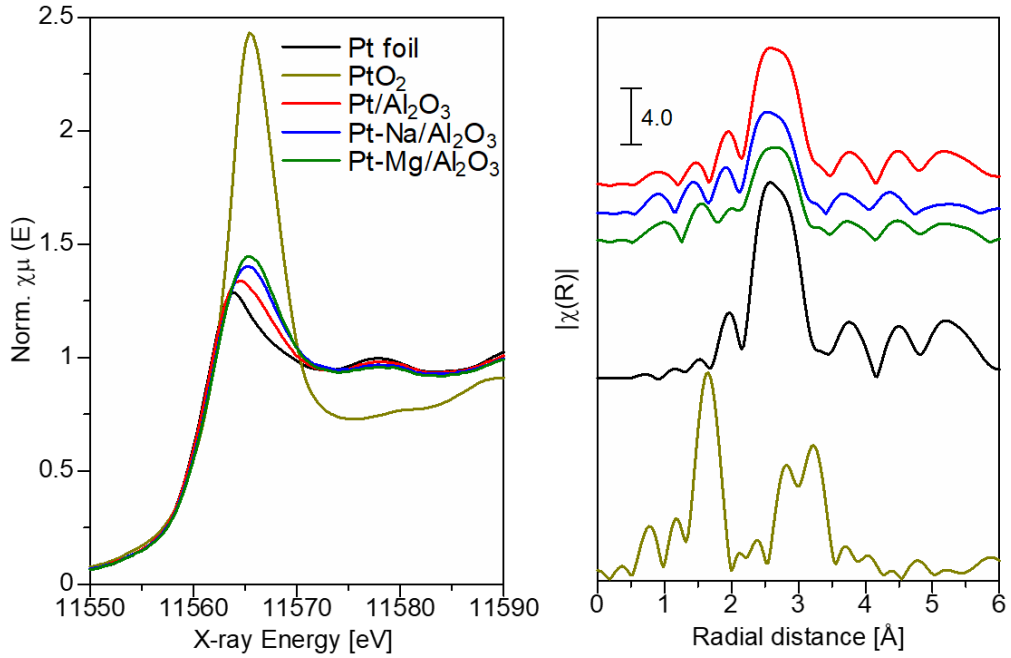

Figure 15. Pt L_3-edge XANES spectra (left) and EXAFS Fourier transforms (right) of Pt/Al_2O_3, Pt-Na/Al_2O_3, and Pt-Mg/Al_2O_3 (without exposure to air after H_2 treatment). All spectra were obtained at room temperature.

Table 2. Curve-fitting analysis of Pt L_3-edge EXAFS of Pt catalysts

Catalyst	Shell	R[a] [Å]	CN[b]	σ[c] [Å]	R-factor[d] [%]
Pt/Al_2O_3	Pt-Pt	2.76	9.0	0.074	3.8
Pt-Na/Al_2O_3	Pt-Pt	2.74	8.0	0.082	2.7
Pt-Mg/Al_2O_3	Pt-Pt	2.76	8.1	0.084	3.1

[a] Bond distance. [b] Coordination numbers. [c] Debye−Waller factor. [d] Residual factor.

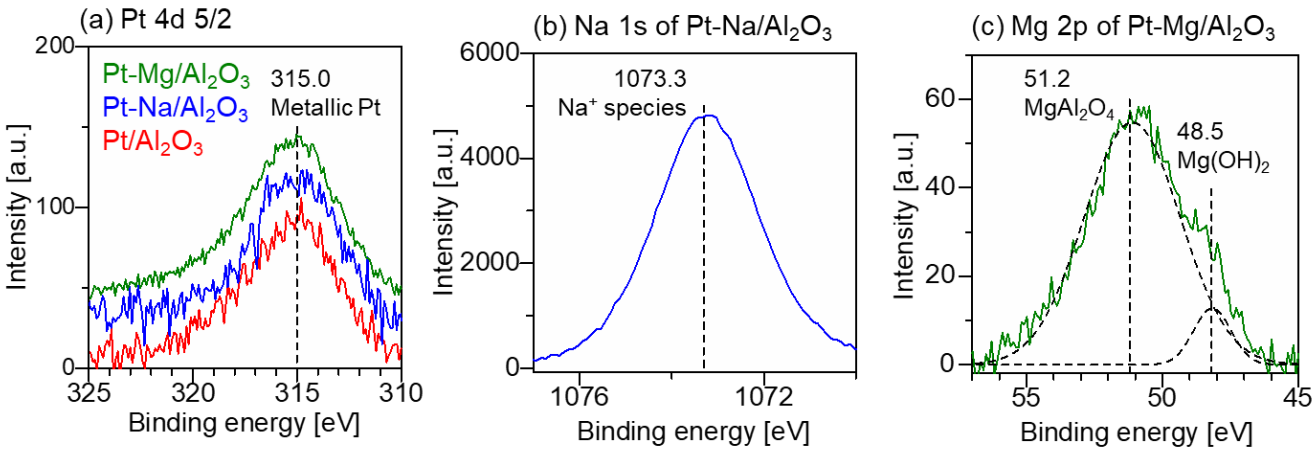

Figure 16. XPS spectra of DFMs. (a) Pt $4d_{5/2}$ region of Pt/Al_2O_3, $Pt\text{-}Na/Al_2O_3$, and $Pt\text{-}Mg/Al_2O_3$, (b) Na 1s region of $Pt\text{-}Na/Al_2O_3$ and (c) Mg 2p region of $Pt\text{-}Mg/Al_2O_3$. All the spectra were obtained after H_2 treatment without exposure to air.

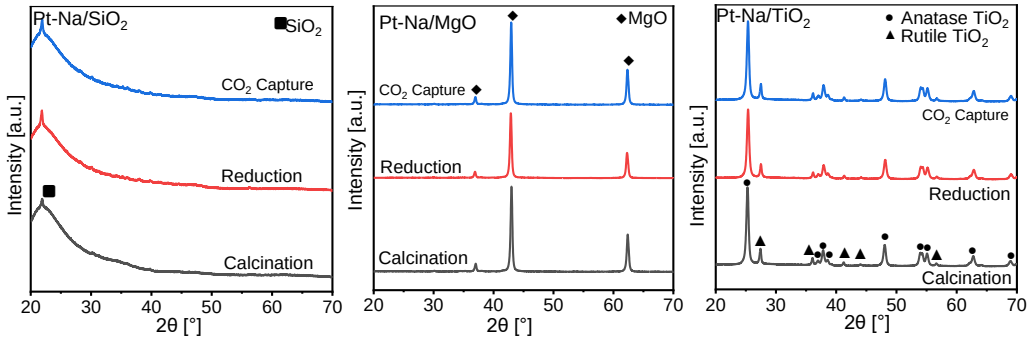

Figure 17. XRD patterns of Pt-Na supported on different oxides after calcination, reduction, and CO_2 capture.

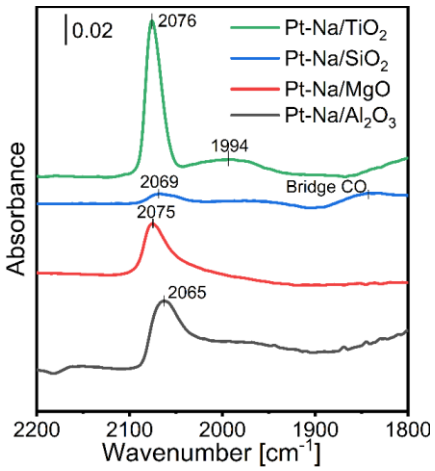

Figure 18. FTIR spectra of CO adsorption for $Pt\text{-}Na/Al_2O_3$, Pt-Na/MgO, $Pt\text{-}Na/SiO_2$, and $Pt\text{-}Na/TiO_2$. Prior to CO adsorption, the catalyst was treated with H_2, and subsequently CO was introduced at –100 °C without exposure to air.

2.3.4 *In situ IR* study using Pt catalysts during CCR operation

To elucidate the high selectivity of Pt-Na/Al_2O_3, *in situ* FTIR measurements were carried out during CCR (Figure 19). Prior to the experiment, self-supported disks were treated with H_2 at 350 °C, and background spectra were obtained under N_2 flow without exposure to air. For Pt/Al_2O_3, two peaks appeared at 1587 and 1341 cm^{-1} during CO_2 absorption, which were assigned to absorbed CO_2, possibly monodentate CO_3^{2-}.[56,57] After the flow gas was altered from 1% CO_2/10% O_2/N_2 to 5% H_2/N_2 (t = 0 min), the two peaks decreased in intensity and a new peak derived from on-top CO on metallic Pt was observed at 2048 cm^{-1}; this peak remained to be observed for 30 min (Figure 19a). When Pt-Na/Al_2O_3 was used instead of Pt/Al_2O_3, much higher peaks derived from CO_3^{2-} were observed during CO_2 capture, confirming that CO_2 absorption ability was enhanced (Figure 19b). Notably, during successive reduction, a very small band assignable to on-top CO was observed at 1 and 10 min, then no adsorbed CO species were observed at 30 min whilst the peak intensities for adsorbed CO_3^{2-} continuously decreased (Figure 19c). In the case of Pt-Mg/Al_2O_3, the band derived from on-top CO on Pt sites was clearly observed in the range of 2060–2030 cm^{-1} during successive reduction (Figure 19d). The results of the *in situ* FTIR indicated that the adsorption of the formed CO was suppressed over Na-modified Pt NPs. The suppression of CO adsorption over Na-promoted metal NPs has previously been reported in several papers.[50,58]

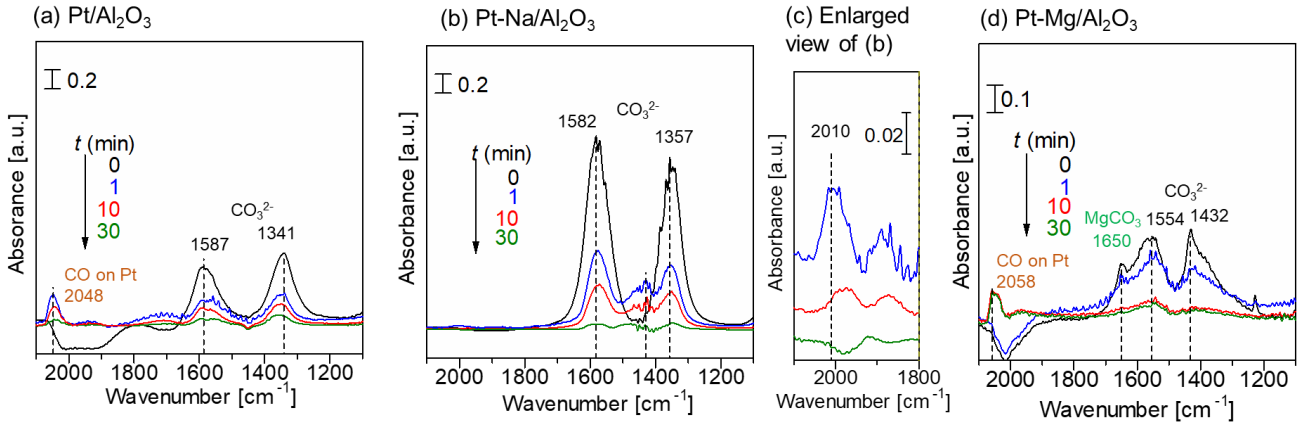

Figure 19. *In situ* FTIR measurements during CCR for (a) Pt/Al_2O_3, (b and c) Pt-Na/Al_2O_3, and (d) Pt-Mg/Al_2O_3. The background spectra were taken before CO_2 capture. After CO_2 capture for 5 min under CO_2/O_2 flow (100 mL/min of 1% CO_2/10% O_2/N_2), the flow gas was changed to H_2 (100 mL/min of 5% H_2/N_2). The time (t) denotes the period of reduction with H_2.

Based on all the results and discussions, the high efficiency of Pt-Na/Al_2O_3 are interpreted as follows. The impregnation of Pt species on Na/Al_2O_3 and calcination induced the formation of small Pt-Na ternary oxides. Following H_2 treatment, the Pt species were reduced to form Na-modified Pt NPs. The Na species on the Pt NPs served as CO_2 capture sites adjacent to the Pt NPs, where absorbed CO_2 species were efficiently reduced by H_2. In addition, the adsorption of generated CO was effectively inhibited because the surface of Pt NPs was modified by Na species, suppressing the successive reduction of CO to CH_4, which is regarded as a key step for CH_4 formation by CO_2 hydrogenation.[59–61] To discuss the impact of surface structures on catalytic performance, a series of Pt-Na/Al_2O_3 catalysts with different Pt

and Na loadings were prepared (Pt(X)-Na(Y)/Al_2O_3, where X and Y denoted the loading amounts of Pt and Na_2O, respectively). These were then compared in the CCR reaction and FTIR measurements with CO adsorption at -100 °C (Figure 20); note that Pt(1)-Na(3)/Al_2O_3 corresponded to the Pt-Na/Al_2O_3 as studied above. With an increase in Pt loading from 1 wt% to 3 and 10 wt% (Pt(3)-Na(3) and Pt(10)-Na(3)/Al_2O_3), the Sel_{CO} decreased from 93% to 30% and 17%, respectively, and the $C_{CO}max$ dropped from 1559 ppm to 142 and 39 ppm, respectively. When Pt(1)-Na(1)/Al_2O_3 with lower Na loading was used, Sel_{CO} and $C_{CO}max$ were moderate to low (59% and 264 ppm, respectively). In the CO adsorption experiments, the linearly adsorbed CO molecules on the terrace of Pt sites were observed at approximately 2080–2100 cm^{-1} for Pt(3)-Na(3), Pt(10)-Na(3), and Pt(1)-Na(1)/Al_2O_3 (Figure 20). This is in sharp contrast to the FTIR spectrum for Pt(1)-Na(3)/Al_2O_3 as discussed above (Figure 4). *In situ* FTIR measurements during the reduction of captured CO_2 with H_2 for Pt(1)-Na(1)/Al_2O_3, Pt(3)-Na(9)/Al_2O_3, and Pt(10)-Na(3)/Al_2O_3 (Figure 21) showed that the adsorbed CO species were clearly observed in the range of 1950-2060 cm^{-1}, which is also quite different from the result of Pt(1)-Na(3)/Al_2O_3. The high selectivity for CO formation over Pt(1)-Na(3)/Al_2O_3 is ascribed to the effective modification of terrace Pt sites with Na species.

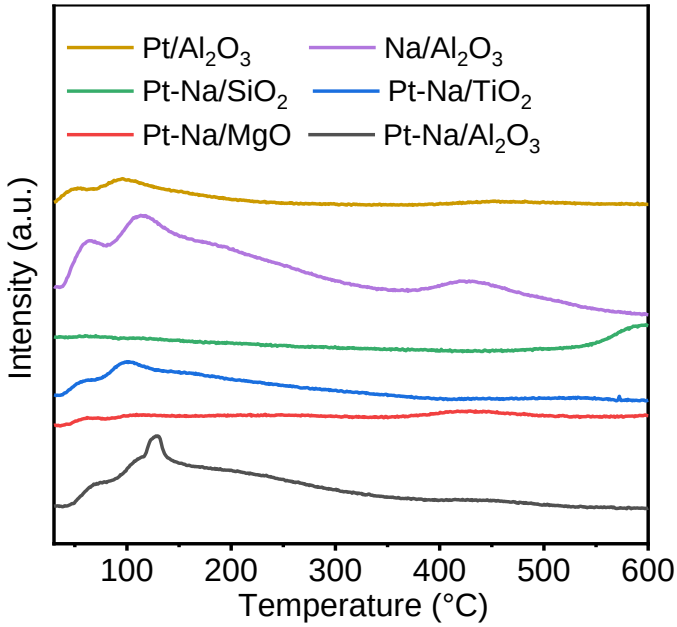

Figure 20. TPD profiles of Na-modified Pt NPs supported on different supports. Conditions: 100 mg sample, 350 °C pretreated by N_2 for 30 min, flow 1%CO_2/N_2 at room temperature for 30 min, increase temperature to 600 °C in 1 h under a N_2 flow.

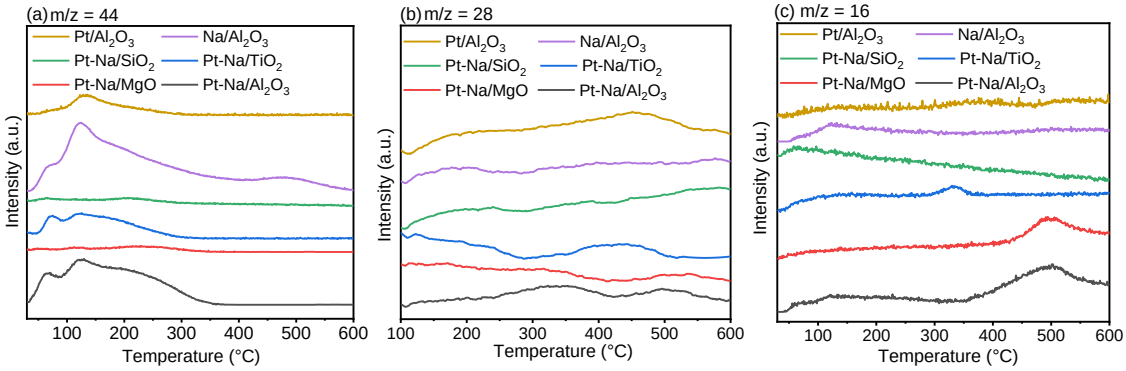

Figure 21. TPSR profiles of Na-modified Pt NPs supported on different supports. Conditions: 100 mg sample, 350 °C pretreated by H_2 for 30 min, following with cool down to room temperature and capture 1% CO_2/10% O_2/N_2 (100 mL min^{-1}), and then increase temperature to 600 °C with 5% H_2/N_2 (100 mL min^{-1}) in 1 h under a N_2 flow.

2.3.5 Long term continuous CCR operation

Finally, a continuous CCR operation was demonstrated using the optimized Pt-Na/Al_2O_3 (Pt(1)-Na(3)/Al_2O_3). Two reactors containing the same amount of Pt-Na/Al_2O_3 were set in parallel, where one reactor (reactor A or B) captured CO_2 from the mixture with O_2 while the other (reactor B or A) reduced the captured CO_2 (Figure 22a). By switching the two valves on the top and bottom of the reactors at the same interval time, the continuous CCR operation was carried out. As such, two effluent gases containing uncaptured CO_2 (effluent 1) and generated CO/CH_4 (effluent 2) were continuously collected, as per the monitoring by FTIR spectroscopy with gas cells. The protocol and reactor system for continuous operation were previously proposed by Urakawa et al.[29], as mentioned in the Introduction. The following two gases were switched on every 30 s: CO_2 capture (0.5% CO_2/10% O_2/N_2, 100 mL/min) and reduction (H_2, 100 mL/min). For comparison, the CCR operation using one reactor was first tested. A 0.3 g of Pt-Na/Al_2O_3 was put in the reactor A while reactor B contains only sea sand. As shown in Figure 22b, the concentration of uncaptured CO_2 was ranged from 800 ppm to 3500 ppm (effluent 1). The highest concentration of formed CO and CH_4 were 3500 ppm and 120 ppm, respectively (effluent 2). At the same time, the concentration of desorbed CO_2 was ranged from 250 ppm to 1100 ppm. Figure 22c shows the results of continuous CCR operation using two reactors containing the same amount of Pt-Na/Al_2O_3 under the same conditions. In contrast to the case of CCR using one reactor, the concentration of uncaptured CO_2 remained about 540 ppm (effluent 1). In the context of the formation of CO and CH_4 (effluent 2), the concentration of CO ranged from 2500 to 4200 ppm, while the concentration of CH_4 remained below 200 ppm. The desorbed CO_2 was continuously detected in the range of 500 to 1200 ppm. The conversion of H_2 ranged from 20% to 30%. Notably, the continuous CCR operation was carried out for at least 100 h (corresponding to 6000 cycles), without a significant decrease in CO_2 capture ability and the productivity of CO (Figure d). The CCR operation using two reactors and switching the reactant/effluent gases in same interval time allows continuous CO_2 capture and CO production, contributing to both emission reduction and the utilization of diluted CO_2. The effect of steam on continuous CCR operation over Pt-Na/Al_2O_3 was also investigated. For this purpose, 3% or 20% water vapor was co-fed using a water bubbler in a heater (25 or 60 °C, corresponding to 3 and 20% water vapor). Although the decrease of CO_2 absorption ability was relatively small, the concentration of generated CO significantly decreased from 2500-4500 ppm to 1800-2000 and 1000-1500 ppm by co-feeding of 3% and 20% water vapor, respectively, with maintaining high CO selectivity. Besides, the concentration of desorbed CO_2 increased with the increase in water vapor

concentration. Although the high CO selectivity was maintained, the CO productivity decreased in the presence of steam, indicating the necessity of removal of water in the real-world application (e.g. exhaust gases from natural gas plant).

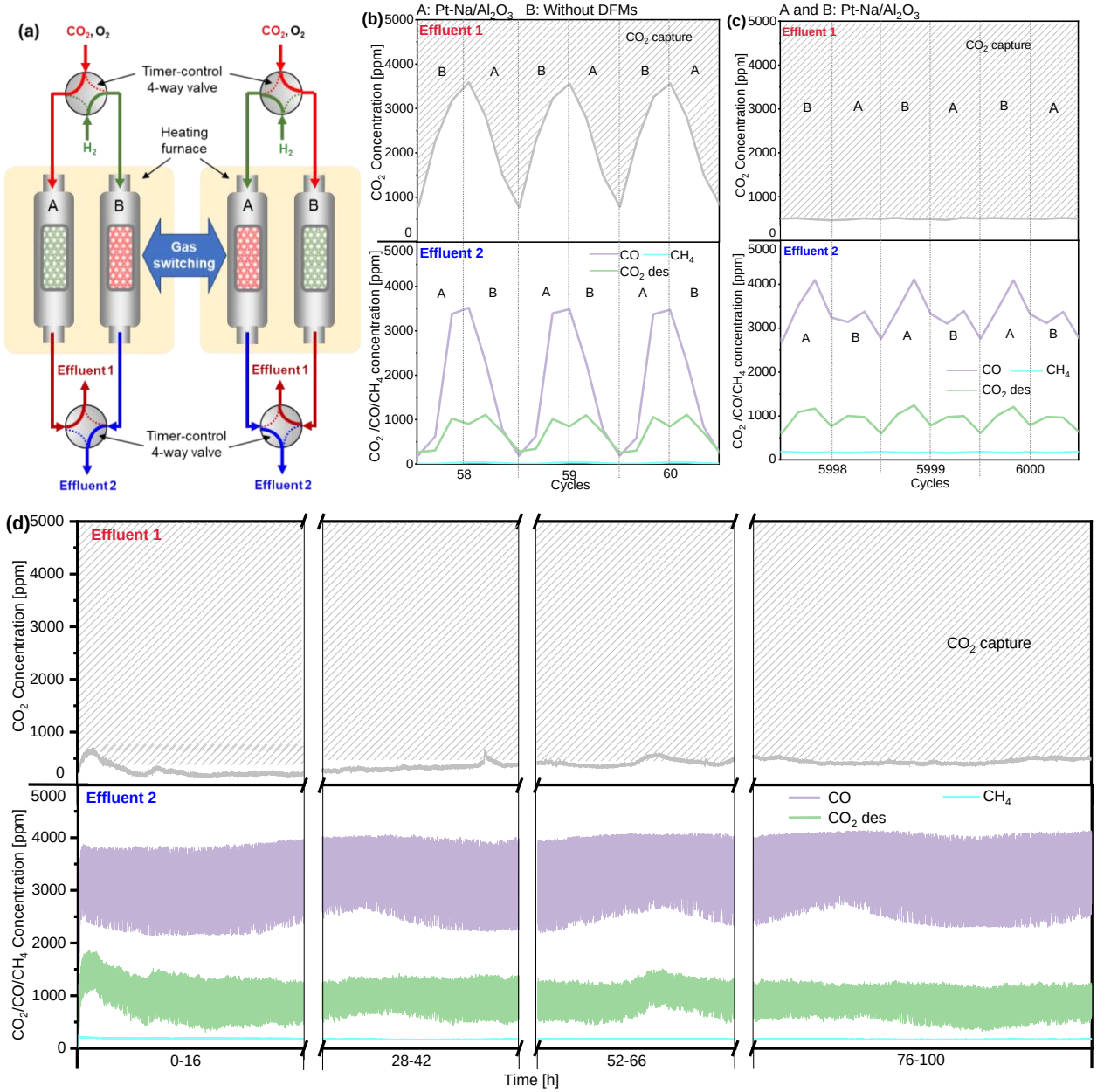

Figure 22. (a) Protocol and reactor system of continuous CCR operation. (b and c) Effluent gas composition for continuous CCR operation (b) using one reactor (reactor A: Pt-Na/Al_2O_3, reactor B: Without DFMs), and (c) using two reactors (reactor A and B: Pt-Na/Al_2O_3) Conditions: 0.3 g of Pt-Na/Al_2O_3 for each reactor, 350 °C, 100 mL/min of 0.5% CO_2/10% O_2/N_2 for 30 s, switched to 100 mL/min of H_2 for the other 30 s. (d) Long-term CCR operation using double reactors for 100 h (6000 cycles).

2.3.6 CCR performance of Cs-based DFMs

Several basic metal oxides were also screened at 500 °C to determine the optimal DFMs for the continuous CCR to CO process. For the continuous CCR to CO, homemade reaction system was used (Figure 23a). Initially, the 1%CO_2+10%O_2/He mixture is fed into DFMs, while pure H_2 were fed into the other reactor at 500 ºC. The concentration profile of uncaptured CO_2 in effluent 1 and product (CO, CH_4 and desorbed CO_2) in effluent 2 over blank tube and Cs(16)/Al_2O_3 were shown Figure 23b and c, respectively. As expected, feed CO_2 was observed (from 0.98% to 1.00 % concentration) was observed in effluent 1, while low concentration of CO_2 (from 0.00 % to 0.02 %) remaining in the reactor and gas line was detected in effluent 2. In contrast to the case of blank test, the uncaptured CO_2 concentration in effluent 1 remaining range from 0.00 to 0.02 %. In the context of the product in effluent 2, the concentration of CO ranged from 0.80 to 1.20 %, whereas the concentration of CH4 was below detectable limitation. Figure 23d summarizes the continuous CCR performance of the various DFMs. Al2O3 and Cs_2CO_3 exhibited low CO yield. While Cs(16)/Al_2O_3 exhibited high CO yield (86 %). Cs(16)/Al_2O_3 was compared with Pt and Na co-loaded DFM (Pt-Na/Al_2O_3) and Ni and Rb co-loaded DFM, which have been developed our group as one of the most effective transition-metal DFMs for CCR to CO. Pt-Na/Al_2O_3 shows lower CO yield (60 %) at 350 ºC, which is reported condition temperature, and further lower CO yield (50 %) at 500 ºC. Rb-Ni/Al_2O_3 also shows lower CO yield. Furthermore, these transition metal loaded DFMs produce large amounts of CH_4 and show lower CO selectivity at 500 ºC (Pt-Na/Al_2O_3 = 50 % and Rb-Ni/Al_2O_3 = 40 %, respectively), compared with Cs(16)/Al_2O_3 (99 %).

Next, we compared the CCR performance of the M/Al_2O_3 (M represents alkali, alkaline earth, and rare earth such as Cs, Rb, K, Na, Ba and La. These components exhibit strong basicity.) samples containing almost equimolar (1.17 mmol/g) loadings (Figure 1e). Mulliken electron negativity (EN) was used for the X-axis in Figure 23e as an indicator of the strength of basicity. When the Mulliken EN was increased from 2.18 (Cs(16)/Al_2O_3) to 3.06 (La(16)/Al_2O_3), the CO yield monotonically decreased. These results imply that strong base loading was effective for continuous CCR. We then compared the continuous CCR performances of the Cs/Al_2O_3 samples containing different Cs loading. The CO yield slightly increased with increasing Cs loading up to 8 wt% (from 0 (Al_2O_3) to 10 % (Cs(8)/Al_2O_3)), and drastically increased with further increasing Cs loading to 12 and 16 wt% (82%, both).

Using the optimal DFM, Cs(16)/Al_2O_3, the continuous CCR performance was evaluated at different temperatures (data not shown). Increase in the temperature from 300 to 600 °C

resulted in monotonic increase in the CO_2 capture efficiency (from 71 to 100%), while CO yield was little increased between 300 and 400 °C (3 and 4 %, respectively), but sharply increased upon heating to 500 °C (81 %). Under a suitable temperature at 500 °C with the best DFM, $Cs(16)/Al_2O_3$, switching time of upper and bottom valves was optimized for the continuous CCR experiments (data not shown). Middle switching time (every 30 sec) gives the highest CO_2 capture efficiency and CO yield simply because with a shorter switching time such as every 10 sec, the reduction time is insufficient, in contrast with a longer switch time (over 60 sec), it exceeds the CO_2 capacity of $Cs(16)/Al_2O_3$.

We also performed stepwise CCR (traditional CCR) reaction tests at 500 ºC (data not shown). The dependence on the loaded alkali metal, (alkaline earth metal or, rare earth metal) oxide and the Cs loading amount showed similar trends to the continuous CCR reaction test, with the highest CO_2 capture amount, CO selectivity, amount of CO production, and max CO production rate. To determine the turnover frequency (TOF_M), the transient rates per unit weight of the DFM were divided by the number of alkali metal, (alkaline earth metal or, rare earth metal) atom per unit weight of the DFM (Figure 24). As plotted in Figure 24a when the Mulliken EN was increased, the TOF_M monotonically decreased from 9.2 ($Cs(16/Al_2O_3)$) to 0.8 h^{-1} ($La(16)/Al_2O_3$). These results possibly implied that alkali metals were active sites for the CCR. Figure 24b plots the TOF_M as a function of the Cs loading. These results showed that the TOF_M was increased with increasing Cs loading from 3 to 12 wt%. This suggests that the nature of active sites was similar ranged from 3 to 16 wt% Cs loading but different from that of $Cs(37)/Al_2O_3$.

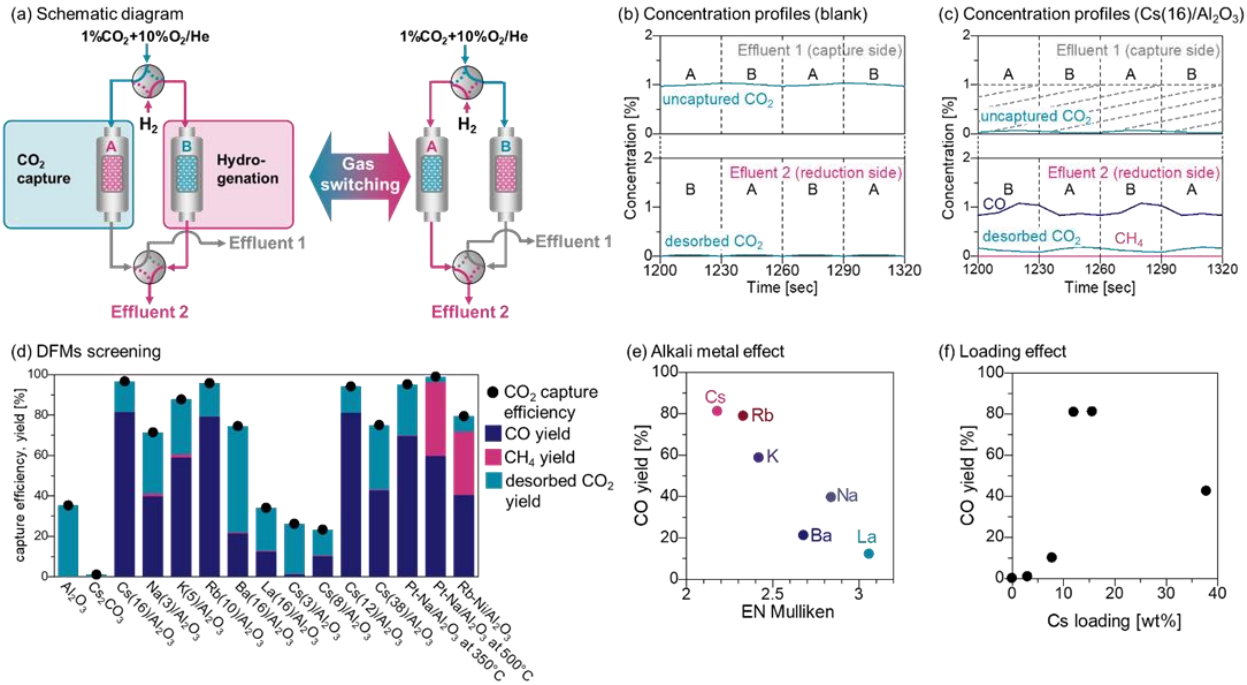

Figure 23. (a) Outline of the protocol and the two-reactor system for the continuous CCR to CO. Examples showing effluent concentration profiles for (b) blank and (c) Cs(16)/Al_2O_3. (d) CO_2 capture efficiency, product (CO, CH_4 and desorbed CO_2) yield in the CCR to CO. Conditions: 500 °C, 100 mL min^{-1} flow rate, 1%CO_2+10%O_2/He for another 30 sec. Variation in CO yield based on inlet CO_2 with respect to (e) loaded species of alkali, alkaline earth and rare earth, and (f) Cs loading.

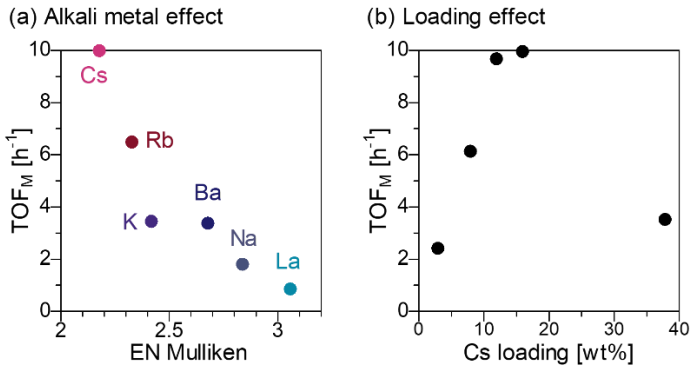

Figure 24. Variation in TOF per amount of alkali metal respect to (a) Mulliken's electron negativity, and (b) Cs loading.

2.4 Conclusions

In summary, this study successfully developed Pt-Na/Al_2O_3 as an effective DFM for selective CO formation through CCR at a mild reaction temperature (350 °C). Among the basic promoters tested, Na was the best for CO formation, while Mg resulted in the lowest CO selectivity. Notably, the optimized Pt-Na/Al_2O_3 was applicable to continuous CCR operation, where CO_2 capture capacity and CO productivity were maintained for at least 100 h. We also conducted a comprehensive characterization of Pt, Pt-Na, and Pt-Mg/Al_2O_3 using microscopic (STEM, EDX) and spectroscopic (XRD, XAS, XPS, FTIR) techniques. The Na-modified Pt NPs were formed in Pt-Na/Al_2O_3, while the Mg species remained in a highly dispersed state on Al_2O_3 in Pt-Mg/Al_2O_3. The electronic states of the Pt NPs were slightly affected by basic promoters regardless of whether or not modified structures had formed. We also conducted *in situ* FTIR measurements during CCR, where the adsorbed CO species were hardly observed over Pt-Na/Al_2O_3. The Na species on Pt NPs not only served as CO_2 absorption sites but also suppressed the adsorption of generated CO, leading to high selectivity for CO. These results reveal the effect of basic promoters on the surface structures of metal NPs and product selectivity, demonstrating the importance of the choice and loading of basic promoters during the development of DFMs for CO_2 capture and reduction. Unfortunately, the CO productivity of present DFM system decreased in the presence of steam although the high CO selectivity retained. Therefore, now we are devoting further optimization of Pt-Na/Al_2O_3 DFMs and CCR operation conditions to adapt real-world applications, such as higher CO_2 concentration conditions and/or in the presence of steam.

2.5 References

(1) Gough, C. State of the Art in Carbon Dioxide Capture and Storage in the UK: An Experts' Review. *Int. J. Greenh. Gas Control* **2008**, *2*, 155–168.

(2) Varghese, A. M.; Karanikolos, G. N. CO_2 Capture Adsorbents Functionalized by Amine – Bearing Polymers: A Review. *Int. J. Greenh. Gas Control* **2020**, *96*, 103005.

(3) Keshavarz, L.; Ghaani, M. R.; MacElroy, J. M. D.; English, N. J. A Comprehensive Review on the Application of Aerogels in CO_2-Adsorption: Materials and Characterisation. *Chem. Eng. J.* **2021**, *412*, 128604.

(4) Yang, H.; Xu, Z.; Fan, M.; Gupta, R.; Slimane, R. B.; Bland, A. E.; Wright, I. Progress in Carbon Dioxide Separation and Capture: A Review. *J. Environ. Sci.* **2008**, *20*, 14–27.

(5) Kolle, J. M.; Fayaz, M.; Sayari, A. Understanding the Effect of Water on CO_2 Adsorption. *Chem. Rev.* **2021**, *121*, 7280–7345.

(6) Balat, H.; Öz, C. Technical and Economic Aspects of Carbon Capture and Storage - A Review. *Energy Explor. Exploit.* **2007**, *25*, 357–392.

(7) Dunstan, M. T.; Donat, F.; Bork, A. H.; Grey, C. P.; Müller, C. R. CO_2 Capture at Medium to High Temperature Using Solid Oxide-Based Sorbents: Fundamental Aspects, Mechanistic Insights, and Recent Advances. *Chem. Rev.* **2021**, *121*, 12681–12745.

(8) Li, D.; Xu, R.; Gu, Z.; Zhu, X.; Qing, S.; Li, K. Chemical-Looping Conversion of Methane: A Review. *Energy Technol.* **2019**, *1900925*, 1–28.

(9) Zhu, X.; Imtiaz, Q.; Donat, F.; Müller, C. R.; Li, F. Chemical Looping beyond Combustion-a Perspective. *Energy Environ. Sci.* **2020**, *13*, 772–804.

(10) Buelens, L. C.; Poelman, H.; Marin, G. B.; Galvita, V. V. 110th Anniversary: Carbon Dioxide and Chemical Looping: Current Research Trends. *Ind. Eng. Chem. Res.* **2019**, *58*, 16235–16257.

(11) Kim, S. M.; Abdala, P. M.; Broda, M.; Hosseini, D.; Copéret, C.; Müller, C. Integrated CO_2 Capture and Conversion as an Efficient Process for Fuels from Greenhouse Gases. *ACS Catal.* **2018**, *8* (4), 2815–2823.

(12) Al-Mamoori, A.; Rownaghi, A. A.; Rezaei, F. Combined Capture and Utilization of CO_2 for Syngas Production over Dual-Function Materials. *ACS Sustain. Chem. Eng.* **2018**, *6* (10), 13551–13561.

(13) Daza, Y. A.; Kuhn, J. N. CO_2 Conversion by Reverse Water Gas Shift Catalysis: Comparison of Catalysts, Mechanisms and Their Consequences for CO_2 Conversion to Liquid Fuels. *RSC Adv.* **2016**, *6*, 49675–49691.

(14) Zeng, D.; Qiu, Y.; Ma, L.; Li, M.; Cui, D.; Zhang, S.; Xiao, R. Tuning the Support Properties toward Higher CO_2 Conversion during a Chemical Looping Scheme. *Environ. Sci. Technol.* **2020**, *54*, 12467–12475.

(15) Daza, Y. A.; Maiti, D.; Kent, R. A.; Bhethanabotla, V. R.; Kuhn, J. N. Isothermal Reverse Water Gas Shift Chemical Looping on $La_{0.75}Sr_{0.25}Co_{(1-Y)}FeYO_3$ Perovskite-Type Oxides. *Catal. Today* **2015**, *258*, 691–698.

(16) Makiura, J. I.; Higo, T.; Kurosawa, Y.; Murakami, K.; Ogo, S.; Tsuneki, H.; Hashimoto, Y.; Sato, Y.; Sekine, Y. Fast Oxygen Ion Migration in Cu-In-Oxide Bulk and Its Utilization for Effective CO_2 conversion at Lower Temperature. *Chem. Sci.* **2021**, *12*, 2108–2113.

(17) Keller, M.; Otomo, J. CO Production from CO_2 and H_2 via the RWGS Reaction by Thermochemical Redox Cycling in Interconnected Fluidized Beds. *J. CO_2 Util.* **2020**, *40*, 101191.

(18) Dharanipragada, N. V. R. A.; Buelens, L. C.; Poelman, H.; De Grave, E.; Galvita, V. V.; Marin, G. B. Mg-Fe-Al-O for Advanced CO_2 to CO Conversion: Carbon Monoxide Yield vs. Oxygen Storage Capacity. *J. Mater. Chem. A* **2015**, *3*, 16251–16262.

(19) Wenzel, M.; Rihko-Struckmann, L.; Sundmacher, K. Continuous Production of CO from CO_2 by RWGS Chemical Looping in Fixed and Fluidized Bed Reactors. *Chem. Eng. J.* **2018**, *336*, 278–296.

(20) Veselovskaya, J. V.; Lysikov, A. I.; Netskina, O. V.; Kuleshov, D. V.; Okunev, A. G. K_2CO_3-Containing Composite Sorbents Based on Thermally Modified Alumina: Synthesis, Properties, and Potential Application in a Direct Air Capture/Methanation Process. *Ind. Eng. Chem. Res.* **2020**, *59* (15), 7130–7139.

(21) Park, S. J.; Bukhovko, M. P.; Jones, C. W. Integrated Capture and Conversion of CO_2 into Methane Using $NaNO_3$/MgO + Ru/Al_2O_3 as a Catalytic Sorbent. *Chem. Eng. J.* **2021**, *420*, 130369.

(22) Sun, H.; Zhang, Y.; Guan, S.; Huang, J.; Wu, C. Direct and Highly Selective Conversion of Captured CO_2 into Methane through Integrated Carbon Capture and Utilization over Dual Functional Materials. *J. CO_2 Util.* **2020**, *38*, 262–272.

(23) Veselovskaya, J. V.; Derevschikov, V. S.; Kardash, T. Y.; Stonkus, O. A.; Trubitsina, T. A.; Okunev, A. G. Direct CO2 Capture from Ambient Air Using K2CO3/Al2O3 Composite Sorbent. *Int. J. Greenh. Gas Control* **2013**, *17*, 332–340.

(24) Duyar, M. S.; Treviño, M. A. A.; Farrauto, R. J. Dual Function Materials for CO_2 Capture and Conversion Using Renewable H_2. *Appl. Catal. B Environ.* **2015**, *168–169*, 370–376.

(25) Duyar, M. S.; Wang, S.; Arellano-Treviño, M. A.; Farrauto, R. J. CO_2 Utilization with a Novel Dual Function Material (DFM) for Capture and Catalytic Conversion to Synthetic Natural Gas: An Update. *J. CO_2 Util.* **2016**, *15*, 65–71.

(26) Mechanism of the CO_2 Storage and in Situ Hydrogenation to CH_4. Temperature and Adsorbent Loading Effects over Ru-CaO/Al_2O_3 and Ru-Na_2CO_3/Al_2O_3 Catalysts. *Appl. Catal. B Environ.* **2019**, *256*, 117845.

(27) Hu, L.; Urakawa, A. Continuous CO_2 Capture and Reduction in One Process: CO_2 Methanation over Unpromoted and Promoted Ni/ZrO_2. *J. CO_2 Util.* **2018**, *25*, 323–329.

(28) Bobadilla, L. F.; Riesco-García, J. M.; Penelás-Pérez, G.; Urakawa, A. Enabling Continuous Capture and Catalytic Conversion of Flue Gas CO_2 to Syngas in One Process. *J. CO_2 Util.* **2016**, *14*, 106–111.

(29) Hyakutake, T.; Van Beek, W.; Urakawa, A. Unravelling the Nature, Evolution and Spatial Gradients of Active Species and Active Sites in the Catalyst Bed of Unpromoted and K/Ba-Promoted Cu/Al_2O_3 during CO_2 Capture-Reduction. *J. Mater. Chem. A* **2016**, *4*, 6878–6885.

(30) Mizutani, Y.; Hirota, Y.; Yamauchi, T. Methane Production System. July 2020, WO 016007825.

(31) Sakai, M.; Imagawa, H.; Mizutani, Y. Carbon Dioxide Occlusion Reduction Catalyst and Methane Production Method, October 2020, JP2020163248A.

(32) Sun, H.; Wang, J.; Zhao, J.; Shen, B.; Shi, J.; Huang, J.; Wu, C. Dual Functional Catalytic Materials of Ni over Ce-Modified CaO Sorbents for Integrated CO_2 Capture and Conversion. *Appl. Catal. B Environ.* **2019**, *244*, 63–75.

(33) Jo, S. Bin; Woo, J. H.; Lee, J. H.; Kim, T. Y.; Kang, H. I.; Lee, S. C.; Kim, J. C. CO_2 Green Technologies in CO_2 Capture and Direct Utilization Processes: Methanation, Reverse Water-Gas Shift, and Dry Reforming of Methane. *Sustain. Energy Fuels* **2020**, *4*, 5543–5549.

(34) Wang, S.; Farrauto, R. J.; Karp, S.; Jeon, J. H.; Schrunk, E. T. Parametric, Cyclic Aging and Characterization Studies for CO_2 Capture from Flue Gas and Catalytic Conversion to Synthetic Natural Gas Using a Dual Functional Material (DFM). *J. CO_2 Util.* **2018**, *27*, 390–397.

(35) Omodolor, I. S.; Otor, H. O.; Andonegui, J. A.; Allen, B. J.; Alba-Rubio, A. C. Dual-Function Materials for CO_2 Capture and Conversion: A Review. *Ind. Eng. Chem. Res.* **2020**, *59* (40), 17612–17631.

(36) Sun, S.; Sun, H.; Williams, P. T.; Wu, C. Recent Advances in Integrated CO_2 capture and Utilization: A Review. *Sustain. Energy Fuels* **2021**, *5* (18), 4546–4559.

(37) Bermejo-López, A.; Pereda-Ayo, B.; González-Marcos, J. A.; González-Velasco, J. R. Ni Loading Effects on Dual Function Materials for Capture and In-Situ Conversion of CO_2 to CH_4 Using CaO or Na_2CO_3. *J. CO_2 Util.* **2019**, *34* (May), 576–587.

(38) Arellano-Treviño, M. A.; He, Z.; Libby, M. C.; Farrauto, R. J. Catalysts and Adsorbents for CO_2 Capture and Conversion with Dual Function Materials: Limitations of Ni-Containing DFMs for Flue Gas Applications. *J. CO_2 Util.* **2019**, *31*, 143–151.

(39) Kosaka, F.; Liu, Y.; Chen, S. Y.; Mochizuki, T.; Takagi, H.; Urakawa, A.; Kuramoto, K. Enhanced Activity of Integrated CO_2 Capture and Reduction to CH_4 under Pressurized Conditions toward Atmospheric CO_2 Utilization. *ACS Sustain. Chem. Eng.* **2021**, *9*, 3452–3463.

(40) González-Castaño, M.; Dorneanu, B.; Arellano-García, H. The Reverse Water Gas Shift Reaction: A Process Systems Engineering Perspective. *React. Chem. Eng.* **2021**, *6*, 954–976.

(41) Porosoff, M. D.; Yan, B.; Chen, J. G. Catalytic Reduction of CO_2 by H_2 for Synthesis of CO, Methanol and Hydrocarbons: Challenges and Opportunities. *Energy Environ. Sci.* **2016**, *9*, 62–73.

(42) Ravel, B.; Newville, M. ATHENA, ARTEMIS, HEPHAESTUS: Data Analysis for X-Ray Absorption Spectroscopy Using IFEFFIT. *J. Synchrotron Radiat.* **2005**, *12*, 537–541.

(43) Lundwall, M. J.; McClure, S. M.; Goodman, D. W. Probing Terrace and Step Sites on Pt Nanoparticles Using Co and Ethylene. *J. Phys. Chem. C* **2010**, *114* (17), 7904–7912.

(44) Siemer, M.; Tomaschun, G.; Klüner, T.; Christopher, P.; Christopher, P.; Al-Shamery, K. Insights into Spectator-Directed Catalysis: CO Adsorption on Amine-Capped Platinum Nanoparticles on Oxide Supports. *ACS Appl. Mater. Interfaces* **2020**, *12*, 27765–27776.

(45) Hossain, M. J.; Rahman, M. M.; Jafar Sharif, M. Preference for Low-Coordination Sites by Adsorbed CO on Small Platinum Nanoparticles. *Nanoscale Adv.* **2020**, *2* (3), 1245–1252.

(46) Wang, C.; Li, Y.; Zheng, L.; Zhang, C.; Wang, Y.; Shan, W.; Liu, F.; He, H. A Nonoxide Catalyst System Study: Alkali Metal-Promoted Pt/AC Catalyst for Formaldehyde Oxidation at Ambient Temperature. *ACS Catal.* **2021**, *11*, 456–465.

(47) Zhu, X.; Shen, M.; Lobban, L. L.; Mallinson, R. G. Structural Effects of Na Promotion for High Water Gas Shift Activity on Pt-Na/TiO_2. *J. Catal.* **2011**, *278* (1), 123–132.

(48) Ding, K.; Gulec, A.; Johnson, A. M.; Schweitzer, N. M.; Stucky, G. D.; Marks, L. D.; Stair, P. C. Identification of Active Sites in CO Oxidation and Water-Gas Shift over Supported Pt Catalysts. *Science.* **2015**, *350*, 189–192.

(49) Wnuk, R. C.; Touw, T. R.; Post, B. The Crystal Structure of $CaPt_3O_4$. *IBM J. Res. Dev.* **2010**, *8*, 185–186.

(50) Zhai, Y.; Pierre, D.; Si, R.; Deng, W.; Ferrin, P.; Nilekar, A. U.; Peng, G.; Herron, J. A.; Bell, D. C.; Saltsburg, H. Alkali-Stabilized Pt-OH_x Species Catalyze Low-Tempereature Water-Gas Shift Reactions. *Science.* **2010**, *329*, 1633–1636.

(51) Yoshitake, H.; Iwasawa, Y. Study on d State of Platinum in Pt/SiO_2 and Na/Pt/SiO_2 Catalysts under C=C Hydrogenation Conditions by X-Ray Absorption near-Edge Structure Spectroscopy. *J. Phys. Chem.* **1991**, *95*, 7368–7372.

(52) Shimizu, K. I.; Shimura, K.; Kato, K.; Tamagawa, N.; Tamura, M.; Satsuma, A. Electronic Effect of Na Promotion for Selective Mono-N-Alkylation of Aniline with Di-Iso-Propylamine by Pt/SiO_2 Catalysts. *J. Mol. Catal. A Chem.* **2012**, *353–354*, 171–177.

(53) Zhang, G.; Wu, L.; Tang, A.; Chen, X. B.; Ma, Y.; Long, Y.; Peng, P.; Ding, X.; Pan, H.; Pan, F. Growth Behavior of MgAl-Layered Double Hydroxide Films by Conversion of Anodic Films on Magnesium Alloy AZ31 and Their Corrosion Protection. *Appl. Surf. Sci.* **2018**, *456*, 419–429.

(54) Harada, T.; Simeon, F.; Hamad, E. Z.; Hatton, T. A. Alkali Metal Nitrate-Promoted High-Capacity MgO Adsorbents for Regenerable CO_2 Capture at Moderate Temperatures. *Chem. Mater.* **2015**, *27* (6), 1943–1949.

(55) Dal Pozzo, A.; Armutlulu, A.; Rekhtina, M.; Abdala, P. M.; Müller, C. R. CO_2 Uptake and Cyclic Stability of MgO-Based CO_2 Sorbents Promoted with Alkali Metal Nitrates and Their Eutectic Mixtures. *ACS Appl. Energy Mater.* **2019**, *2* (2), 1295–1307.

(56) Busca, G.; Lorenzelli, V. Infrared Spectroscopic Identification of Species Arising from Reactive Adsorption of Carbon Oxides on Metal Oxide Surfaces. *Mater. Chem.* **1982**, *7*, 89–126.

(57) Baltrusaitis, J.; Jensen, J. H.; Grassian, V. H. FTIR Spectroscopy Combined with Isotope Labeling and Quantum Chemical Calculations to Investigate Adsorbed Bicarbonate Formation Following Reaction of Carbon Dioxide with Surface Hydroxyl Groups on Fe_2O_3 and Al_2O_3. *J. Phys. Chem. B* **2006**, *110*, 12005–12016.

(58) Ang, M. L.; Oemar, U.; Saw, E. T.; Mo, L.; Kathiraser, Y.; Chia, B. H.; Kawi, S. Highly Active Ni/XNa/CeO_2 catalyst for the Water-Gas Shift Reaction: Effect of Sodium on Methane Suppression. *ACS Catal.* **2014**, *4*, 3237–3248.

(59) Teramura, K.; Tanaka, T.; Kikkawa, S.; Asakura, H.; Hosokawa, S. Ni−Pt Alloy Nanoparticles with Isolated Pt Atoms and Their Cooperative Neighboring Ni Atoms for Selective Hydrogenation of CO_2 toward CH_4 Evolution: In Situ and Transient Fourier Transform Infrared Studies. *ACS Appl. Nano Mater.* **2020**, *3*, 9633–9644.

(60) Chen, X.; Su, X.; Duan, H.; Liang, B.; Huang, Y.; Zhang, T. Catalytic Performance of the Pt/TiO_2 Catalysts in Reverse Water Gas Shift Reaction: Controlled Product Selectivity and a Mechanism Study. *Catal. Today* **2017**, *281*, 312–318.

(61) Westermann, A.; Azambre, B.; Bacariza, M. C.; Graça, I.; Ribeiro, M. F.; Lopes, J. M.; Henriques, C. Insight into CO_2 Methanation Mechanism over NiUSY Zeolites: An Operando IR Study. *Appl. Catal. B Environ.* **2015**, *174–175*, 120–125.

Chapter 3

CO_2 capture and hydrogenation to CH_4 over Ni-based DFMs

3.1 Introduction

The emission of CO_2 into the atmosphere owing to human activities is recognized as a major contributor to global warming [1–5]. The Paris Agreement established a goal to limit the increase in global average temperature to 2.0 °C by the year 2100. Achieving this target requires a significant reduction in CO_2 emissions from energy- and industry-related sources [6–9]. Carbon capture and utilization (CCU) [10–21], including carbon capture and reduction (CCR) using H_2 or hydrocarbons [22–39], have been proposed to achieve this target. The concept of the CCR reaction involves CO_2 capture and subsequent reduction combined in one process, utilizing an unsteady-state operation. In 2016, Urakawa et al. and Farrauto et al. separately published their works on CCR [24,25]. Alkali and alkaline earth metal components and transition metal co-loaded catalysts (dual functional materials: DFMs) are widely used for CCR operations owing to their high capacity for CO_2 uptake and ability to form metal carbonates. Transition metals, including DFMs, promote carbonate hydrogenation.

Among various CCU strategies, CO_2 capture and methanation using DFMs have proven to be effective for synthesizing carbon-neutral CH_4. Among the alkali and alkaline earth components, calcium oxide is well known to have a good CO_2 capacity and is one of the most suitable alkaline components for CO_2 capture and methanation. Farrauto et al. first proposed Ru-CaO/Al_2O_3 as an efficient DFM for assisting the CCR to CH_4 [25]. Yang et al. reported that the utilization of Ni/CaO-Al_2O_3 led to increased CO_2 conversion and greater selectivity for CH_4 compared to using Ni/Al_2O_3. This improvement was attributed to the coating of the CaO-Al_2O_3 surface by species derived from CO_2 [33]. Alipour et al. reported that CaO loading significantly enhanced the capacity for CO_2 uptake of DFMs.[34] Bermejo-Lopez et al.[35] and Sun et al.[37] studied Ni-Ca DFMs and evaluated the effect of Ni loading. Moreover, they investigated the relationship between the activity and the distance between the catalytic sites and sorbents. Recently, our research group developed Al_2O_3-supported Ni-Ca materials as effective DFMs for CCR to yield CH_4 [38,39]. We found that the Ca-Al mixed oxide phase derived from the mayenite ($Ca_{12}Al_{14}O_{33}$) structure enhanced the CO_2 capture ability of the DFM [38]. In the second study, we optimized the Ca loading in Ni-Ca/Al_2O_3 for the CCR to CH_4 at low temperatures. and demonstrated the conversion of CO_2 captured from air to CH_4 using a system combined with membrane-based direct air capture[39]. Although there have been many attempts to improve CCR performance, the detailed reaction mechanism over Ni-Ca DFMs is still not clear.

In this study, the mechanism of the CCR to CH_4 was investigated using Al_2O_3-supported Ni-Ca DFMs. Initial screening tests for Ca and Ni loading revealed that Ni(10)-

Ca(28)/Al_2O_3 (Ni=10 wt% and Ca=28 wt%) was the most effective material for CCR. Various structural analyses, including X-ray diffraction (XRD), X-ray absorption spectroscopy (XAS), scanning transmission electron microscopy (STEM), and energy-dispersive X-ray (EDX) spectroscopy, were used in our investigation. The resulting structure-property relationships revealed that the Ni nanoparticles and bulk CaO on Al_2O_3 were responsible for the methanation and capture of CO_2. Finally, the Ni oxidation state and formation/decomposition of Ca carbonate were studied using *in situ* XAS/XRD with online gas composition analysis (*operando* XAS/XRD).

3.2 Experimental section

3.2.1 Catalyst preparation

The Ni-Ca/Al_2O_3 catalysts were synthesized using a wetness impregnation method. An appropriate amount of aqueous Ca-$(NO_3)_2 \cdot H_2O$ (AR 98.5%, FUJIFILM WAKO Pure Chemical Corporation) was mixed with commercial γ-Al_2O_3 for impregnation (Ca loading: 8, 14, 20, 28, and 32 wt%) and stirred for 1 h. Subsequently, the mixture was evaporated to dryness at 50°C using a vacuum pump and finally dried overnight at 100°C in air. The obtained powder was calcined at 500°C for 2 h to yield CaO-loaded/Al_2O_3, denoted as Ca/Al_2O_3. Then, a precursor of Ni-Ca/Al_2O_3 (Ni loading: 10 wt%) was prepared by stirring a mixture of Ca/Al_2O_3 with an aqueous
solution of $Ni(NO_3)_2 \cdot 6H_2O$ (AR >99%, FUJIFILM WAKO Pure Chemical Corporation) at room temperature for 1 h, evaporated to dryness at 50°C, and dried overnight at 100°C in air. Ni-Ca/Al_2O_3 catalysts with different Ca loadings were prepared using a similar method and denoted as Ni(x)-Ca(y)/Al_2O_3 (where x and y are the contents of Ni and Ca loadings, respectively).

3.2.2 Characterization

Powder XRD measurements were conducted using a Rigaku MiniFlex II/AP diffractometer with Cu Kα radiation. High-angle annular dark-field scanning transmission electron microscopy (HAADF-STEM) images were recorded on an FEI Titan G2 microscope equipped with an EDX analyzer. X-ray photoelectron spectroscopy (XPS) profiles were measured on a JEOL JPC-9010MC spectrometer in a modified ultrahigh vacuum (UHV) chamber using Mg Ka radiation. All XPS profiles were corrected for charging effects by aligning them with the O 1s peak at 532.0 eV and subsequently analyzed after linear background subtraction. Curve-fitting analysis
was performed using Fityk software version 1.3.1, and the Gaussian function was used for curve fitting. For XPS measurements, catalysts were treated with pure H_2, 2.5% CO_2/He, or 2.5% CO_2/10% O_2/He at 500ºC and then transferred to a chamber without exposure to air using a transfer vessel. Charge correlation was determined using the O 1s peak at 532.0 eV. Ni K-edge X-ray absorption near-edge structure (XANES) and extended X-ray absorption fine structure (EXAFS) measurements were performed on a medium-length hard X-ray bending magnet (BL01B1) beamline at SPring-8 (Harima,
Japan) using a Si (111) double-crystal monochromator (Proposal No. 2023A0713). Ni K-edge XANES and EXAFS studies were performed in a transmission mode. Sample pellets

(*Φ*=diameter of the pellet, *Φ*=10 mm) were treated with pure H_2 or 2.5% CO_2+10%O_2/He at 500 ºC and then transferred to a glove box without exposure to air. The treated pellets were then packed into gasbarrier bags and measured using a beamline. It is noteworthy that Ni K-edge EXAFS spectra were obtained, normalized to units of A^{-1}, and subsequently Fourier transformed over the range of 3.0–12.0 A^{-1}. The XANES and EXAFS spectra were analyzed using Athena software ver. 0.9.25, which is included in the Demeter package [44].

3.2.3 *In situ*/*operando* spectroscopic experiments

In situ XRD measurements were conducted using a Cu Ka radiation source (Rigaku Ultima IV, Rigaku Corporation, Japan). The total flow rate of the gas mixture was 50 mL/min. The sample (100 mg) was pretreated with 5% H_2/N_2 at 500 ºC for 30 min, and for purging, the gas was switched to He. Subsequently, a mixture of 10% CO_2/He was fed into the system at 500 ºC for 30 min until sufficient $CaCO_3$ was formed, He was purged for 20 min, and the flow gas was switched to 5% H_2/N_2 for 40 min.

For the *in situ* and *operando* XANES measurements, a sample pellet prepared using 30 mg of the catalyst (*Φ*=10 mm) was introduced into a quartz cell. This cell was equipped with Kapton film windows and gas lines connected to a high-sampling-rate thermal conductivity detector gas chromatograph (TCD GC, 490 Micro GC; Agilent Technologies Inc.). The total flow rate of the gas mixture was set to 100 mL/min. The sample pellet was heated to 500°C in He, and the gas was switched to 10% H_2/He for pretreatment for 30 min. A reaction gas containing CO_2 (2.5% CO_2/He) was allowed to flow for 5 min. Subsequently, a reaction gas containing H_2 (10% H_2/He) was introduced and allowed to flow for 30 min. Then, the reaction gas was changed to 2.5% CO_2+10% O_2/He for 6 min. Finally, the flow gas changed again to 10% H_2/He for 21 min. For the linear combination fitting (LCF) analysis, Ni foil and NiO were used as reference compounds for Ni^0 and Ni^{2+}, respectively.

3.2.4 CCR operation

The CCR was performed in a vertical quartz fixed-bed flow reactor. A catalyst (300 mg) was placed on quartz wool in the middle of the reactor, which was set in an electric tube furnace and heated to 500 ºC under a N_2 flow (100 mL/min). Then, the catalyst was reduced under H_2 (100 mL/min) for 30 min at 500 ºC. A reaction gas containing 2.5% CO_2+10% O_2/N_2 was fed into the reactor at a flow rate of 100 mL/min for 5 min to capture CO_2, and then the feeding gas was switched to H_2 (100 mL/min) for 15 min to reduce the adsorbed CO_2. The composition (CO, CH_4, and CO_2) of the effluent gas was quantitatively analyzed using an FTIR spectrometer (JASCO FT/IR-4600) combined with a gas cell. Calculation of CO_2 adsorption capacity (CO2 ad.), the amount of produced CH_4 or CO (CH_4 or CO production),

the selectivity for CH_4 ($Sel._{CH4}$) and the yield of CH4 based on the amount of adsorbed CO_2 (CH_4 yield) are described as follows:

$$CO_2 \text{ ad. } (\mu\text{mol g}^{-1}) = \frac{\int_0^{t_a} [F^{in}_{CO_2}(t) - F^{out}_{CO_2}(t)]dt}{m} \quad (1)$$

$$CH_4 \text{ or CO production } (\mu\text{mol g}^{-1}) = \frac{\int_0^{t_H} F^{out}_{CH_4 \text{ or CO}}(t)dt}{m} \quad (2)$$

$$Sel._{CH4} (\%) = \frac{CH_4 \text{ prod.}}{CH_4 \text{ prod.} + CO \text{ prod.}} \times 100 \quad (3)$$

$$CH_4 \text{ yield } (\%) = \frac{CH_4 \text{ prod.}}{CO_2 \text{ ad}} \times 100, \quad (4)$$

where F^{in}_{CO2} and F^{out}_{CO2} are the CO_2 molar flow rates at the column inlet and outlet, respectively, F^{out}_{CO} and F^{out}_{CH4} are the CO and CH_4 molar flow rates at the column outlet, respectively, *m* is the catalyst mass, t_a is the duration of the adsorption stage, and t_H is the duration of the H2 reduction process.

3.3 Results and discussion

3.3.1 Catalytic Performance

In a typical CCR experiment conducted in this study, a DFM was evaluated for CO_2 capture from a flow of model combustion exhaust (2.5% CO_2/10% O_2/N_2) for 5 min, followed by the reduction of the captured CO_2 with H_2 for 15 min under isothermal conditions (500 ºC). Figure 1 shows the typical results of CCR experiments for Ni(10)/Al_2O_3, Ni(10)-Ca(28)/Al_2O_3, and Ni(10)/CaO. Table 1 summarizes the CCR performance of the various DFMs. Ni(10)-Ca(28)/Al_2O_3 and Ni(10)/CaO captured CO_2 for longer periods than Ni(10)/Al_2O_3. The initial H_2O formation under CO+O_2 for Ni(10)-Ca(28)/Al_2O_3 and Ni(10)/CaO can be due to the desorption of adsorbed H_2O generated during H_2 pretreatment. Under a subsequent flow of H_2, CH_4 and H_2O were produced in the cases of Ni(10)-Ca(28)/Al_2O_3 and Ni(10)/CaO, respectively, whereas CH_4 formation was negligible in the case of Ni(10)/Al_2O_3. These results clearly demonstrate that Ca is indispensable for CO_2 capture and CH_4 formation in the CCR.

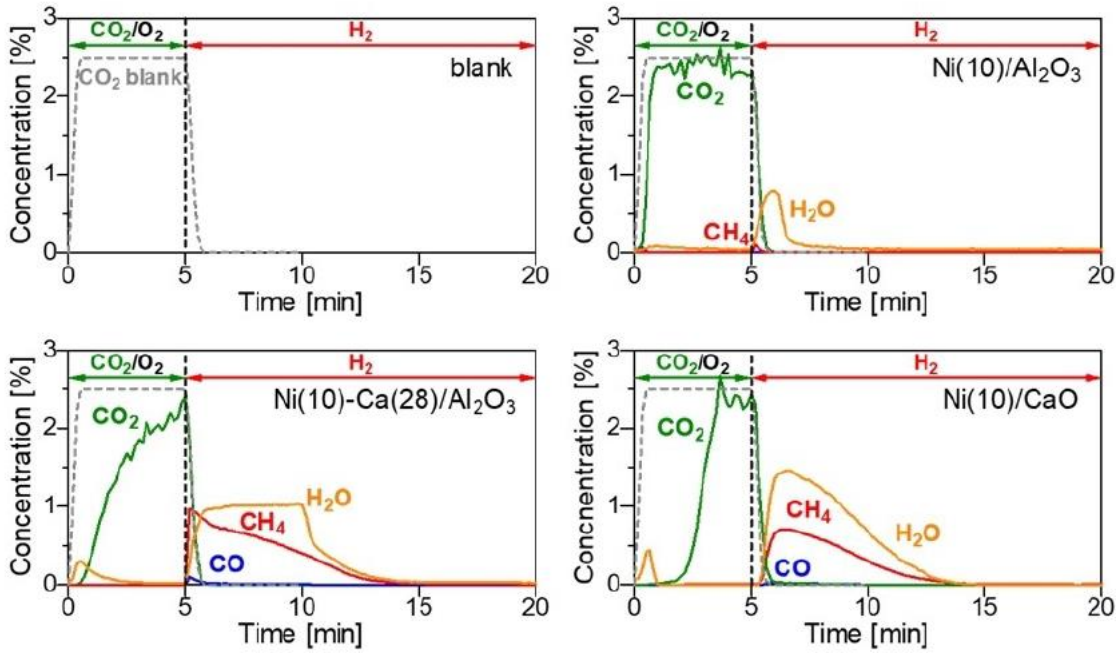

Figure 1. Effluent gas concentration profiles during CO_2 capture (2.5% CO_2+10% O_2/N_2) and reduction (pure H_2) over Ni(10)/Al_2O_3, Ni(10)-Ca(28)/Al_2O_3, and Ni(10)/CaO.

Table 1. Summary of CCR performances over Ni based DFMs.[a]

Catalyst	CO_2 ad. [μmol g^{-1}][b]	CH_4 [μmol/g][b]	Sel.$_{CH4}$ [%][c]	CH_4 yield [c] [%]
Ni(10)/Al_2O_3	123	8	86	9
Ni(10)/CaO	870	379	98	45
Ni(10)-Ca(28)/Al_2O_3	687	557	99	81
Ni(10)-Ca(8)/Al_2O_3	326	161	98	51
Ni(10)-Ca(14)/Al_2O_3	465	289	98	63

Ni(10)-Ca(32)/Al_2O_3	800	449	99	57
Ni(30)-Ca(28)/Al_2O_3	610	385	97	65
Ni(50)-Ca(28)/Al_2O_3	508	421	97	85

[a] Reaction conditions: 300 mg of DFMs, 500 ºC, 2.5% CO2+10% O2/N2 for 5 min, followed by pure H_2 for 15 min. [b] The composition of the outlet gas was quantitatively analyzed using FTIR spectroscopy combined with a gas cell. [c] Based on the amounts of CH_4 and CO produced during the reduction period. [d] Amounts of produced CH_4 per unit of adsorbed CO_2.

Next, we compared the CCR performance of the Ni(10)-Ca/Al_2O_3 samples containing different Ca loadings (0–64 wt%) at 500 ºC (Figure 2a). The Ca loading in Ni(10)/CaO was 64 wt%. The amount of adsorbed CO_2 increased monotonically increasing Ca loading up to 32 wt% and leveled off at higher Ca loadings. The amount of CH_4 formed under H_2 increased with Ca loading up to 32 wt% and then decreased with a further increase in Ca loading. The yield of CH_4 based on the amount of adsorbed CO2 also exhibited the same trend. Consequently, a Ca loading of 28 wt% was determined to be optimal for Ni(10)-Ca/Al_2O_3. We then compared the CCR performances of the Ni-Ca(28)/Al_2O_3 samples containing different Ni loadings (Figure 2b). When the amount of Ni loading was increased from 10 to 50 wt%, the amounts of CO2 adsorbed and CH4 formed decreased slightly from 687 to 508 mmol g^{-1} and 557 to 421 mmol g^{-1}, respectively. The yield of CH4 based on the amount of adsorbed CO2 varied within a narrow range of 85 to 65%, depending on the Ni loading. These results imply that the effect of Ni loading on CCR performance was not significant. Using the optimal DFM material, Ni(10)-Ca(28)/Al_2O_3, the CCR performance was evaluated at different temperatures (Figure2c). Increase in the temperature from 300 to 500 ºC resulted in monotonic increase in the CO_2 adsorption, CH_4 formation, and the CH_4 yield based on the amount of adsorbed CO_2 (37 to 81%). Under the best conditions at 500 ºC with the best DFM, Ni(10)-Ca(28)/Al_2O_3, the amount of CO_2 captured was 687 mmol g^{-1} and the CH_4 yield based on the adsorbed CO_2 was 81%. The captured CO_2 was selectively converted to CH_4, with 99% conversion to CH_4 and only 1% conversion to CO.

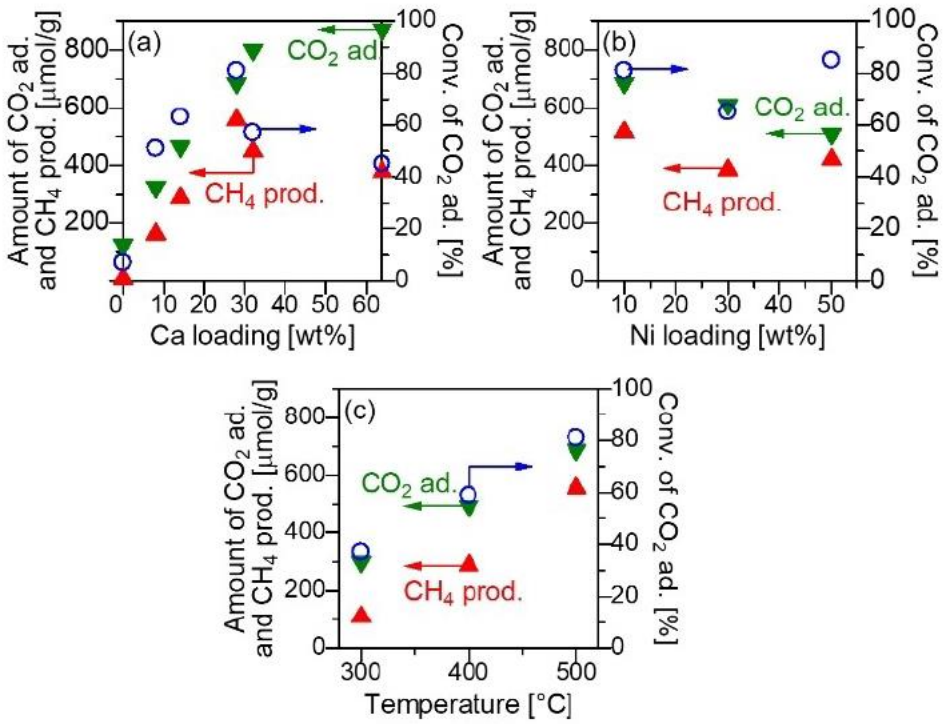

Figure 2. Variation in CO_2 adsorption (green), CH_4 formation (red), and CH_4 yields based on adsorbed CO_2 (blue) with respect to (a) Ca loading, (b) Ni loading, and (c) reaction temperature, over Ni-Ca/Al_2O_3 at 500 ºC (except for (c)).

3.3.2 Characterization of Ni(10)-Ca(28)/Al_2O_3

Detailed characterization experiments were conducted on the optimum DFM, Ni(10)-Ca(28)/Al_2O_3. Ni nanoparticles with an average diameter of 5.4 nm were observed using STEM and EDX (Figure 3). The EDX line scan profile shows a Ca-rich zone corresponding to aggregated Ca species in the particle of Ni(10)-Ca(28)/Al_2O_3.

Figure 4 shows XRD profiles of Ni(10)/CaO, Ni(10)-Ca(28)/Al_2O_3, Ni(10)/Al_2O_3, $CaCO_3$, and CaO. The XRD patterns of Ni(10)/CaO and Ni(10) Ca(28)/Al2O3 after H2 treatment exhibited peaks assignable to CaO (32.4º, 37.6º, and 54.1º).[40] No peak corresponding to CaCO3 (29.5º) was observed. Combined with the results of the EDX line scan, it was observed that CaO particles were the dominant Ca species on H_2-reduced Ni(10)-Ca(28)/Al_2O_3. The CaO crystallite sizes of Ni(10)-Ca(28)/Al_2O_3 and Ni(10)/CaO were evaluated using the full width at half maximum (FWHM) of the peak at 37.6º owing to CaO(111). The FWHM of the Ni(10)/CaO peak was narrower than that of the Ni(10)-Ca(28)/Al_2O_3. The CaO crystallite sizes (15.5 nm) for Ni(10)- Ca(28)/Al_2O_3, based on the Scherrer equation, were smaller than that for Ni(10)/CaO (31.7 nm).

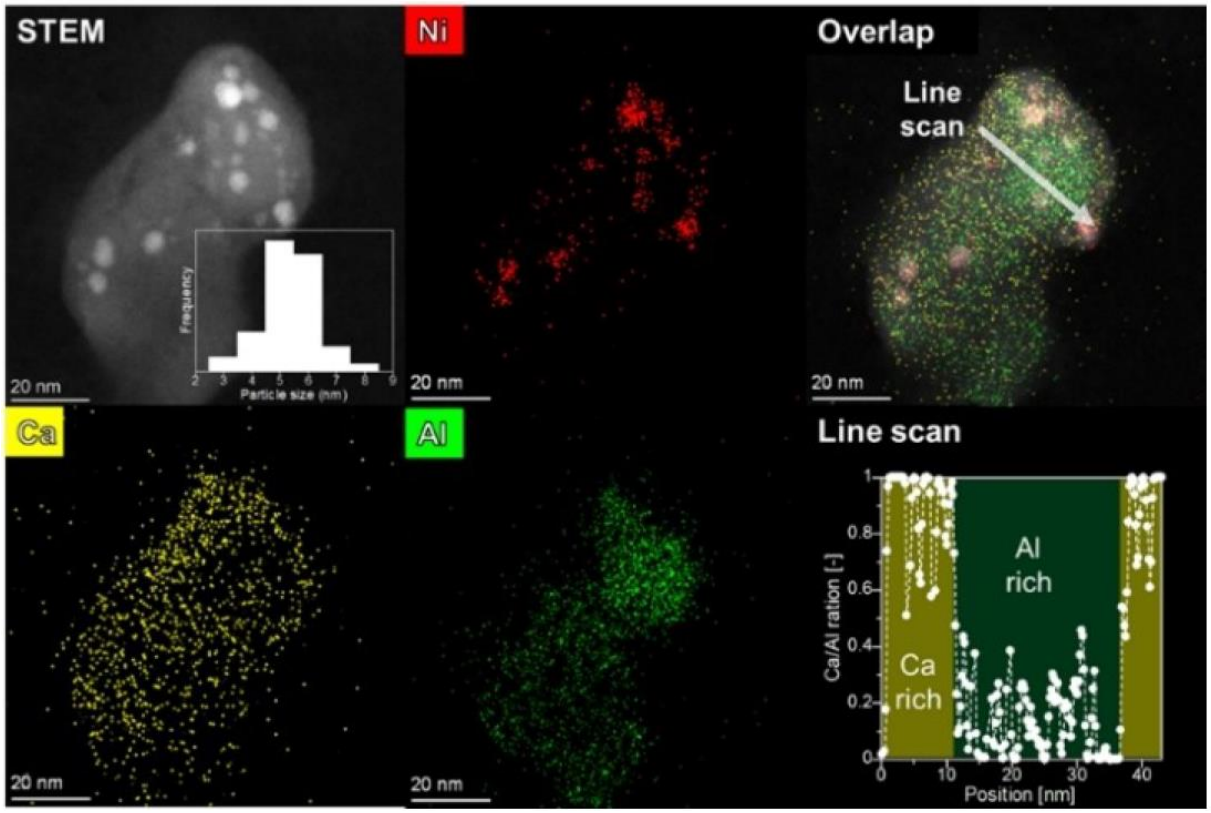

Figure 3. STEM and EDX mappings of Ni(10)-Ca(28)/Al_2O_3 after H_2 treatment for 30 min at 500 ºC.

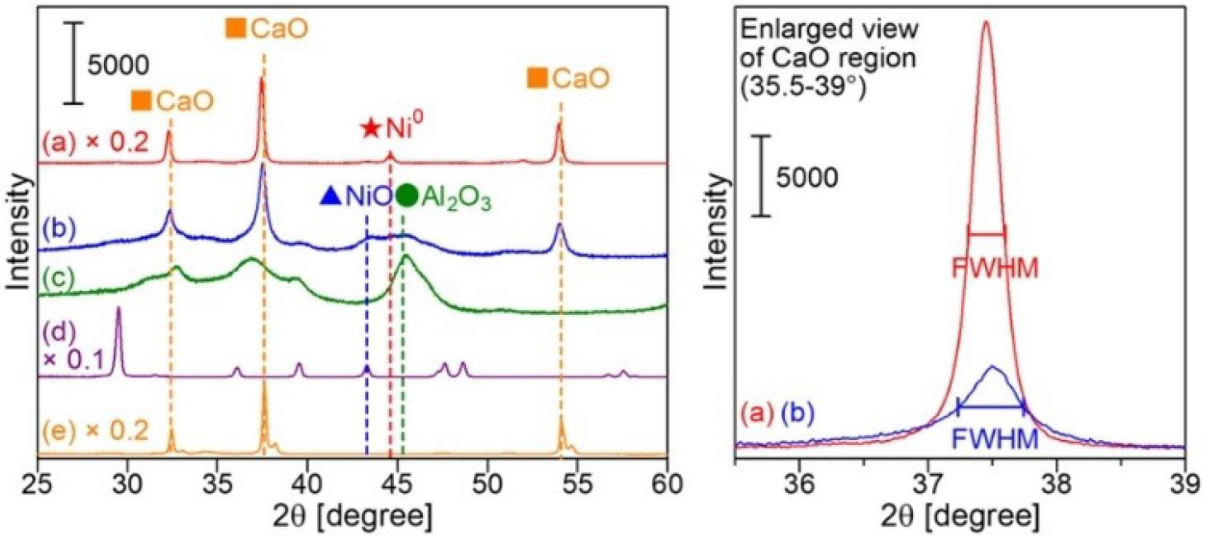

Figure 4. XRD patterns for (a) Ni(10)/CaO, (b) Ni(10)-Ca(28)/Al_2O_3, (c) Ni(10)/Al_2O_3, $CaCO_3$, and CaO. The Ni-loaded DFMs were pre-reduced by H_2 for 30 min at 500 ºC.

The oxidation states of the Ni species in the DFMs were investigated using Ni K-edge XANES (Figure 5a). The XANES spectrum of Ni(10)-Ca(28)/Al_2O_3 after the CO_2+O_2 treatment at 500 ºC was nearly identical to that of NiO (reference compound), indicating that the Ni species on this DFM were present as NiO. The XANES spectra of Ni(10)/CaO and Ni(10)/Al_2O_3 after the CO_2 +O_2 treatment (Figure. 6) were also identical to those of NiO, suggesting that NiO was the major Ni species in these samples. After the H_2-reduction, the intensities of the white line peak associated with NiO in these three samples fell within the range between those of Ni foil and NiO. This suggests the co-presence of Ni metal and NiO in the reduced samples. The white-line intensities changed in the following order: Ni(10)/Al_2O_3>Ni(10)- Ca(28)/Al_2O_3>Ni(10)/CaO. This suggests that the NiO/Ni ratio in the H_2-reduced DFMs changed in the same order.

Figure 5b shows the Fourier transforms of the Ni *K*-edge EXAFS for the DFMs after CO_2+O_2 and H_2 treatments. The R space plots are not phase-corrected, and thus, they do not represent the true bond distances. Table 2 lists the corresponding curve-fitting results. The peaks around 1.6 and 2.7 Å correspond to the Ni-O bond and the Ni-O-Ni bond of NiO, respectively. The peak around 2.2 Å corresponds to the Ni-Ni bond of Ni metal. All the spectra of CO_2+O_2-treated DFMs exhibited two characteristic peaks corresponding to NiO. On the other hand, the H_2-treated DFMs exhibited a peak at 2.2 Å corresponding to metallic Ni. The curve-fitting analysis (Table 2) revealed the coordination number (CN) and bond distance (*R*). The Ni(10)-Ca(28)/Al_2O_3 sample, subjected to H_2 treatment, exhibited reduced CNs for the Ni-O and Ni-O-Ni bonds compared to the sample treated with CO_2/O_2. Additionally, it

exhibited the presence of metallic Ni-Ni bonds, with a coordination number of 4.5 at a distance of 2.50 Å. The H_2-treated Ni(10)/CaO exhibited only a metallic Ni-Ni bond (CN of 8.0 at 2.47 Å). Among the H_2-treated samples, the CN of the Ni-O shell bond increased in the following order: Ni(10)/CaO (0)<Ni(10)-Ca(28)/Al_2O_3 (1.0)<Ni(10)/Al_2O_3 (4.6), suggesting that the relative amount of NiO after the H_2 treatment increases in the same order. This trend is consistent with the XANES results and implies that the reducibility of NiO increases with increasing Ca loading.

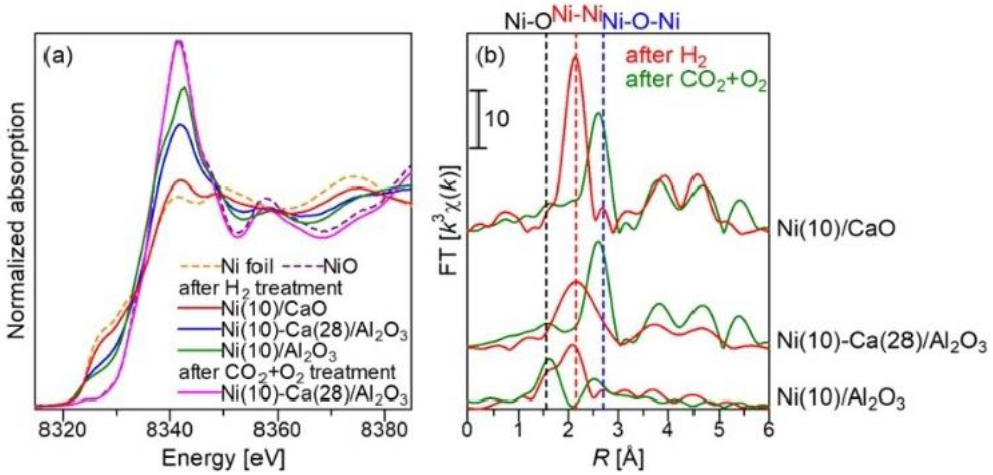

Figure 5. Ni K-edge (a) XANES and (b) EXAFS FTs of Ni(10)/Al_2O_3, Ni(10)-Ca(28)/Al_2O_3, and Ni(10)/CaO after H_2 reduction (30 min) and 2.5% CO_2/10% O_2/He treatment (5 min) at 500 ºC. The spectra of the pretreated samples were obtained at room temperature without exposure to air.

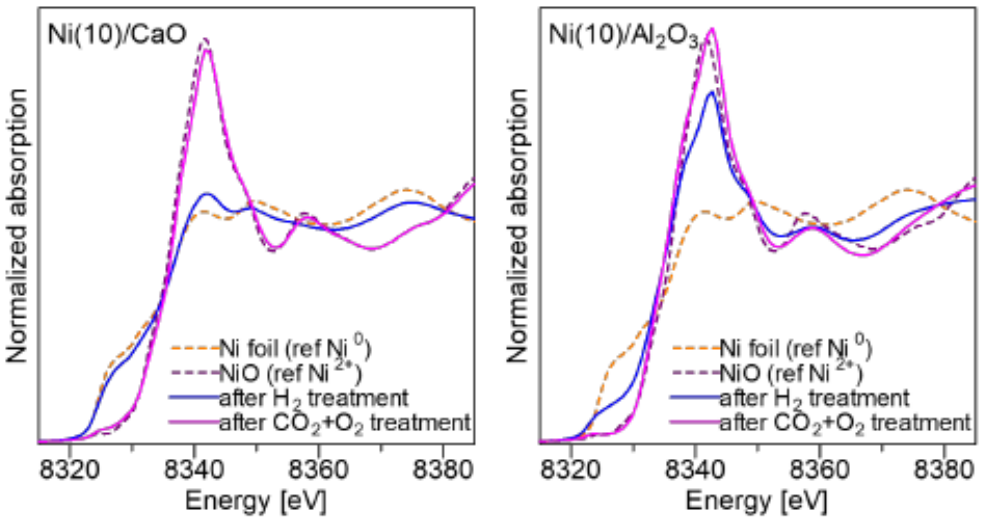

Figure 6. Ni K-edge XANES of Ni(10)/Al_2O_3 and Ni(10)/CaO after H_2-reduction (30 min) and after 2.5% CO_2/10% O_2/He treatment (5 min) at 500 ºC. The spectra of the pretreated samples were obtained at room temperature without exposure to air.

Table 2. Curve-fitting analysis of Ni K-edge EXAFS of Ni DFMs.

Sample	Pretreatment	Shell	CN[a]	R [Å][b]	σ [Å][c]	Rf [%][d]
Ni(10)/CaO	H_2	Ni-Ni	8.0	2.47	0.067	0.7
	CO_2+O_2	Ni-O	7.5	2.13	0.089	0.5
		Ni-O-Ni	10.5	2.94	0.074	
Ni(10)-Ca(28)/Al_2O_3	H_2	Ni-O	1.0	2.10	0.060	4.7
		Ni-Ni	4.5	2.50	0.075	
		Ni-O	3.1	2.95	0.090	
	CO_2+O_2	Ni-O	8.0	2.10	0.106	0.5
		Ni-O-Ni	9.9	2.94	0.074	
Ni(10)/Al_2O_3	H_2	Ni-O	4.6	2.00	0.095	0.01
		Ni-Ni	4.8	2.46	0.088	
	CO_2+O_2	Ni-O	7.3	2.04	0.093	0.5
		Ni-O-Ni	5.7	2.95	0.108	
NiO[e]		Ni-O	6	2.02		
		Ni-O-Ni	12	2.94		
Ni foil[e]		Ni-Ni	12	2.49		

[a] Coordination numbers. [b] Bond distance. [c] Debye-Waller factor. [d] Residual factor. [e] Crystallographic data of Ni oxide and Ni metal.

3.3.3 Redox of Ni species during CCR over Ni(10)-Ca(28)/Al_2O_3

The catalytic test of Ni(10)-Ca(28)/Al_2O_3 for the unsteady-state methanation under periodic 2.5% CO_2⇔H_2 feeds was conducted at 500 ºC on a fixed-bed flow reactor. Figure 7 shows the time course of the concentration profiles of the outlet gases (CO_2, H_2, CH_4, CO, and H_2O). Unlike the conditions shown in Figure 1, the periodic reaction test shown in Figure 7 was conducted without O_2 during the CO_2 capture phase to discuss the CCR mechanism, excluding Ni oxidation by O_2. After pretreatment under H_2, the exposure of Ni(10)-Ca(28)/Al_2O_3 to CO_2 resulted in CO_2 capture. The H_2O peak can be due to desorption of adsorbed H_2O generated during the H_2 pretreatment. Subsequent exposure to H_2 resulted in the formation of CH_4, followed by H_2O formation. The CO formation was negligibly small. The delayed H_2O formation could be due to larger interaction of H_2O with the polar catalyst surface than non-polar CH_4.

The amount of CH_4 formed was 520 mmol g^{-1}, and the selectivity of CH_4 was 95%. These values were similar to those under O_2-cofeeding conditions (Table 1).

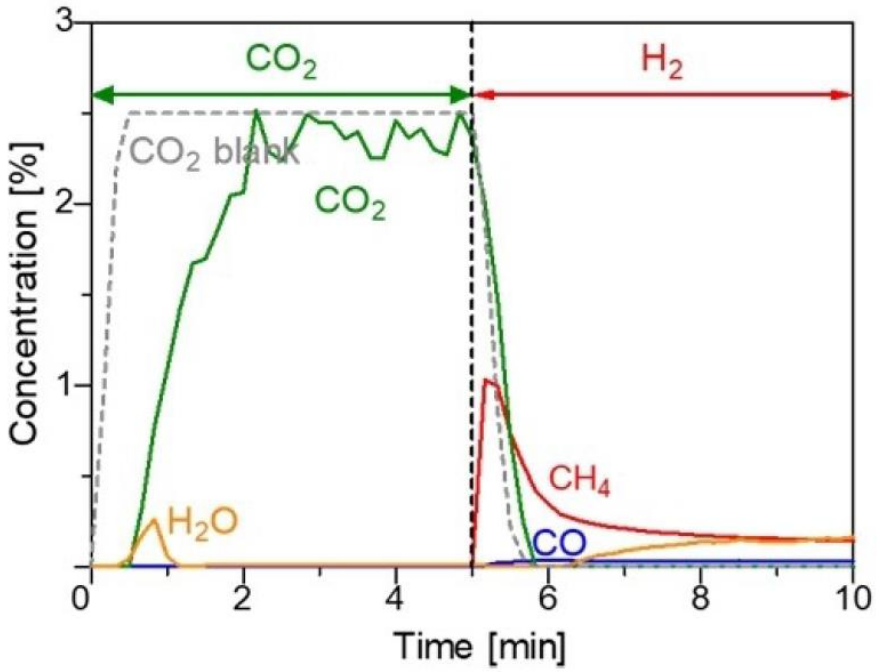

Figure 7. Effluent gas concentration profiles during CO2 capture (2.5% CO_2, 5 min) and subsequent H_2-reduction (pure H_2, 15 min) at 500 ºC.

To understand the oxidation state of the Ni nanoparticles during CO2 flow, *in situ* Ni K-edge XANES measurements were performed for H_2-prereduced Ni(10)- Ca(28)/Al_2O_3 (Figure 8). During the CO_2 flow, the white-line intensity increased slightly (Figure 8a). The time course of the white-line intensity at 8341.5 eV (Figure 8b) exhibited a slight oxidation of metallic Ni by CO_2 within the first 2 min.

XPS experiments (Figure 9) were also performed to identify the oxidation states of the Ni nanoparticle surfaces. After H_2 and subsequent CO_2 treatments at 500 ºC, Ni(10)-Ca(28)/Al_2O_3 was transferred to an XPS chamber without exposure to air. The XPS spectrum after CO_2+O_2 treatment of the Ni 2*p* region exhibited 2$p_{1/2}$ (855.9 eV) and 2$p_{3/2}$ (873.5 eV) peaks corresponding to Ni^{2+}.[41–43] The broad peaks at around 863 and 881 eV are the satellite peaks of the Ni (Ni^0 and Ni^{2+}) species. After the H_2 treatment, two additional peaks assignable to Ni^0 (869.8 eV for 2$p_{1/2}$ and 853.4 eV for 2$p_{3/2}$) were observed.[43] These peaks are clearly separated, implying the absence of an intermediate oxidation state between Ni^0 and Ni^{2+}. Ni^0 and Ni^{2+} peaks were also observed for CO_2-treated Ni(10)-Ca(28)/Al_2O_3, but the CO_2-treated sample showed a higher intensity of the Ni^{2+} peak (855.9 eV) than the H_2-treated sample. Based on the curve-fitting analysis, the fractions of Ni^{2+} and Ni^0 species were also estimated (Table 3). The fraction of Ni^{2+} for the CO_2-treated sample (55.7%) was higher than that in the H_2-treated sample (50.9 %). *In situ* Ni K-edge XANES and XPS results indicate the partial oxidation of the surface Ni^0 species by CO_2. The redox phenomena could play a role in the unsteady-state methanation of Ni(10)-Ca(28)/Al_2O_3.

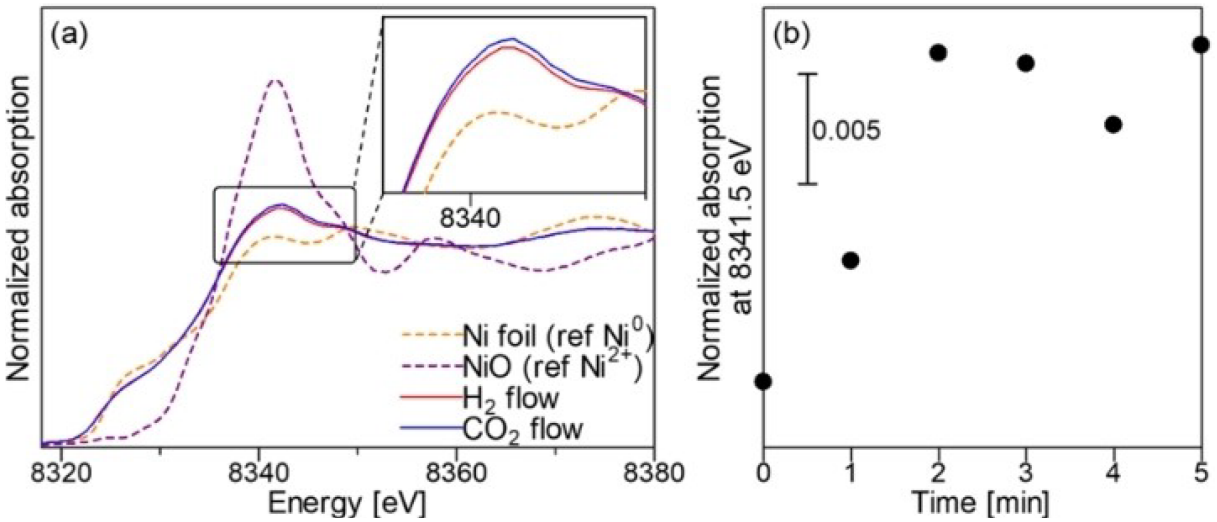

Figure 8. (a) *In situ* Ni-K edge XANES spectra of H2-prereduced Ni(10)-Ca(28)/Al2O3 during CO2 capture under O2-free conditions (2.5% CO2, 5 min, green line) and CO2 capture with O2 co-feed (2.5% CO2/10% O2, 5 min, red line) at 500 ºC. (b) Kinetics of oxidation of Ni0 on Ni(10)-Ca(28)/Al2O3 during CO2 capture without O2 co-feed.

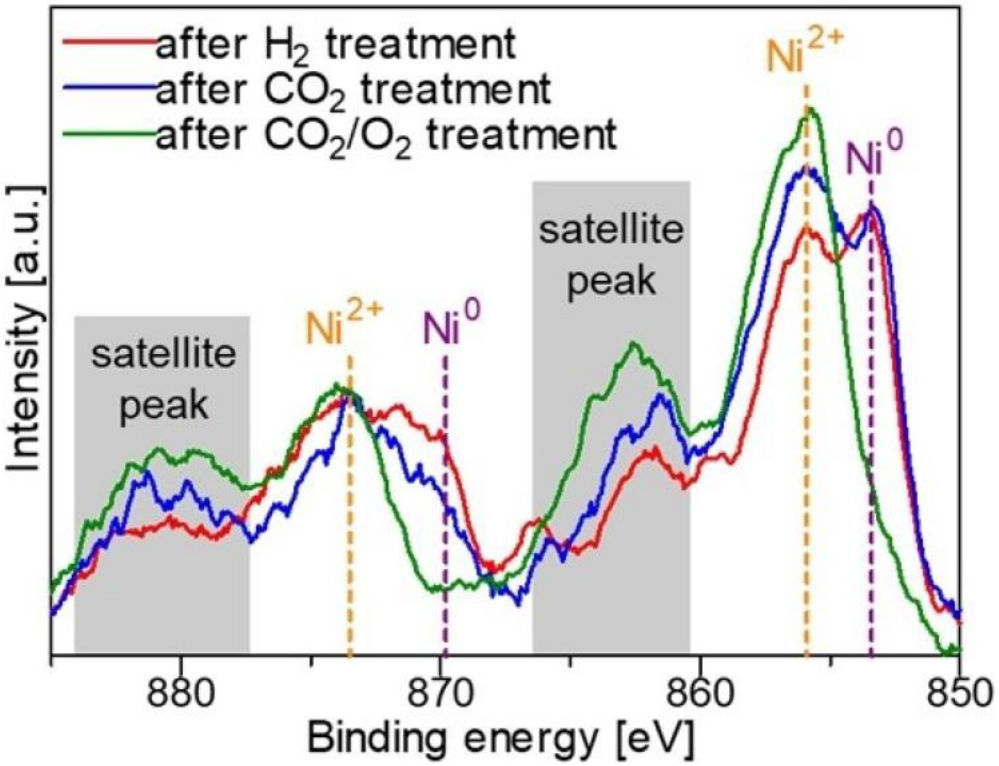

Figure 9. Ni 2p XPS spectra of Ni(10)-Ca(28)/Al_2O_3 after H_2, CO_2, and CO_2+O_2 treatments. Reaction temperature was 500 ºC. H_2- and CO_2- treated samples were prepared without exposure to air.

Table 3. Ni $2p_{3/2}$ XPS analysis of Ni(10)-Ca(28)/Al_2O_3.

Treatment gas	Fraction of Ni species [%][a]		Ni^0/Ni^{2+} [-][a]
	Ni^{2+}	Ni^0	
H_2	50.9	49.1	0.96
CO_2	55.7	44.3	0.80
CO_2+O_2	100	0	0.00

[a] Calculated from the area of the Ni $2p_{3/2}$ peak after curve-fitting analysis.

3.3.4 Formation and decomposition of CaCO3 during CCR (*in situ* XRD)

To characterize the dynamic changes in the structure of the Ca species on Ni(10)-Ca(28)/Al_2O_3 during CCR, *in situ* XRD measurements were performed (Figure 10). Prior to the experiment, the sample was reduced by 5% H_2/N_2 at 500 ºC. Subsequently, the formation and consumption of $CaCO_3$ were monitored by *in situ* XRD under successive feeds of 10% CO_2/N_2 and 5% H_2/N_2 at 500 ºC. For Ni(10)-Ca(28)/Al_2O_3, two peaks assignable to CaO were observed after the H_2 pretreatment. Upon changing the gas flow to CO_2/He, the intensities of these two XRD signals gradually decreased, and three peaks assignable to $CaCO_3$ were observed. These results provide direct evidence of the reaction between CaO and CO_2 to yield bulk $CaCO_3$ during the CO_2 storage step of the CCR operation. The peak corresponding to NiO at 44º also appeared under CO_2. This result is consistent with the XPS (Figure 9) and *in situ* XANES (Figure 8) results, which show that part of the Ni^0 species was oxidized by CO_2 to yield NiO. When the gas was switched to 5% H_2/N_2, the intensities of the $CaCO_3$ peaks decreased, and those of the CaO peaks increased again. These results provide direct evidence for the reduction of bulk $CaCO_3$ with H_2 to yield CaO during the H_2 reduction step of the CCR operation. Combined with the product gas profile in Figure 7, it can be concluded that the H_2-reduction of bulk $CaCO_3$ yields CaO and gas-phase products (CH_4 and H_2O). As shown in Figure 11, bulk $CaCO_3$ formation under CO_2 and consumption under H_2 were also observed for Ni(10)/CaO. The observed similarity between Ni(10)-Ca(28)/Al_2O_3 and Ni(10)/CaO suggests that CCR with Ni-Ca based DFMs proceeds via a similar mechanism involving the formation and reduction of bulk carbonates. In our previous study using *in situ* FTIR also provided direct evidence of the formation and decomposition of surface carbonates on Ni-Ca based DFMs during CCR.[39]

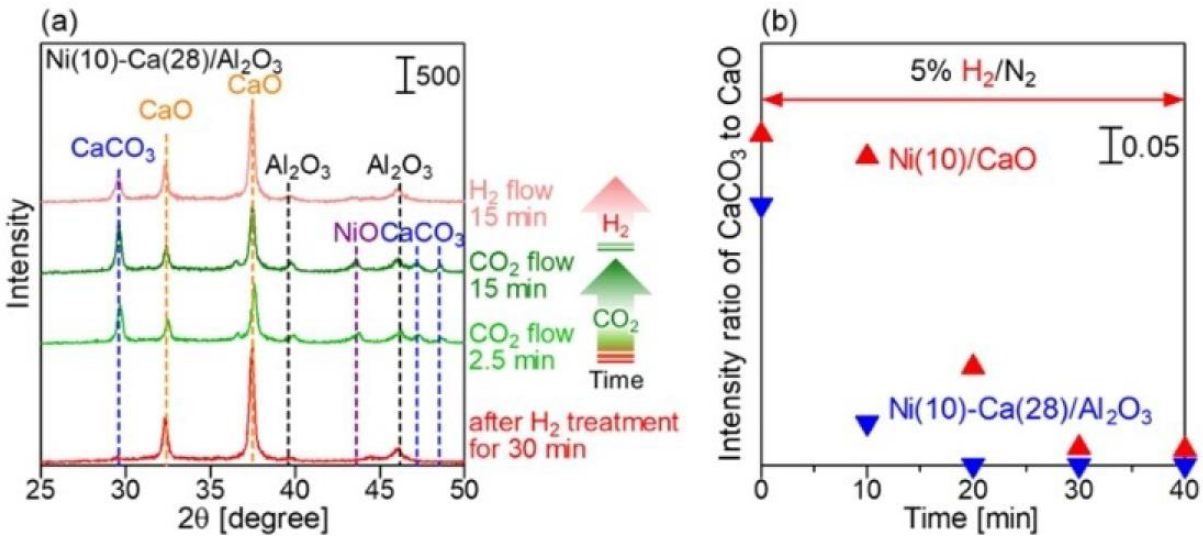

Figure 10. (a) *In situ* XRD patterns of the H_2-prereduced Ni(10)-Ca(28)/Al2O3 at 500 ºC. The flow gas was successively changed from 10% CO_2/He (for 15 min) to 5% H_2/N_2 (for 15 min). (b) XRD intensity ratio of $CaCO_3$ to CaO for Ni(10)-Ca(28)/Al_2O_3 and Ni(10)/CaO versus reduction time.

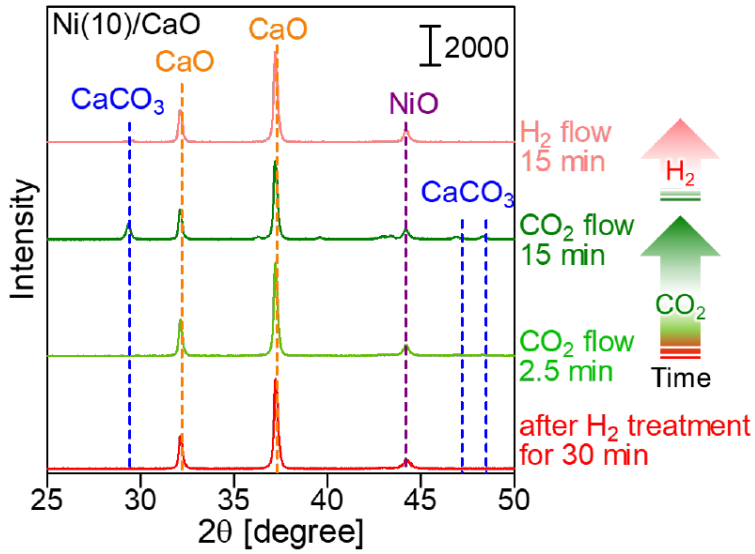

Figure 10. *In situ* XRD patterns of H_2-prereduced Ni(10)/CaO. The flow gas was successively changed from 10% CO_2/He (15 min) to 5% H_2/N_2 (5 min).

As shown in Figure 2, the CaO crystallite size of Ni(10)-Ca(28)/Al_2O_3 (15.5 nm) is smaller than that of Ni(10)/CaO (31.7 nm). To discuss the effect of the CaO particle size on the hydrogenation kinetics, the XRD intensity ratios of $CaCO_3$ to CaO on Ni(10)-Ca(28)/Al_2O_3 and Ni(10)/CaO are plotted against the H_2-reduction time in Figure 10b. The results show that the consumption of $CaCO_3$ was faster over Ni(10)- Ca(28)/Al_2O_3 than over Ni(10)/CaO. This suggests that $CaCO_3$ species on smaller CaO particles are more reactive during the methanation process.

Based on the XPS, *in situ* XANES, and *in situ* XRD results, a simple redox mechanism for the CCR reaction over Ni-Ca based DFMs is proposed in Figure 12. In the CO_2 storage

step, part of the bulk CaO, probably the surface layers of the CaO particles, reacts with CO_2 to yield bulk $CaCO_3$. In the subsequent H_2-reduction step, the bulk $CaCO_3$ is reduced by H_2 to yield CaO and gas-phase products (CH_4 and H_2O). Assuming that the Ni site is a H_2 dissociation site, it can be proposed that the carbonate species at the Ni-Ca interface site is responsible for CH_4 production. Furthermore, after consuming the carbonate species at the Ni-Ca interface, other carbonate species could diffuse to the Ni site and be reduced to give CH_4 and H_2O. The carbonate diffusions at similar temperature conditions were previously reported by Muller et al.[45]

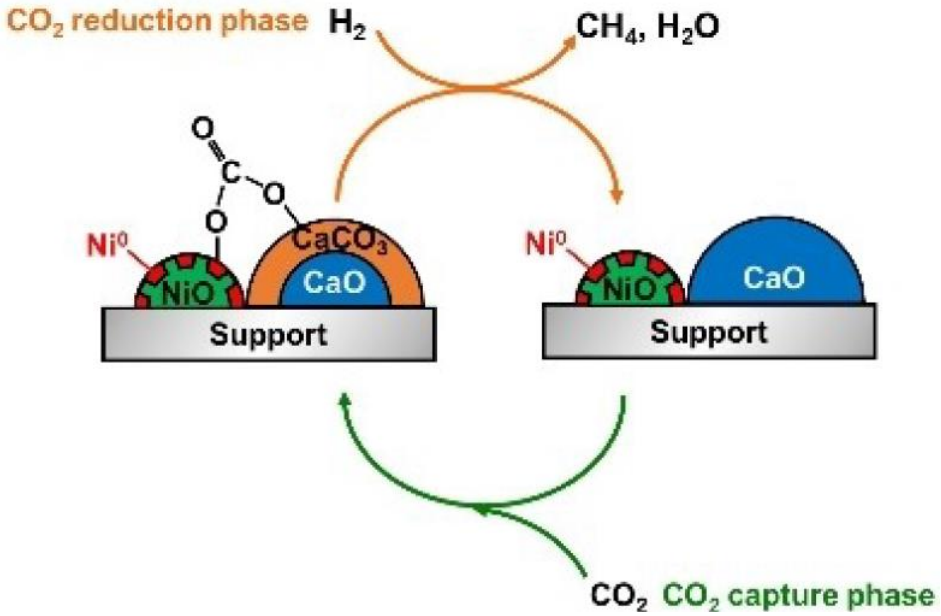

Figure 12. (a) *In situ* XRD patterns of the H_2-prereduced Ni(10)-Ca(28)/Al2O3 at 500 ºC. The flow gas was successively changed from 10% CO_2/He (for 15 min) to 5% H_2/N_2 (for 15 min). (b) XRD intensity ratio of $CaCO_3$ to CaO for Ni(10)-Ca(28)/Al_2O_3 and Ni(10)/CaO versus reduction time.

3.3.4 *Operando* XANES study during CCR with O_2

The mechanism of unsteady-state methanation without O_2 was discussed above. In a practical CCR process, CO_2 is captured in the presence of O_2; therefore, the effects of O_2 should be studied in detail. *Operando* XANES measurements at 500 ºC with online gas analysis were performed using Ni(10)-Ca(28)/Al_2O_3 to investigate the oxidation state of Ni species during CCR in the presence of O_2 (Figure 13). Figure 13 shows the time dependence of the generated gas and Ni^0. The fraction was determined by LCF analysis of XANES spectra using NiO and Ni foil as Ni^{2+} and Ni^0 references, respectively. After the initial H_2 treatment, 80% of the Ni species on Ni(10)- Ca(28)/Al_2O_3 was metallic Ni^0. Then, the Ni^0 species underwent rapid oxidation (within 1 min) under 2.5% CO_2/10% O_2/He, 93% of the Ni species was converted to NiO after 6 min, and gas phase H_2O was simultaneously observed. In addition to these results (Figure 8), it was observed that Ni^0 was only slightly oxidized by CO_2,

indicating that the metallic Ni^0 species were rapidly and completely oxidized by O_2 to yield NiO and H_2O. When the gas flow was changed to H_2, the Ni^0 fraction rapidly increased within 1 min. Also, the highest H_2O formation rate was observed at 1 min. The results suggest that surface NiO species are reduced by H_2 to yield surface Ni^0 sites and H_2O. Afterward, the surface Ni0 sites continuously catalyze the H_2-reduction of adsorbed CO_2 to give CH_4 and H_2O. Gradual increase in the Ni^0 fraction after 1 min suggests gradual increase in the Ni^0 species most probably inside the Ni particles.

The CCR mechanism of the Ni-Ca based DFMs in the presence of O_2 is illustrated in Figure 14. In the initial CO_2 capture step, the Ni^0 species undergoes complete oxidation by O_2 to yield NiO, followed by CO_2 capture via the interaction between the CaO surface and CO_2 to yield $CaCO_3$ layers on the CaO particles. When the gas flow was switched to H_2, NiO was partially reduced by H_2 to provide Ni^0 sites, which acted as active sites for the H_2-reduction of adjacent $CaCO_3$ layers to yield CaO and gas-phase products, CH_4 and H_2O.

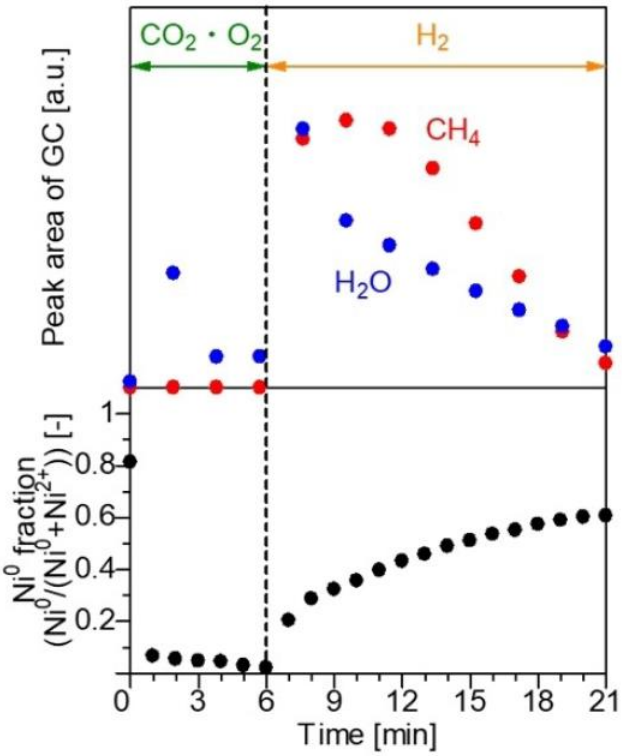

Figure 13. *Operando* Ni K-edge XANES results for Ni(10)-Ca(28)/Al_2O_3 at 500 ºC during CO_2 capture (under 2.5% CO_2+10% O_2, for 5 min), followed by H_2-reduction (10% H_2, for 15 min). GC signals for CH_4 and H_2O and Ni^0 fraction determined by LCF analysis of the *in situ* Ni K-edge XANES results are plotted against time.

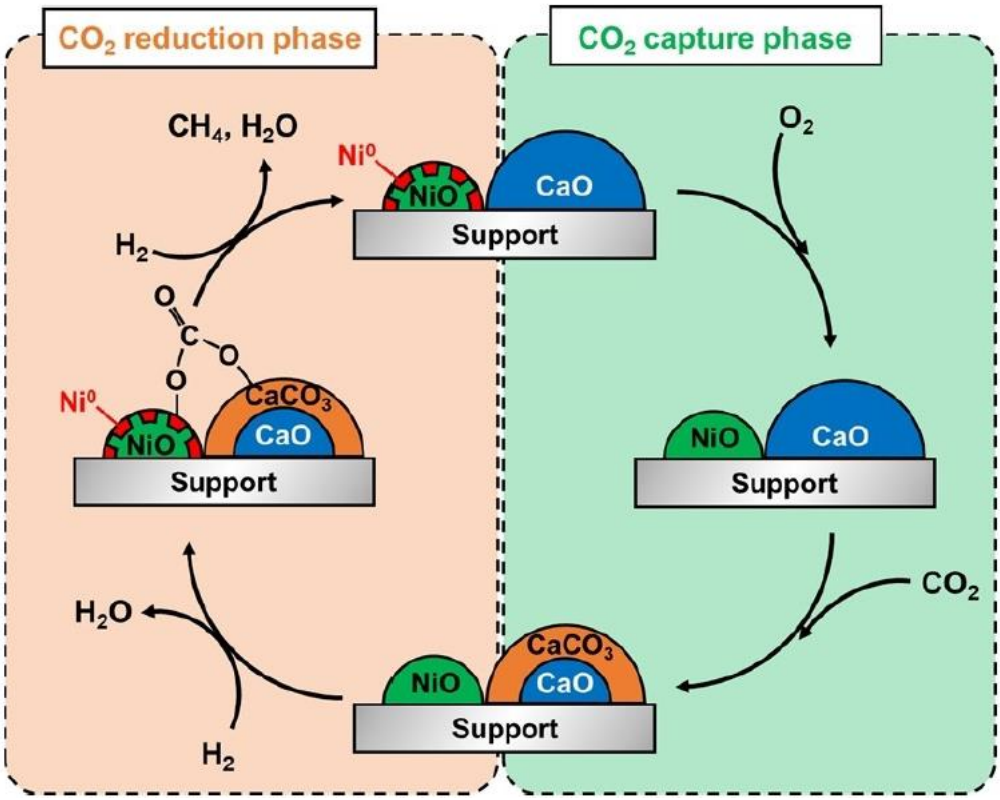

Figure 14. A proposed mechanism for CCR (with O2 during the CO2 capture step) over Ni-Ca based DFMs.

3.4 Conclusion

We performed various *in situ* and *operando* spectroscopic studies, and the following conclusions were obtained regarding the mechanism of the CCR of CH_4 over Ni-Ca based DFMs. Under O_2-free conditions, only a small part of the Ni^0 species was oxidized by CO_2 during the CO_2 storage step, whereas a part of the bulk CaO reacted with CO_2 to yield bulk $CaCO_3$ layers on CaO. In the subsequent H_2-reduction step, the bulk $CaCO_3$ was reduced by H_2 to yield CaO and gas-phase products (CH_4 and H_2O). In the presence of O_2 during the CO_2 capture step, the Ni^0 species underwent complete oxidation by O_2 to yield NiO, followed by CO_2 capture via the interaction between the CaO surface and CO_2 to yield $CaCO_3$ layers on the CaO particles. When the gas flow was switched to H_2, NiO was partially reduced by H_2 to provide Ni^0 sites, which served as active sites for the H_2-reduction of adjacent $CaCO_3$ layers to yield CaO and gas-phase products, CH_4 and H_2O.

3.5 References

(1) D. A. Lashof, D. R. Ahujah, *Nature* 1990, *344*, 529‐531.

(2) S. Fawzy, A. I. Osman, J. Doran, D. W. Rooney, *Environ. Chem. Lett.* 2020, *18*, 2069‐2094.

(3) C. Gough, *Int. J. Greenhouse Gas Control* 2008, *2*, 155‐168.

(4) M. Bui, C. S. Adjiman, A. Bardow, E. J. Anthony, A. Boston, S. Brown, P. S. Fennell, S. Fuss, A. Galindo, L. A. Hackett, J. P. Hallett, H. J. Herzog, G. Jackson, J. Kemper, S. Krevor, G. C. Maitland, M. Matuszewski, I. S. Metcalfe, C. Petit, G. Puxty, J. Reimer, D. M. Reiner, E. S. Rubin, S. A. Scott, N. Shah, B. Smit, J. P. M. Trusler, P. Webley, J. Wilcox, N. Mac Dowell, *Energy Environ. Sci.* 2018, *11*, 1062‐1176.

(5) M. Tamura, M. Honda, Y. Nakagawa, K. Tomishige, *J. Chem. Technol. Biotechnol.* 2014, *89*, 19‐33.

(6) J. Rogelj, M. Den Elzen, N. Hohne, T. Fransen, H. Fekete, H. Winkler, R. Schaeffer, F. Sha, K. Riahi, M. Meinshausen, *Nature* 2016, *534*, 631‐639.

(7) C. F. Schleussner, J. Rogelj, M. Schaeffer, T. Lissner, R. Licker, E. M. Fischer, R. Knutti, A. Levermann, K. Frieler, W. Hare, *Nat. Clim. Change* 2016, *6*, 827‐835.

(8) E. S. Sanz-Perez, C. R. Murdock, S. A. Didas, C. W. Jones, *Chem. Rev.* 2016, *116*, 11840‐11876.

(9) J. Rogelj, D. Huppmann, V. Krey, K. Riahi, L. Clarke, M. Gidden, Z. Nicholls, M. Meinshausen, *Nature* 2019, *573*, 357‐363.

(10) K. M. K. Yu, I. Curcic, J. Gabriel, S. C. E. Tsang, *ChemSusChem* 2008, *1*, 893‐899.

(11) N. Mac Dowell, P. S. Fennell, N. Shah, G. C. Maitland, *Nat. Clim. Change* 2017, *7*, 243‐249.

(12) M. T. Dunstan, F. Donat, A. H. Bork, C. P. Grey, C. R. Muller, *Chem. Rev.* 2021, *121*, 12681‐12745.

(13) A. Alvarez, A. Bansode, A. Urakawa, A. V. Bavykina, T. A. Wezendonk, M. Makkee, J. Gascon, F. Kapteijn, *Chem. Rev.* 2017, *117*, 9804‐9838.

(14) S. Sun, H. Sun, P. T. Williams, C. Wu, *Sustain. Energy Fuels* 2021, *5*, 4546‐4559.

(15) W. Gao, S. Liang, R. Wang, Q. Jiang, Y. Zhang, Q. Zheng, B. Xie, C. Y. Toe, X. Zhu, J. Wang, L. Huang, Y. Gao, Z. Wang, C. Jo, Q. Wang, L. Wang, Y. Liu, B. Louis, J. Scott, A. C. Roger, R. Amal, H. He, S. E. Park, *Chem. Soc. Rev.* 2020, *49*, 8584‐8686.

(16) T. P. Senftle, E. A. Carter, *Acc. Chem. Res.* 2017, *50*, 472‐475.

(17) E. I. Koytsoumpa, C. Bergins, E. Kakaras, *J. Supercrit. Fluids* 2018, *132*, 3‐16.

(18) S. Kar, A. Goeppert, G. K. S. Prakash, *Acc. Chem. Res.* 2019, *52*, 2892‐2903.

(19) S. Miyazaki, Z. Li, Z. Maeno, T. Toyao, M. Ito, Y. Nakajima, K. Shimizu *Chem. Lett.* 2022, *51*, 914‐918.

(20) S. Miyazaki, Z. Li, L. Li, T. Toyao, Y. Nakasaka, Y. Nakajima, K. Shimizu, Z. Maeno *Energy Fuels* 2023, *37*, 7945‐7957.

(21) S. Miyazaki, M. Yoshihara, T. Toyao, Z. Maeno, K. Shimizu *Next Nanotechnology* 2023, *3‐4*, 100029.

(22) L. Li, S. Miyazaki, S. Yasumura, K. W. Ting, T. Toyao, Z. Maeno, K. Shimizu, *ACS Catal.* 2022, *12*,

2639-2650.

(23) S. M. Kim, P. M. Abdala, M. Broda, D. Hosseini, C. Coperet, C. Muller, *ACS Catal.* 2018, *8*, 2815-2823.

(24) T. Hyakutake, W. Van Beek, A. Urakawa, *J. Mater. Chem. A* 2016, *4*, 6878-6885.

(25) M. S. Duyar, M. A. A. Trevino, R. J. Farrauto, *Appl. Catal. B* 2015, *168-169*, 370-376.

(26) M. S. Duyar, S. Wang, M. A. Arellano-Trevino, R. J. Farrauto, *J. CO2 Util.* 2016, *15*, 65-71.

(27) F. Kosaka, Y. Liu, S. Y. Chen, T. Mochizuki, H. Takagi, A. Urakawa, K. Kuramoto, *ACS Sustainable Chem. Eng.* 2021, *9*, 3452-3463.

(28) L. C. Wirner, F. Kosaka, T. Sasayama, Y. Liu, A. Urakawa, K. Kuramoto, *Chem. Eng. J.* 2023, *470*.

(29) F. Kosaka, T. Sasayama, Y. Liu, S. Y. Chen, T. Mochizuki, K. Matsuoka, A. Urakawa, K. Kuramoto, *Chem. Eng. J.* 2022, *450*, 138055.

(30) L. Proano, E. Tello, M. A. Arellano-Trevino, S. Wang, R. J. Farrauto, M. Cobo, *Appl. Surf. Sci.* 2019, *479*, 25-30.

(31) M. A. Arellano-Trevino, N. Kanani, C. W. Jeong-Potter, R. J. Farrauto, *Chem. Eng. J.* 2019, *375*, 121953.

(32) S. Wang, R. J. Farrauto, S. Karp, J. H. Jeon, E. T. Schrunk, *J. CO2 Util.* 2018, *27*, 390-397.

(33) W. Yang, Y. Feng, W. Chu, *Int. J. Chem. Eng.* 2016, 2041821.

(34) Z. Alipour, M. Rezaei, F. Meshkani, *J. Ind. Eng. Chem.* 2014, *20*, 2858-2863.

(35) A. Bermejo-Lopez, B. Pereda-Ayo, J. A. Gonzalez-Marcos, J. R. Gonzalez-Velasco, *J. CO2 Util.* 2019, *34*, 576-587.

(36) A. Bermejo-Lopez, B. Pereda-Ayo, J. A. Gonzalez-Marcos, J. R. Gonzalez- Velasco, *Sustain. Energy Fuels* 2021, *5*, 1194-1210.

(37) H. Sun, Y. Wang, S. Xu, A. I. Osman, G. Stenning, J. Han, S. Sun, D. Rooney, P. T. Williams, F. Wang, C. Wu, *Fuel* 2021, *286*, 119308.

(38) L. Li, Z. Wu, S. Miyazaki, T. Toyao, Z. Maeno, K. Shimizu, *RSC Adv.* 2023, *13*, 2213-2219.

(39) L. Li, S. Miyazaki, Z. Wu, T. Toyao, R. Selyanchyn, Z. Maeno, S. Fujikawa, K. Shimizu, *Appl. Catal. B* 2023, *339*, 123151.

(40) B. Ravel, M. Newville, *J. Synchrotron Radiat.* 2005, pp. 537-541.

(41) Y. Xu, F. Donat, C. Luo, J. Chen, A. Kierzkowska, M. Awais Naeem, L. Zhang, C. R. Muller, *Chem. Eng. J.* 2023, *453*, 139913.

(42) S. Tada, H. Nagase, N. Fujiwara, R. Kikuchi, *Energy Fuels.* 2021, *35*, 5241-5251.

(43) A. M. Hengne, A. K. Samal, L. R. Enakonda, M. Harb, L. E. Gevers, D. H. Anjum, M. N. Hedhili, Y. Saih, K. W. Huang, J. M. Basset, *ACS Omega* 2018, *3*, 3688-3701.

(44) J. Li, L. Shi, G. Feng, Z. Shi, C. Sun, D. Kong, *Catalysts* 2020, *10*, 1-14.

(45) S. M. Kim, P. M. Abdala, M. Broda, D. Hosseini, C. Coperet, C. Muller, *ACS Catal.* 2018, *8*, 2815-2823.

Chapter 4

Unsteady-state tandem catalytic systems for CO_2 capture and reduction.

4.1 Introduction

Anthropogenic greenhouse gas emissions are critical in causing global warming[1,2]. To mitigate global warming and achieve a carbon-neutral society, the amount of CO_2 emitting from energy- and industry-related sources must be significantly reduced[3,4]. One of the most promising strategies for mitigating anthropogenic CO_2 emissions is to convert CO_2 into chemical fuels, such as methane or methanol, and value-added chemicals via syngas[5,6]. However, CO_2 needs to be captured from emission sources (such as power, refinery, chemical, steel, and ceramic plants) and stored prior to chemical transformation[7]. Although liquid amine scrubbing is a commonly employed CO_2 capture and storage (CCS) technology in the industry[8], it is hindered by high costs, significant energy requirements for solvent regeneration, and the need for large-scale plants[9].

Recently, unsteady-state CO_2 hydrogenation processes, known as CO_2 capture and reduction (CCR) and integrated CO_2 capture and conversion, have emerged as alternative technologies in which the need for CCS is avoided[10,11]. In 2016, Urakawa et al.[12] and Farrauto et al.[13] separately published their works on CCR. Unlike conventional methods, CCR does not require large amounts of thermal energy for CO_2 separation and purification[14]. Furthermore, this process is theoretically applicable to the utilization of O_2-containing CO_2 emitted from industries such as power plants and is advantageous for practical use[15].

Dual-functional materials (DFMs) in which alkali or alkaline earth metals for CO_2 capture are combined with transition metals for CO_2 hydrogenation are widely used in CCR operations. Selective CH_4 and CO formation has been reported in various CCR studies. However, the reported CCR processes cannot be integrated with effluent streams released from various industrial processes because these are performed by changing the gas conditions stepwise (Fig. 1a). To address this, Urakawa et al. proposed a two-reactor parallel-type system for continuous CCR[12], whereas we developed a two-reactor parallel-type system for the continuous production of green fuels, such as CH_4[16,17] and CO[18,19], from a $CO_2/O_2/N_2$ mixture by alternating the feeds of $CO_2/O_2/N_2$ and H_2 to the DFMs in the two reactors (Fig. 1b). Our system can continuously capture low-concentration CO_2 (below 1%) from a mixture of O_2 and convert it into green fuels. However, continuous CCR is not applicable to high-concentration CO_2 emissions that are similar to exhaust gas emissions from thermal power plants and other industrial sources because of the limited CO_2 capacity of DFMs[20] compared with zeolite sorbents[21,22]. For example, less than 30% high-concentration inlet CO_2 (10%) can be converted even when one of the highest-activity DFMs available is used under optimized conditions.

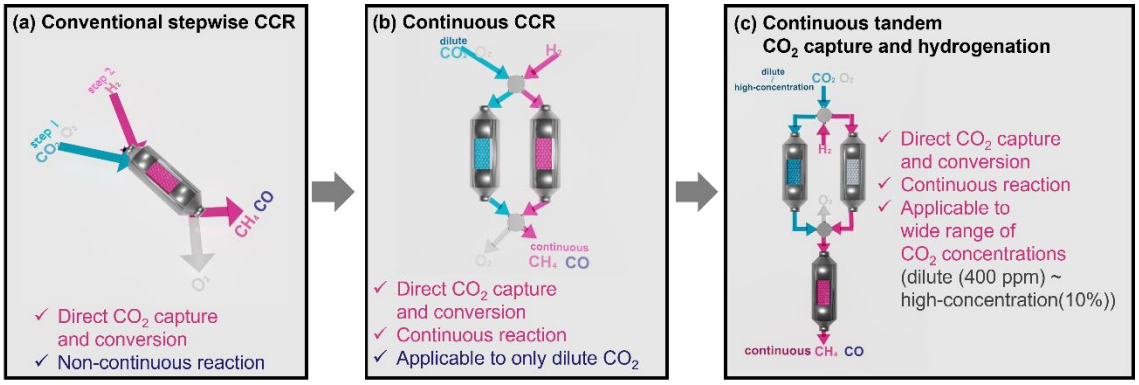

Figure 1. Conceptual diagram of (a) conventional stepwise CCR, (b) continuous CCR, and (c) continuous tandem CO_2 capture and hydrogenation processes.

In this study, we developed a novel system in which tandem CO_2 capture and hydrogenation is achieved by combining Rb-loaded zeolites (Rb-zeolites) as CO_2 adsorbents with CO_2 hydrogenation catalysts (Fig. 1c). For CO_2 hydrogenation, Ni/CeO_2[23–25] and $Cu/ZnO/Al_2O_3$[26–28] were used as typical catalysts for methanation and reverse water–gas shift (RWGS) reactions, respectively. The sorbents were filled upstream in two parallel reactors. The catalyst was filled downstream in a single reactor. The system was based on continuous temperature swing adsorption (TSA) and catalytic reactions. Initially, a $CO_2/O_2/N_2$ mixture was fed into the Rb-zeolite sorbent (denoted as Z) to capture CO_2 (Eq. 1). After this mixture changed to pure H_2 gas and the sorbent temperature was increased, the captured CO_2 and H_2 were simultaneously desorbed by applying heat (Eq. 2). Desorbed CO_2 and H_2 flowed to the bottom reactor, and the methanation or RWGS reaction proceeded using the catalysts (Eqs. 3 and 4).

$$CO_2\ (gas) + Z \rightarrow Z\text{-}CO_2\ (ad) \quad (1)$$

$$H_2 + Z\text{-}CO_2\ (ad) \rightarrow CO_2\ (gas) + H_2\ (gas) + Z \quad (2)$$

$$CO_2\ (gas) + 4H_2\ (gas) \rightarrow CH_4\ (gas) + 2H_2O\ (gas) \quad (3)$$

$$CO_2\ (gas) + H_2\ (gas) \rightarrow CO\ (gas) + H_2O\ (gas) \quad (4)$$

This new process is suitable for continuous operation under temperature-swing cycling in the low-temperature range (between 40 and 200 °C) in the presence of O_2. Compared with more than 50 reported CCR processes, this newel process exhibited high inlet CO_2 conversion.

4.2 Experimental Section

4.2.1 Sorbent and catalyst preparation

Beta (Si/Al = 5, Mitsui Mining & Smelting Co., Ltd.), 13X (Si/Al = 1.25, Junsei Chemical Co., Ltd.), and Na-Y zeolites (Si/Al = 2.75, JRC-Z-Y5.5, Tosoh Corporation) were used as sorbents and supports. To prepare Rb-loaded zeolite sorbents, Rb species were immobilized on the zeolites using the conventional impregnation method. An appropriate amount of a Rb_2CO_3 aqueous solution (AR >99%, FUJIFILM WAKO Pure Chemical Corporation) was incorporated into the zeolites. After being stirred for 3 h at 25 °C, the suspension was evaporated by using a vacuum pump at 50 °C and dried overnight at 100 °C. The solid produced was then calcined at 200 °C for 1 h to obtain the desired Rb-zeolites. Other alkali-metal-loaded zeolite sorbents were prepared by employing the same approach using K_2CO_3 (AR: 99.0%, Tokyo Chemical Industry Co., Ltd.) and Cs_2CO_3 (AR >99%, FUJIFILM WAKO Pure Chemical Corporation) as precursors.

4.2.2 Characterization

CO_2 adsorption measurements were performed by using a fixed-bed flow reactor. The zeolite sorbents (50 mg) were placed on quartz wool in the middle of a reactor, which was then placed in an electric tube furnace. The zeolite sorbents were heated to 500 °C under pure He flow (100 mL min^{-1}), maintained for 30 min to remove the CO_2 and water vapor included in zeolites, and cooled to 40 °C. The gas emitting from the reactor outlet was directly connected to a homemade IR gas cell to monitor the CO_2 concentration by performing IR measurements. In the first 30 s, before the CO_2 concentration stabilized, a flow of 1% CO_2/He was passed through the bypass line and then the feed was switched to the reactor. The CO_2 adsorption amount was calculated from the difference in CO_2 concentrations between the blank and zeolites. The TPD of CO_2 was also performed using the homemade IR gas cell. The zeolite (100 mg) was pretreated in He atmosphere at 500 °C for 30 min and then cooled to 50 °C. Next, the 1% CO_2/N_2 (100 mL min^{-1}) mixed gas was fed into the reactor for 30 min and then He was flowed for 15 min. The TPD profile was obtained by heating the sample from 30 to 200 °C at a rate of 20 °C/min under He flow. *Operando* FTIR measurements were performed during the TPD of CO_2 using a JASCO FT/IR-4600 spectrometer equipped with a mercury–cadmium–telluride detector and a flow-type quartz IR cell connected to a flow system (total flow rate = 100 mL min^{-1}). The effluent gas was simultaneously monitored by performing FTIR spectroscopy (JASCO FT/IR-4600) using a homemade gas cell. A sample pellet (40 mg; diameter: 20 mm) was introduced into a quartz cell equipped with a CaF

window. The sample pellet was pretreated at 200 °C for 30 min under He flow and cooled to 40 °C, and the 1% CO_2/He mixture was fed into the reactor for 5 min. Subsequently, the system was purged with He for 10 min and the background spectrum was recorded. Temperature-resolved measurements were performed from 40 to 200 °C. The *operando* IR measurements were performed by monitoring the desorption of CO_2 in the outlet gas mixture.

4.2.3 Continuous CO_2 capture and O_2-free CO_2 production using two parallel reactors

Continuous CO_2 capture and O_2-free CO_2 production were performed using a system similar to that in a previous study[37]. CO_2 was continuously separated by using two fixed-bed flow reactors, and the response curves for CO_2 were obtained using a blank test. Two vertical quartz reactors (a and b) containing the same sorbent powder (14 g) were placed on quartz wool in the middle of the reactor in an electric tube furnace. The sorbents were pretreated under pure He flow (100 mL min^{-1}) at 400 °C. Subsequently, continuous CO_2 capture and O_2-free CO_2 production were achieved. Two timer-controlled 4-way valves were switched simultaneously to feed a simulated exhaust gas (100 mL min^{-1}; 10% CO_2 + 10% O_2/He for 29.5 min and He for 0.5 min) and an O_2-free CO_2 gas (120 mL min^{-1}; He for 30 min); when the simulated exhaust gas was fed to reactor a, the O_2-free CO_2 gas was fed to reactor b. Effluent gases containing uncaptured CO_2 from reactors a and b (with O_2 and He) were continuously fed into effluent 1. The produced O_2-free CO_2 in reactors a and b (with He) was continuously fed into effluent 2. The effluent gas was simultaneously monitored by performing FTIR spectroscopy (JASCO FT/IR-4600) using a gas cell and a mass spectrometer (BELMass, MicrotracBEL Corp.). The CO_2 concentration was calculated using the calibration curve for the CO_2 concentration and the IR peak area in the range of 2395−2235 cm^{-1} for ≤ 1% CO_2 and 3760−3662 cm^{-1} for > 1% CO_2. The CO_2 capture efficiency and the yield of O_2-free CO_2 were calculated as follows:

$$CO_2\ capture\ efficiency\ [\%] = \frac{\int_0^t \left[F_{CO_2}^{in} - F_{CO_2}^{out(1)}(t)\right] dt}{\int_0^t F_{CO_2}^{in}(t)dt} \times 100;$$

$$Yield\ of\ O_2\ free\ CO_2\ [\%] = \frac{\int_0^t F_{CO_2}^{out(2)}(t)dt}{\int_0^t F_{CO_2}^{in}(t)dt} \times 100,$$

where $F_{CO_2}^{in}$, $F_{CO_2}^{out(1)}$, and $F_{CO_2}^{out(2)}$ are the CO_2 molar flow rates at the column inlet and the outlets of effluents 1 and 2, respectively, and t denotes the duration of one cycle.

4.2.4 Continuous CO_2 capture and methanation/RWGS reaction using the combined system with two parallel reactors for TSA and a single reactor for hydrogenation

Continuous CO_2 capture and hydrogenation (such as the methanation and RWGS reactions) were performed using homemade reactors (Fig. 1c). Two vertical quartz reactors (a and b) containing the Rb-beta sorbent powder (14 g), same as those used for O_2-free CO_2 production, were placed on quartz wool in the middle of the reactor in an electric tube furnace. For the methanation and RWGS reactions, Ni/CeO_2 and $Cu/ZnO/Al_2O_3$ (commercial, Alfa Aesar) were added to the bottom reactor (c). The sorbents were pretreated under He flow for 30 min at 400 °C. Ni/CeO_2 was pretreated with H_2 for 30 min at 400 °C. $Cu/ZnO/Al_2O_3$ was pretreated with H_2 for 30 min at 500 °C. After these pretreatments, continuous CO_2 capture and hydrogenation were performed. Similar to the continuous O_2-free CO_2 production system, 1% CO_2 + 10% O_2/He or pure He (for purging) and pure H_2 were alternately flowed to each Rb-beta under cooling and heating. The produced O_2-free CO_2 and H_2 were fed into a hydrogenation catalyst (in reactor c). Effluent 1 contained the uncaptured CO_2, O_2, and He. Effluent 2 contained the produced CH_4, CO, and unreacted CO_2. The produced H_2O was trapped before the gas concentrations were analyzed using cold trap equipment. The gas compositions in effluents 1 and 2 (CO_2, CO, and CH_4) were analyzed online by using an FTIR spectrometer (JASCO FT/IR-4600) with a gas cell. The STY_{CH4}, STY_{CO}, and CH_4 and CO yields are calculated as follows:

$$STY_{CH4}\ or\ STY_{CO}\ [mmol\ g^{-1}\ h^{-1}] = \frac{\int_0^t F_{CH_4\ or\ CO}^{out}(t)dt}{m_{cat} \times t};$$

$$CH_4\ or\ CO\ yield\ [\%] = \frac{\int_0^t F_{CH_4\ or\ CO}^{out}(t)dt}{\int_0^t F_{CO_2}^{in}(t)dt} \times 100,$$

where $F_{CH_4}^{out}$ and F_{CO}^{out} are the CH_4 and CO molar flow rates, respectively, at the column outlet of effluent 2, and m_{cat} is the catalyst mass. To determine the CO and CH_4 molar flow rates, the peak area values around 2250−2001 and 3031−2994 cm^{-1} were used, respectively.

4.3 Results and discussion

4.3.1 Screening and optimizing sorbents and catalysts

First, we examined the CO_2 adsorption properties of zeolite sorbents at 50 ºC using a fixed-bed continuous-flow system. The breakthrough curve obtained from the CO_2 adsorption measurements is shown in Fig. 2a, and the CO_2 adsorption amount determined from the breakthrough curve is presented in Fig. 2b. Among Rb-zeolites (such as Rb-13X, Rb-Y, and Rb-beta) and alkali-metal-loaded beta zeolites (such as Rb-, Na-, K-, and Cs-beta), Rb-beta

exhibited the highest amount of CO_2 adsorption. Subsequently, we performed temperature-programmed desorption (TPD) measurements of CO_2 to explore the CO_2 desorption properties of Rb-beta (Fig. 2c). CO_2 desorption from Rb-beta was observed over the temperature range of 50–150 °C, and the total amount of desorbed CO_2 (0.8 mmol/g) was close to the CO_2 adsorption amount (0.8 mmol/g). This indicated that adsorbed CO_2 at 50 °C was completely desorbed after heating to 150 °C.

To elucidate the mechanism underlying CO_2 adsorption and desorption, *operando* Fourier transform infrared (FTIR) spectroscopy was performed during the TPD of CO_2 on Rb-beta. Prior to the experiment, the infrared (IR) disk was heated under He at 400 °C for 30 min and then cooled to 40 °C. To record the background spectrum, 1% CO_2/He was fed to the sample at 40 °C for 5 min and purged under He. A strong band at 2275 cm^{-1} assigned to the physically adsorbed CO_2 on zeolite[29,30] and two weak broad bands at 1720 and 1280 cm^{-1} assigned to the carbonate species[31,32] were observed before heating (Fig. 2d). These results indicated that physically adsorbed CO_2 was the main adsorbed species and carbonate was a minor species. As the temperature increased from 60 to 160 °C, the band intensity for the physically adsorbed CO_2 sharply decreased, accompanied by CO_2 formation at the outlet of the IR cell (Fig. 2e). This indicated that the physical adsorption and desorption of CO_2 were responsible for the adsorption/desorption of CO_2 on Rb-beta.

We adopted Ni/CeO_2 and Cu/ZnO/Al_2O_3 as typical catalysts for the methanation and RWGS reactions. The reaction temperatures for these catalysts were optimized by performing steady-state reaction experiments (Fig. 3). When the Ni/CeO_2 catalyst was used, the CO_2 conversion and CH_4 selectivity sharply increased at a temperature of >150 ºC (Fig. 3a). The reaction over the temperature range of 200–500 °C resulted in nearly complete conversion of CO_2 to CH_4 (CO_2 conversion ≥97.0%, CH_4 selectivity ≥ 99.7%). In the case of the RWGS reaction with the Cu/ZnO/Al_2O_3 catalyst, the CO_2 conversion monotonically increased from 2.0% to 78.1% with the temperature over the range of 100–650 ºC (Fig. 3b). Compared with equilibrium conversion, the difference of CO_2 conversion was almost zero at 650 ºC. Further increasing the temperature to 700 °C did not significantly improve CO_2 conversion (79.4%). CO selectivity was high (≥99.3%) at a temperature of >200 ºC.

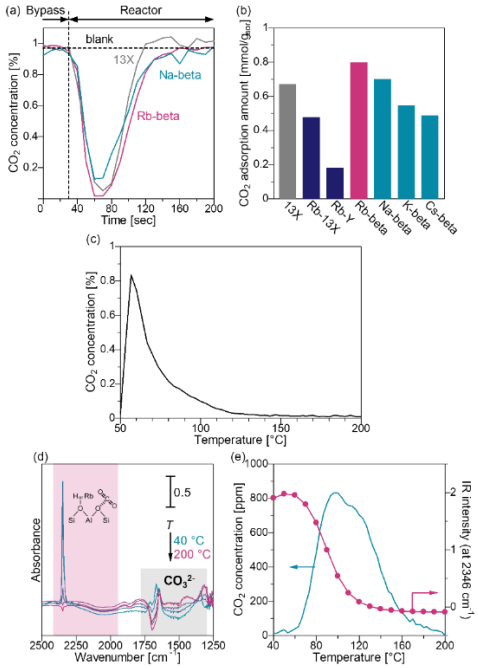

Figure 2. (a) CO_2 adsorption at 50 ºC for 200 s under a flow of 0.97% CO_2 (He balance; total flow: 100 mL/min). The flow passed through a bypass line in the first 20 s. (b) Comparison between CO_2 adsorption amounts on zeolite sorbents at 50 ºC (determined by conducting the experiment shown in Fig. 1a). (c) CO_2 TPD profiles for Rb-beta under He flow. Conditions: heated at 500 °C under He flow and then cooled to 50 °C under He flow; 1% CO_2/N_2 mixture was fed into the reactor at 50 ºC for 30 min and purged with He for 5 min. The CO_2 TPD experiment was conducted by applying heat under He flow. (d) *Operando* FTIR spectroscopy for Rb-beta under CO_2 TPD condition. IR spectra of adsorbed species at temperature intervals of 40 °C. (e) Time-resolved trends in the IR intensities of adsorbed CO_2; concentration of desorbed CO_2. The background spectrum was recorded before CO_2 capture.

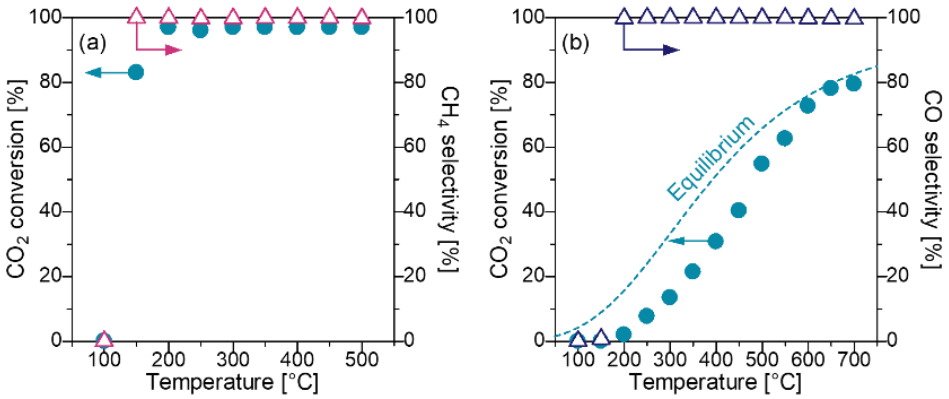

Figure 3. (a) CO_2 conversion and CH_4 selectivity with respect to reaction temperature with Ni/CeO_2 catalyst. (b) CO_2 conversion and CO selectivity with respect to reaction temperature with $Cu/ZnO/Al_2O_3$ catalyst.

4.3.2 Continuous production of O_2-free CO_2 from CO_2/O_2 mixture

Prior to the continuous CO_2 capture and hydrogenation using the coupled tandem TSA/catalyst system, we demonstrated the continuous production of O_2-free CO_2 from a model combustion exhaust gas (10% CO_2 + 10% O_2/He) using the TSA system. Fig. 4a shows a schematic of the TSA system for O_2-free CO_2 production from the model combustion exhaust gas. Two reactors containing equal amounts of Rb-beta were set up in parallel for CO_2 capture and desorption. The CO_2 concentrations in effluents 1 and 2 were monitored by performing FTIR spectroscopy, and the O_2 concentration in effluent 1 was monitored by using mass spectrometry (MS). A gas mixture of CO_2/O_2/He was fed into one reactor for 29.5 min for CO_2 capture and then purged with He (0.5 min) to remove the remaining O_2 from the reactor. The other reactor (containing CO_2-captured Rb-beta) was heated to 200 ºC under He to produce O_2-free CO_2 in effluent 2. Figs. 4b and 4d show the typical variations in the CO_2 and O_2 concentrations in effluents 1 and 2 over time, respectively. CO_2 is captured from the CO_2/O_2 mixture when the reactor is cooled from 200 to 40 ºC. During the CO_2-capture period, the outlet CO_2 concentration (in effluent 1) is below the detection limit, indicating that CO_2 is almost completely removed from the 10%-CO_2/10%-O_2 mixture. Subsequently, two 4-way valves connected to the top and bottom of the tubular reactors are simultaneously switched, and the captured CO_2 is released by heating to 200 ºC (5.5 ºC/min) under He flow; this results in the formation of O_2-free CO_2 in effluent 2. The maximum concentration of the liberated CO_2 is ~37%. The amounts of captured CO_2 (12.1 mmol) and produced O_2-free CO_2 (11.9 mmol) in one cycle, calculated by applying Eqs. 2 and 3. Note that the production of CO_2 results in an increase in the total flow rate (from 120 to 167 mL/min) of effluent 2. The CO_2 capture and desorption experiments are performed continuously for seven cycles (data not shown). These results clearly reveal the continuous production of O_2-free CO_2 from the 10%-CO_2/10%-O_2 gas mixture.

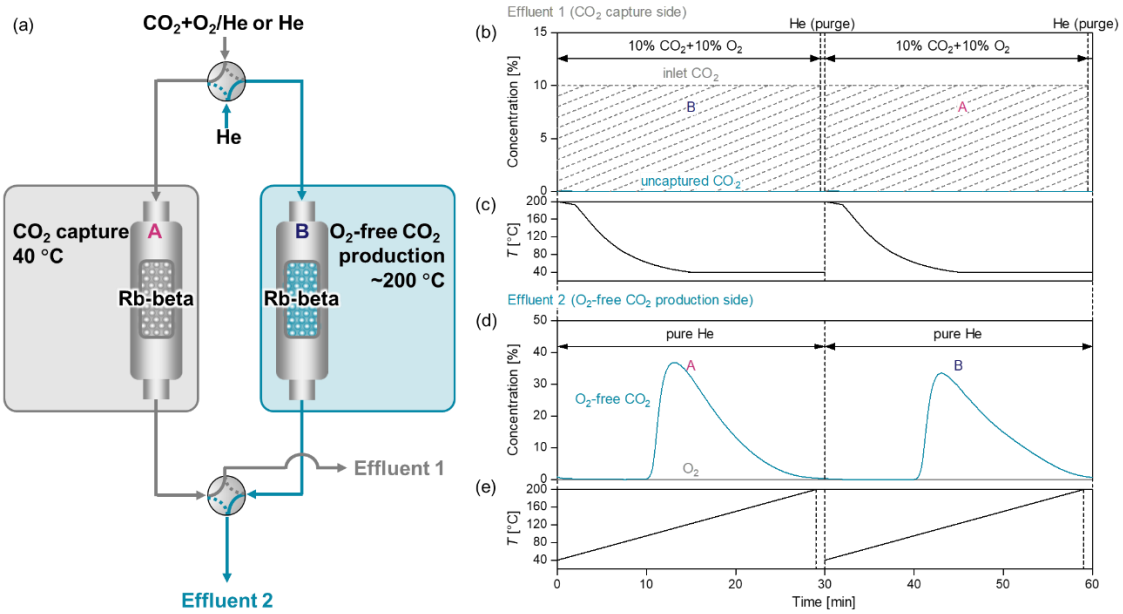

Figure 4. (a) Schematic of the two-reactor TSA system for continuous CO_2 capture and O_2-free CO_2 production; captured gas (100 mL/min, 10% CO_2 + 10% O_2/He for 29.5 min and then pure He for 0.5 min) and released gas (120 mL/min, pure He for 30 min) were alternately fed into each reactor containing 14 g of Rb-beta. (b and d) Typical variations in the CO_2 and O_2 concentrations in effluents 1 and 2 over time, respectively. (c and e) Typical temperature changes in reactors a and b over time, respectively.

4.3.2 Continuous CO_2 capture and methanation/RWGS reaction using the tandem system

Next, continuous CO_2 capture and methanation were performed using the tandem TSA/methanation system. Unlike DFM designs, the tandem-system design allows individually optimized active sites and reaction conditions for each step. The proposed TSA system converts the model combustion exhaust (10% CO_2/10% O_2) to O_2-free CO_2, which undergoes methanation under H_2 in the reactor (containing Ni/CeO_2) downstream at 300 °C (Fig. 5a). First, the CO_2/O_2 mixture is fed into one reactor of the TSA system for 29.5 min for CO_2 capture, and then, pure He (0.5 min) is fed to purge the remaining O_2 in the reactor. The other reactor (containing CO_2-captured Rb-beta) is heated to 200 ºC (5.5 ºC/min) under pure H_2 for 30 min. The desorbed CO_2 and H_2 are fed into the methanation reactor and converted to CH_4.

Figures 5b and 5d show the typical variations in the CH_4, CO_2, and O_2 concentrations in effluents 1 and 2 over time, analyzed online by employing an IR gas-cell and MS, respectively. Figures 5c and 5e depict the optimized time variations in the temperatures of the two TSA reactors. During the CO_2-capture period, the outlet CO_2 concentration (in effluent 1) is below the detection limit, indicating that CO_2 is almost completely removed from the 10%-CO_2/10%-O_2 mixture. Subsequently, two 4-way valves connected to the top and bottom of the tubular reactors are simultaneously switched, and the captured CO_2 is released by heating under H_2. When CO_2-captured Rb-beta is heated under H_2, CH_4 was observed in

effluent 2, with a maximum concentration of ~66.3%. The concentration of CO (0.02%) is low, and CO_2 is not present in effluent 2; thus, CH_4 selectivity is ≥99%. Note that the high conversion level of CO_2 and H_2 over the downstream Ni/CeO_2 catalyst results in a significant decrease in the total flow rate (from 120 to 40 mL min^{-1}) of effluent 2. The CO_2 capture and desorption/methanation experiments are performed continuously for four cycles (data not shown). The effect of the CO_2-capture temperature (40, 80, 100, and 120 °C) on the CH_4 yield reveals that the lowest temperature (40 °C) produces the highest CH_4 yield, simply because a lower adsorption temperature leads to a larger CO_2 capacity of Rb-beta. The effect of the catalyst amount shows that increasing the catalyst amount (from 2 to 15 g) results in a slight increase in the CH_4 yield (from 85 to 92%) and a large decrease in the space-time-yield of CH_4 (STY_{CH4}) (from 11.9 to 1.8 mmol g^{-1} h^{-1}).

A CH_4 yield of 92% is almost double those in the previously reported catalytic systems for the methanation of a CO_2/O_2 mixture using CCR (16 reports and 55 reaction processes presented in Fig. 6). The reaction temperature in our system (300 °C) is the lowest among the reported systems, and the inlet CO_2 concentration in our system is the highest among the reported systems. Note that the majority of the previously reported CCR systems for CH_4 production were tested in the absence of O_2 during the CO_2-capture period (10 reports and 100 reaction processes). Compared with those systems, our system produces the highest CH_4 yield.

We demonstrated continuous CO_2 capture and the RWGS reaction using a system similar to that described in the previous subsection; in this system, a commercial $Cu/ZnO/Al_2O_3$ catalyst was used as the RWGS catalyst (catalyst amount = 10 g) (data not shown). When Rb-beta was heated from 40 to 200 °C, CO was formed with a maximum concentration of ~41.0%, CO_2 was desorbed with a maximum concentration of ~11.2%, and almost no CH_4 was detected (CO selectivity ≥99%). In addition, no CO_2 was detected in effluent 1 using gas-cell IR, indicating that almost all the supplied CO_2 was captured by Rb-beta. Given the CO production per unit time, the conversion of inlet CO_2 to CO (denoted as the CO yield) was 85%, indicating that a considerable amount of the supplied high-concentration CO_2 in the presence of O_2 was continuously converted to CO. This reaction was repeated several times and maintained for at least 2 h (six cycles; data not shown). Furthermore, the amount of $Cu/ZnO/Al_2O_3$ included in this RWGS system was optimized from 0.2 to 14 g (data not shown). When the catalyst amount was between 1 to 15 g, the CO yield was over 85% and the maximum CO production rate was 20.1 mmol g^{-1} h^{-1}. When the

catalyst amount was decreased to 0.2 g, the CO yield decreased by 45% but the space-time-yield of CO (STY_{CO}) increased to 55.5 mmol g^{-1} h^{-1}. Thus, increasing the catalyst amount from 0.2 to 1 g resulted in a sharp increase in the CO yield (from 45% to 85%), but further increasing the amount from 1 to 15 g resulted in limited change (from 85% to 81%). Additionally, increasing the catalyst amount from 0.2 to 15 g significantly decreased the STY_{CO} from 55.5 to 1.5 mmol g^{-1} h^{-1}.

The system was compared with previously reported systems (10 reports and 30 reaction processes in Fig. 6b). The majority of the previously reported CCR systems for CO production were evaluated at low inlet CO_2 concentrations (below 1%). Our system demonstrated the RWGS process with a high CO yield (85%) at a high inlet CO_2 concentration (10%). Notably, many of the previously studied CCR systems aimed at CO production were tested in the absence of O_2 during CO_2 capture (10 reports and 100 reaction processes). Compared with systems with the same inlet CO_2 concentration (10%), our system demonstrated approximately twice the CO yield.

For example, in Fischer–Tropsch (FT)[33], methanol (MeOH)[34], and ethanol (EtOH) syntheses[35] from syngas, the H_2/CO ratio of the syngas significantly affects the selectivity and yield of the product. Similar to the aforementioned methanation system, the H_2 input was optimized (Fig. 7). When the H_2 flow time was reduced from 30 to 20 min in one cycle, the H_2 conversion slightly increased from 9.8% to 15% and the H_2/CO ratio changed from 9.1 to 3.7, which is closer to the ideal value of 2.0 for FT, MeOH, and EtOH syntheses, while retaining a high CO yield (93%). Furthermore, syngas is an environment-friendly alternative gaseous fuel for internal combustion during engine operations, and H_2-rich syngas (H_2/CO ≥3.0) has been reported to improve thermal efficiency[36]; this continuous RWGS process also has the potential to provide industrially valuable syngas. This technique is effective for continuous CO_2 capture and methanation. A decrease in the H_2 flow time improved the H_2 utilization efficiency (H_2 conversion increased from 38% to 58%).

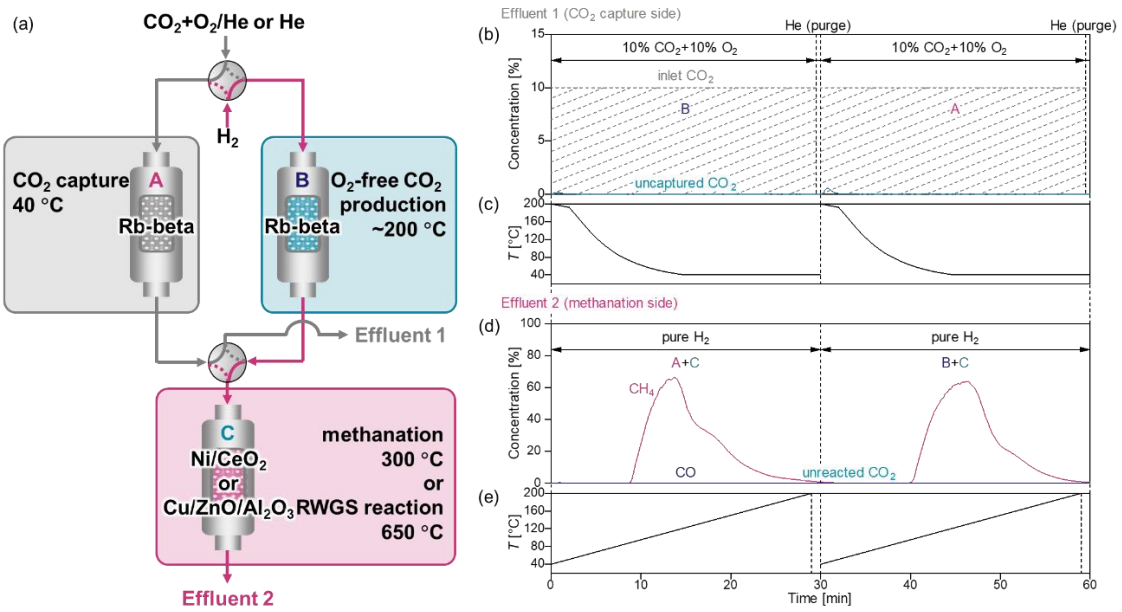

Figure 5. (a) Schematic of the two-reactor TSA system for continuous CO_2 capture and methanation; captured gas (100 mL/min; 10% CO_2 + 10% O_2/He for 29.5 min and then pure He for 0.5 min) and hydrogenation gas (120 mL/min; pure H_2 for 30 min) were alternately fed into each reactor containing 14 g of Rb-beta. (b and d) Typical variations in the CH_4, CO_2, and CO concentrations in effluents 1 and 2 over time, respectively. (c and e) Typical temperature changes in reactors a and b over time, respectively.

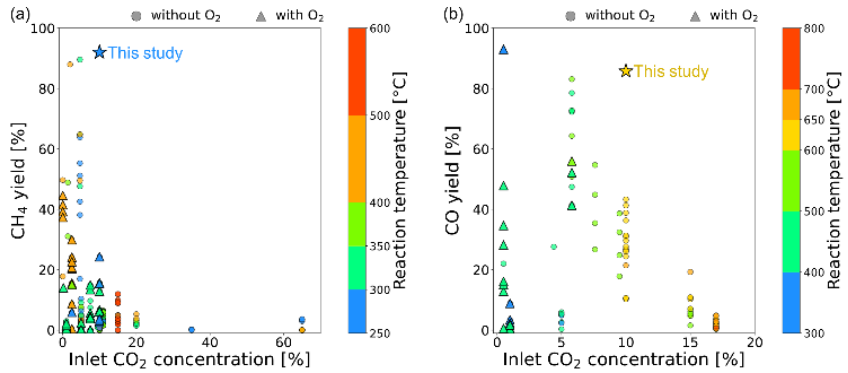

Figure 6. Performance of (a) methanation and (b) RWGS reaction processes in the proposed system and previously reported systems for exhaust or atmospheric CO_2 conversion.

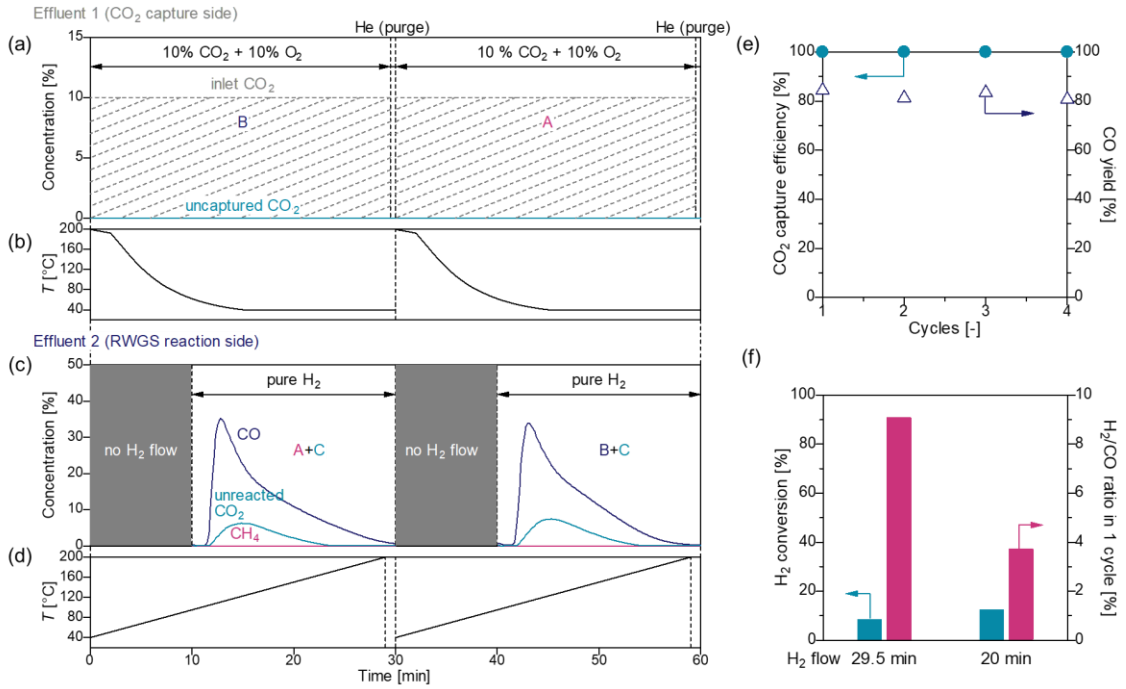

Figure 7. (a) Schematic and procedure of continuous CO_2 capture and methanation; captured gas (100 mL min^{-1}; 10% CO_2 + 10% O_2/He for 29.5 min and then pure He for 0.5 min) and hydrogenation gas (120 mL min^{-1}; pure H_2 for 20 min) were alternately fed into each reactor containing 14 g of Rb-beta. (b and d) Typical variations in the CH_4, CO_2, and CO concentrations in effluents 1 and 2 over time, respectively. (c and e) Typical temperature changes in reactors a and b over time, respectively. (f) Changes in the CO_2 capture efficiency and CO yield during cyclic test. (g) Comparison of H_2 conversion and ratio of effluent CO to H_2 in one cycle between the conditions depicted inH_2 flow for 29.5 min) and those H_2 flow for 20 min.

4.3.3 Continuous direct air capture and methanation

Next, we broadened the applicability of the proposed system for continuous CH_4 production from ambient CO_2 (Fig. 8). For ambient CO_2 capture and methanation, a high flow rate (500 mL min^{-1}) of air was fed into one TSA reactor for 60 min, whereas a low flow rate (10 mL min^{-1}) of pure H_2 was fed to the other TSA reactor (containing CO_2-captured Rb-beta) for 60 min. The H_2 and desorbed CO_2 from the other TSA reactor were subsequently fed into the downstream methanation reactor (containing Ni/CeO_2). When CO_2-captured Rb-beta was heated under H_2, the desorbed CO_2 underwent methanation on the downstream Ni/CeO_2 catalyst to produce a high concentration of CH_4. The maximum CH_4 concentration was 0.7%, and the average CH_4 concentration was ~0.4%. The results highlight the production of 10 times enriched CH_4 from atmospheric CO_2. As shown in our previous study[37], the enrichment methodology is simply based on the difference in the flow rates for CO_2 capture (500 mL min^{-1}) and reduction (10 mL min^{-1}). The proposed methanation method is also applicable to high concentrations (40%) of CO_2. The 40%-CO_2+10%-O_2 mixture undergoes methanation, and the CH_4 yield is ~70%. These results demonstrate that the proposed methanation system can be applied to a wide range of CO_2 concentrations.

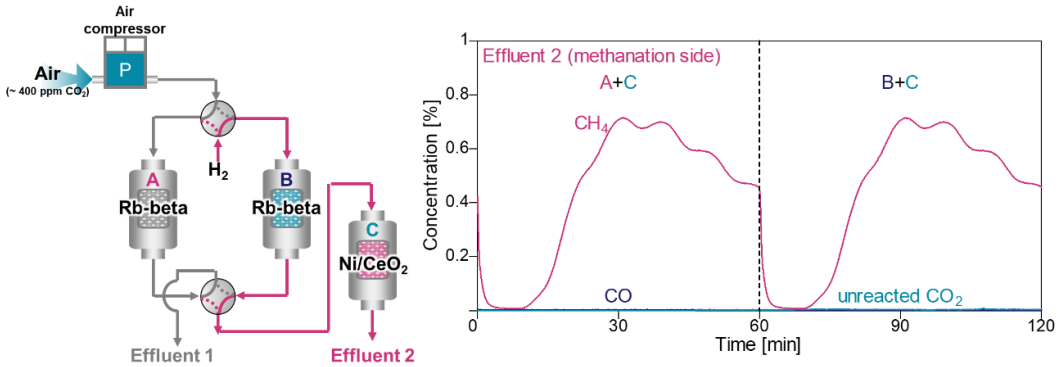

Figure 8. Schematic and typical variations in the CH_4, CO, and unreacted CO_2 amounts in effluent 2 over time for continuous direct air capture and methanation. Conditions: 14 g of Rb-beta for each upper reactor and temperature swing from 40 to 200 °C (heating rate = 20 °C/min); 15 g of Ni/CeO_2 for the bottom reactor, 300 °C, and 500 mL min^{-1} air for 60 min and switched to 10 mL min^{-1} H_2 for another 60 min.

4.3.4 Energy efficiency

To assess the energy requirements of the two processes, we analyzed the energy efficiency (η) and fuel production efficiency (FPE) of the tandem methanation and CCR systems[38]. The η for CO_2 conversion reactions was calculated using the following equation[39]:

$$\eta(\%) = \frac{\Delta H_R(\mathrm{kJ\cdot mol^{-1}})\cdot X_{CO_2}\cdot r_{CO_2,\mathrm{in}}(\mathrm{mol\cdot s^{-1}})}{P(\mathrm{kW})},$$

where $r_{CO_2,\mathrm{in}}$ represents the molar flow rate of CO_2 at the inlet of the reactor, and ΔH_R is the reaction enthalpy (−165 kJ/mol for the methanation process at 298 K). The calculated η values for the two systems are plotted as a function of time elapsed in Fig. 9a. The η for CCR is 46% at the beginning of the reaction but declines exponentially owing to the limited CO_2 capacity of the DFM. In contrast, the η for tandem methanation is significantly higher than that for CCR, owing to the lower total thermal input and greater CH_4 production. The system performances are compared in Fig. 9b. The advantages of tandem methanation over CCR are evident in terms of the CH_4 yield, CH_4 selectivity, CH_4 production per gram of the catalyst + adsorbent (to ensure a fair comparison between the two systems), and η. Note that the η for tandem methanation exceeds 100%. This is because only the power input is considered in the overall energy input and output and the net energy flow of the reactants and products is ignored. We also compared the FPEs of the two systems. The FPE for the methanation reaction is defined as the ratio of the energy output in the form of methane (not considering unreacted H_2 at the exit) to the total energy input. The output energy is estimated based solely on the low heating value of CH_4 ($\mathrm{LHV_{CH_4}}$), because the condensation heat of the produced water is typically not recovered. The energy input includes both the thermal input and the feed gas (H_2), which possesses a heating value and contributes energy to the process. Therefore, the FPE is calculated as

$$\mathrm{FPE}(\%) = \frac{\text{Output energy}}{\text{Input energy}} = \frac{\mathrm{LHV_{CH_4}(kJ\cdot mol^{-1})}\cdot r_{CH_4}(\mathrm{mol\cdot s^{-1}})}{P(\mathrm{kW}) + \mathrm{LHV_{H_2}(kJ\cdot mol^{-1})}\times\left(r_{H_2,in} - r_{H_2,out}\right)(\mathrm{mol\cdot s^{-1}})}$$

where P is the thermal input, r_{CH_4} is the mole of CH_4 production, $r_{\mathrm{H_2,in}} - r_{\mathrm{H_2,out}} = \left(n_{H_2,in} - n_{H_2,out}\right)/\Delta t$ is the rate of H_2 consumption, and $\mathrm{LHV_{H_2}}$ and $\mathrm{LHV_{CH_4}}$ are the LHVs of the converted hydrogen and methane (242 and 801 kJ/mol), respectively. As depicted in Fig. 9b, tandem methanation yields a high FPE of 83%, whereas CCR exhibits a FPE of 80%.

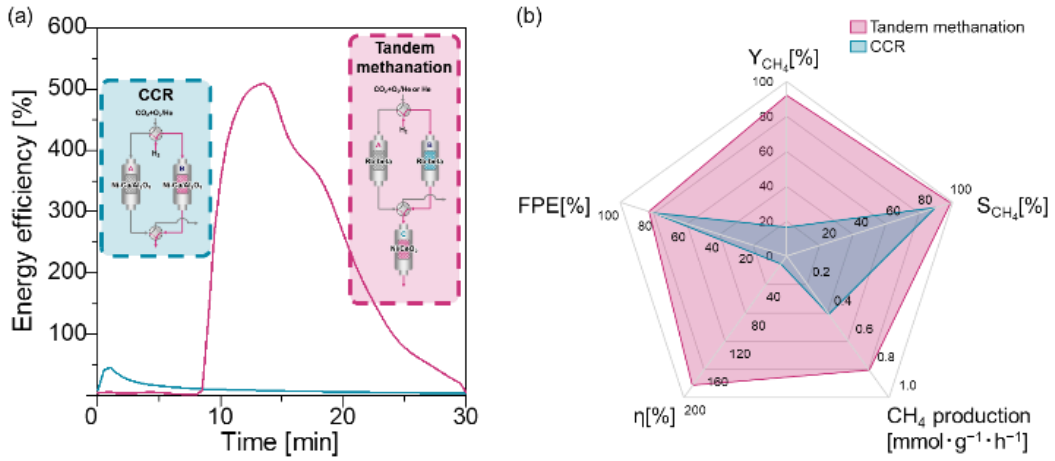

Figure 9. (a) Typical variations in the energy efficiencies of CCR and tandem methanation system over time. Conditions: 14 g of Rb-beta for each upper reactor and temperature swing from 40 to 200 °C (heating rate = 20 °C/min); 15 g of Ni/CeO_2 for the bottom reactor, 300 °C, and 500 mL/min air for 60 min and switched to 10 mL/min H_2 for another 60 min. (b) Comparison of the CH_4 yield (Y_{CH4}), CH_4 selectivity (S_{CH4}), CH_4 production, energy efficiency (η), and fuel production efficiency (FPE) between the CCR and tandem methanation systems.

4.4 Conclusions

In summary, we developed a new method for the continuous production of O_2-free CO_2, CH_4, and CO from the atmosphere and a simulated exhaust gas (CO_2/O_2/He mixture). The developed process is suitable for continuous operation over a low-temperature swing of 40–200 °C on a Rb-beta sorbent combined with a methanation system at 300 °C and a RWGS system (for syngas synthesis) at 650 °C. The results of this study revealed that the developed process is almost twice as effective as CCR for CO_2 capture and hydrogenation. We also provided evidence that the energy efficiency of the tandem methanation process based on the overall energy input and output is comparatively high because of the low power input required to operate the system and the high CH_4 production. This approach is promising for CO_2 utilization via direct air and post-combustion gas capture and conversion to green fuels. In the future, we expect that our flexible process, in combination with efficient catalysts, will contribute to a carbon-neutral society.

4.5 References

(1) Lashof, D. A. & Ahujah, D. R. *Relative Contributions of Greenhouse Gas Emissions to Global Warming*. 344, 529-531, (1990)

(2) Sanz-Pérez, E. S., Murdock, C. R., Didas, S. A. & Jones, C. W. Direct Capture of CO_2 from Ambient Air. *Chem. Rev.* vol. 116 11840–11876 (2016).

(3) Schleussner, C. F. *et al.* Science and policy characteristics of the Paris Agreement temperature goal. *Nat. Clim. Change* vol. 6 827–835 (2016).

(4) Fawzy, S., Osman, A. I., Doran, J. & Rooney, D. W. Strategies for mitigation of climate change: a review. *Environmental Chem. Lett.* vol. 18 2069–2094 (2020).

(5) Tamura, M., Honda, M., Nakagawa, Y. & Tomishige, K. Direct conversion of CO2 with diols, aminoalcohols and diamines to cyclic carbonates, cyclic carbamates and cyclic ureas using heterogeneous catalysts. *J. Chem. Technol. Biotechnol.* vol. 89 19–33 (2014).

(6) Álvarez, A. *et al.* Challenges in the Greener Production of Formates/Formic Acid, Methanol, and DME by Heterogeneously Catalyzed CO_2 Hydrogenation Processes. *Chem. Rev.* vol. 117 9804–9838 (2017).

(7) Gough, C. State of the art in carbon dioxide capture and storage in the UK: An experts' review. *Int. J. of Greenh. Gas Control* 2, 155–168 (2008).

(8) Kammerer, S., Borho, I., Jung, J. & Schmidt, M. S. Review: CO_2 capturing methods of the last two decades. *Int. J. Environ. Sci. Technol.* vol. 20 8087–8104 (2023).

(9) Patel, H. A., Byun, J. & Yavuz, C. T. Carbon Dioxide Capture Adsorbents: Chemistry and Methods. *ChemSusChem* 10, 1303–1317 (2017).

(10) Omodolor, I. S., Otor, H. O., Andonegui, J. A., Allen, B. J. & Alba-Rubio, A. C. Dual-Function Materials for CO_2 Capture and Conversion: A Review. *Ind Eng Chem Res* 59, 17612–17631 (2020).

(11) Shao, B. *et al.* CO_2 capture and in-situ conversion: recent progresses and perspectives. *Green Chemical Eng.* vol. 3 189–198 (2022).

(12) Bobadilla, L. F., Riesco-García, J. M., Penelás-Pérez, G. & Urakawa, A. Enabling continuous capture and catalytic conversion of flue gas CO_2 to syngas in one process. *J. CO2 Util.* 14, 106–111 (2016).

(13) Duyar, M. S., Treviño, M. A. A. & Farrauto, R. J. Dual function materials for CO_2 capture and conversion using renewable H_2. *Appl Catal B* 168–169, 370–376 (2015).

(14) Kosaka, F. *et al.* Enhanced Activity of Integrated CO_2 Capture and Reduction to CH_4 under Pressurized Conditions toward Atmospheric CO_2 Utilization. *ACS Sustain Chem*

Eng 9, 3452–3463 (2021).

(15) Sakai, M., Imagawa, H. & Baba, N. Layered-double-hydroxide-based Ni catalyst for CO_2 capture and methanation. *Appl Catal A Gen* 647, (2022).

(16) Li, L. *et al.* Continuous direct air capture and methanation using combined system of membrane-based CO_2 capture and Ni-Ca based dual functional materials. *Appl Catal B* 339, (2023).

(17) Li, L. *et al.* Continuous CO_2 capture and methanation over Ni-Ca/Al_2O_3 dual functional materials. *RSC Adv* 13, 2213–2219 (2023).

(18) Li, L. *et al.* Continuous CO_2 Capture and Selective Hydrogenation to CO over Na-Promoted Pt Nanoparticles on Al_2O_3. *ACS Catal* 12, 2639–2650 (2022).

(19) Li, L. *et al.* Rb-Ni/Al_2O_3 as dual functional material for continuous CO_2 capture and selective hydrogenation to CO. *Chemical Engineering Journal* 477, (2023).

(20) Lu, B. *et al.* Material design and prospect of dual-functional materials for integrated carbon dioxide capture and conversion. *Carbon Capture Science and Technology* vol. 12 100207 (2024).

(21) Dunstan, M. T., Donat, F., Bork, A. H., Grey, C. P. & Müller, C. R. CO_2 Capture at Medium to High Temperature Using Solid Oxide-Based Sorbents: Fundamental Aspects, Mechanistic Insights, and Recent Advances. *Chemical Reviews* vol. 121 12681–12745 (2021).

(22) Leperi, K. T., Yancy-Caballero, D., Snurr, R. Q. & You, F. 110th Anniversary: Surrogate Models Based on Artificial Neural Networks to Simulate and Optimize Pressure Swing Adsorption Cycles for CO_2 Capture. *Ind Eng Chem Res* 58, 18241–18252 (2019).

(23) Tada, S., Nagase, H., Fujiwara, N. & Kikuchi, R. What are the best active sites for CO2 methanation over Ni/CeO_2? *Energy Fuels* 35, 5241–5251 (2021).

(24) Zhou, G. *et al.* Role of surface Ni and Ce species of Ni/CeO_2 catalyst in CO_2 methanation. *Appl Surf Sci* 383, 248–252 (2016).

(25) Li, L. *et al.* Research Progress and Reaction Mechanism of CO_2 Methanation over Ni-Based Catalysts at Low Temperature: A Review. *Catalysts* vol. 12 (2022).

(26) Zhou, H. *et al.* Combining Atomic Layer Deposition with Surface Organometallic Chemistry to Enhance Atomic-Scale Interactions and Improve the Activity and Selectivity of Cu-Zn/SiO_2 Catalysts for the Hydrogenation of CO_2 to Methanol. *JACS Au* 3, 2536–2549 (2023).

(27) Behrens, M. *et al.* The Active Site of Methanol Synthesis over Cu/ZnO/Al_2O_3 Industrial Catalysts. *Science (1979)* 336, 893–897 (2012).

(28) Lunkenbein, T., Schumann, J., Behrens, M., Schlögl, R. & Willinger, M. G. Formation of a ZnO Overlayer in Industrial Cu/ZnO/Al_2O_3 Catalysts Induced by Strong Metal-Support Interactions. *Angew. Chem. Int. Ed.* 54, 4544–4548 (2015).

(29) Osuga, R., Yokoi, T. & Kondo, J. N. Probing the basicity of lattice oxygen on H-form zeolites using CO_2. *J Catal* 371, 291–297 (2019).

(30) Lavalley, J. C. *Infrared Spectrometric Studies of the Surface Basicity of Metal Oxides and Zeolites Using Adsorbed Probe Molecules*. *Catalysis Today* vol. 27 (1996).

(31) Busca, G. & Lorenzelli, V. Infrared spectroscopic identification of species arising from reactive adsorption of carbon oxides on metal oxide surfaces. *Materials Chemistry* 7, 89–126 (1982).

(32) Stevens, R. W., Siriwardane, R. V. & Logan, J. In situ fourier transform infrared (FTIR) investigation of CO_2 adsorption onto zeolite materials. *Energy Fuels* 22, 3070–3079 (2008).

(33) Riedel, T. *et al.* Comparative Study of Fischer-Tropsch Synthesis with H_2/CO and H_2 /CO_2 Syngas Using Fe-and Co-Based Catalysts. *Appl. Catal. A Gen.* vol. 186 (1999).

(34) Yin, X. *et al.* Characteristics of the synthesis of methanol using biomass-derived syngas. *Energy Fuels* 19, 305–310 (2005).

(35) Liu, G., Yang, G., Peng, X., Wu, J. & Tsubaki, N. Recent advances in the routes and catalysts for ethanol synthesis from syngas. *Chem. Soc. Rev.* vol. 51 5606–5659 (2022).

(36) Sahoo, B. B., Sahoo, N. & Saha, U. K. Effect of H_2:CO ratio in syngas on the performance of a dual fuel diesel engine operation. *Appl. Therm. Eng.* 49 139–146 (2012).

(37) Miyazaki, S., Yoshihara, M., Toyao, T., Maeno, Z. & Shimizu, K. Continuous production of O_2-free enriched CO_2 from ambient air using moisture swing sorbents. *Next Nanotechnol.* 3–4, 100029 (2023).

(38) Ullah, S. *et al.* Recent Trends in Plasma-Assisted CO_2 Methanation: A Critical Review of Recent Studies. *Plasma Chem. Plasma Process.* 43, 1335–1383 (2023).

(39) Dębek, R., Azzolina-Jury, F., Travert, A. & Maugé, F. A review on plasma-catalytic methanation of carbon dioxide – Looking for an efficient catalyst. *Renew. Sustain. Energy Rev.* 116, 109427 (2019

Chapter 5

CO_2 reforming by CH_4 via chemical looping technology

5.1 Introduction

The excessive emission of greenhouse gases (GHG) such as methane (CH_4) and carbon dioxide (CO_2) has become a global environmental problem[1,2]. CH_4 and CO_2 valorization, a favorable route to reduce GHG emissions, have been a subject of intense research [2–11]. Dry reforming of methane (DRM) is a promising catalytic reaction that can convert CH_4 and CO_2 to syngas (CO and H_2)[4,12–18]. Although several efficient and durable catalyst systems for DRM have been developed recently, most reported catalyst systems suffer from certain drawbacks, such as catalyst deactivation due to coke deposition and undesired CO_2 reduction by the generated H_2. Chemical looping dry reforming of methane (CL-DRM) has received considerable attention as an alternative technology to circumvent these drawbacks. CL-DRM uses oxygen storage materials (OSMs, such as MO_X) and consists of the following two-step reaction: In the first step, CH_4 reacts with OSMs to produce H_2 and CO, resulting in the reduction of OSMs (partial oxidation of CH_4 (POM), Eq. 1). In the second step, the reduced OSMs are reoxidized by CO_2 to produce CO and regenerate OSMs (CO_2 reduction, Eq. 2). Hence, in the above two-step reaction, H_2 and CO with molar ratios similar to those obtained in DRM could be realized. Although coke deposition possibly occurs during CH_4 oxidation, it can react with CO_2 to produce CO (Boudouard reaction, Eq. 3). Reduction of CO_2 by H_2 can be suppressed by separating the CO_2 and CH_4.

$$dCH_4 + MO_X \rightarrow d(CO + 2H_2) + MO_{X-d} \quad (1)$$

$$dCO_2 + MO_{X-d} \rightarrow dCO + MO_X \quad (2)$$

$$C + CO_2 \rightarrow 2CO \quad (3)$$

Otsuka and Yamanaka et al. first reported CL-DRM over CeO_2 in the presence of Pt or Pd black[19]. Subsequently, various metal oxides (NiO[20,21], FeO[20,22–24], perovskites[25–27], and hexaaluminates[28,29]) have been used as OSMs in CL-DRM. Earth-abundant NiO and FeO lose their redox activities owing to severe coke deposition and sintering, respectively. Perovskite oxides[25–27] and hexaaluminates[28,29] require high reaction temperatures (>850 °C). Although Ni-modified CeO_2 has been recently studied as an effective material for CL-DRM at lower temperatures (approximately 750 °C) by several research groups[30–35], OSMs for low-temperature CL-DRM need to be explored. Besides, the repetition of CL-DRM in previous studies was limited to a few dozen cycles[30–35], and thus the long-term durability was rarely investigated.

Metal oxide-supported WO_3, such as tungstated zirconia (WO_3/ZrO_2) and tungstated alumina (WO_3/Al_2O_3), are widely used as heterogeneous acid catalysts for hydrocarbon isomerization and cracking and biomass conversions[28–40]. Their catalytic properties strongly depend on the structure of the WO_3 species, which is influenced by their surface W density estimated from the WO_3 loading amount and specific surface area. Isolated monotungstate and/or oligomeric polytungstate species are dominant in low surface W density (<4 W atoms/nm^2) whereas three-dimensional tungstate nanoclusters and/or monolayer domains are formed with the increase of surface W density increases to 4–8 W atoms/nm^2 [36]. Various studies on the relationship between the surface W density, structure of the supported WO_3 species, and acid catalysis reported that intermediate-to-high W density (approximately 6–10 W atoms/nm^2) was optimal, showing that three-dimensional nanoclusters and/or monolayer domains are responsible for effective Brønsted acid sites rather than monomers, oligomers, or crystalline WO_3 species. Transition metal-modified WO_3/ZrO_2 and WO_3/Al_2O_3 have also been investigated as solid acid catalysts. H_2 pretreatment reduced the surface W^{6+} to W^{5+}/W^{4+} species in the Pt-WO_3/ZrO_2 system[49,50]. H_2 reduces the W species at the interface of WO_X and Pt to produce active Brønsted acid sites[45,51]. In the previous reports on syngas production from CH_4 *via* CL reactions, redox properties of supported WO_3 have also been studied. Despite bulk or supported WO_3 in the CL steam reforming of CH_4 [52–54] high-temperature conditions (900–1000 °C) are required to reduce WO_3 by CH_4. In contrast, in the CL-type POM, the Ni-modified WO_3/Al_2O_3 reacted with CH_4 at a milder reaction temperature (800 °C)[55]. A few WO_3-based catalysts have been applied for steady-state POM[56,57]. The studies mentioned above demonstrated the potential of supported WO_3 materials as OSMs for CL-type POM. However, the relationship between the structure of WO_X species and its redox properties has not yet been investigated.

In this study, we investigated CL-DRM over supported WO_3 materials. Screening of the metal oxide supports and WO_3 loading amount revealed that Ni-modified WO_3/ZrO_2 with 10.0 wt% WO_3 loading (Ni/WO_3(10)/ZrO_2) efficiently promoted CL-DRM at a relatively low temperature (750 °C). Structural analysis using N_2 adsorption, X-ray diffraction (XRD), Raman spectroscopy indicated that the highly dispersed tungstate species, including isolated monotungstate and/or oligomeric polytungstate species, on ZrO_2 functioned as oxygen storage sites in CL-DRM. Temperature-programmed surface reactions (TPSRs) indicated that dispersed tungstate species and Ni species cooperatively work on ZrO_2 to promote POM. The redox properties and local structures of dispersed tungstate species in CL-DRM were also studied using *in situ* XAS with an online mass spectrometer (*operando* XAS) and X-ray

photoelectron spectroscopy (XPS). We also compared CL-DRM performance over $Ni/WO_3(10)/ZrO_2$ with conventional DRM for long-term reactions.

5.2 Experimental Section

5.2.1 General and material synthesis

$Ni(NO_3)_2 \cdot 6H_2O$ (AR 98%) was obtained from KANTO Chemical Co., INC. WO_3 (AR 99.9%) was purchased from Sigma-Aldrich. WO_3-ZrO_2 (6.2, 10.0, and 19.5 wt% of WO_3) and ZrO_2 (RC-100) were supplied by DAIICHI KIGENSO KAGAKU KOGYO Co., Ltd. Other WO_3-loaded metal oxides were synthesized via the wetness impregnation method using $(NH_4)_{10}W_{12}O_{41}\cdot 5H_2O$ (FUJIFILM WAKO Pure Chemical Corporation) as the WO_3 precursor. Al_2O_3 was obtained by calcination of AlOOH (Catapal B alumina, Sasol Chemicals) at 900 °C for 3 h. SiO_2 (Q-10) (Fuji Silysia Chemical Ltd.) and MgO (JRC-MGO-3), and TiO_2 (JRC-TIO-4) were obtained from the Catalysis Society of Japan and used as received. An appropriate amount of $(NH_4)_{10}W_{12}O_{41}\cdot 5H_2O$ was impregnated into each support. After stirring for 3 h at room temperature (approximately 25 °C), the suspension was evaporated at 50 °C using a vacuum pump and then dried at 100 °C overnight. The solid obtained was calcined at 500 °C for 3 h to yield the WO_3-loaded support. Ni-modified WO_3/ZrO_2 was synthesized via a precipitation method using urea as the precipitating agent. An appropriate amount of $Ni(NO_3)_2\cdot 6H_2O$ and urea were dissolved in deionized water, and then WO_3/ZrO_2 was added. The mixed suspension was stirred at 90 °C for 24 h. The solid obtained was separated by centrifugation and washed five times with deionized water. The resulting solid was dried overnight in an oven at 90 °C and then calcined at 500 °C in the air for 3 h. Ni-modified WO_3-loaded metal oxides were synthesized similarly. In our previous study of CL-DRM using Ni-modified CeO_2, higher Ni loading resulted in severe coke formation[33]. To avoid the coke formation for investigation of the CH_4 partial oxidation over tungstate species and its redox reaction, we chose a very low Ni loading amount of 0.5 wt%. For the preparation of the $Ni/WO_3(10)/ZrO_2$ having mainly monoclinic phase (denoted as $Ni/WO_3(10)/ZrO_2$–monoclinic), $Zr(OH)_4$ (JRC-ZRO-6) was calcined at 500 °C for 3 h to synthesize monoclinic ZrO_2.

5.2.2 Chemical looping dry reforming of methane (CL-DRM)

CL-DRM was performed under atmospheric pressure in an electrically heated reactor with a quartz reaction tube. The quartz reaction tubes were filled 40 mg of fine powder materials. The temperature was raised to 750 °C for 20 min under a He flow. The reaction was performed by periodically switching the gas between 1% CH_4/He (100 mL/min) and 1%

CO_2/He (100 mL/min) using a timer-controlled valve. The gas hourly space velocity (GHSV) value was approximately 119000 h^{-1}. The generated CO and unreacted CH_4 and CO_2 were analyzed using an online Fourier transform infrared (FTIR) spectrometer (SHIMADZU-IRSpirit) and a gas cell. Note that we checked the response curve of CH_4 and CO_2 by blank test and calculated the actual molar amount of CH_4 and CO_2 flowed in 1 cycle. Based on these calculated values, we determined the conversion values. The generated H_2 during CH_4 flow was analyzed using a gas chromatography-mass spectrometer (GC-MS, JEOL JMS-Q1500GC).

5.2.3 Characterization

N_2 adsorption measurements were performed using an AUTOSORB 6AG instrument (Yuasa Ionics Co., Ltd.). Note that, for N_2 adsorption measurements, the material after calcination was further calcined at 200 °C for 3 h under pure He. The WO_3 surface density was calculated the following equation based on the specific surface area obtained from N_2 adsorption measurements.

$$\mathrm{WO_3\ surface\ density\ [W\ atoms/nm^2]} = \frac{\mathrm{Amount\ of\ WO_3\ unit\ [W\ atoms/g\_cat]}}{\mathrm{specific\ surface\ area\ [m^2/g\_cat]}}$$

$$= \frac{\left(\frac{\mathrm{WO_3\ loading\ [g/g\_cat]}}{\mathrm{Molecular\ weight\ of\ WO_3\ [g/mol]}} \times \mathrm{Avogadro\ constant\ [atoms/mol]}\right)}{\mathrm{Specific\ surface\ area\ [m^2/g\_cat]}}$$

CH_4- and CO_2-TPSRs were conducted using the same reactor system used for CL-DRM. The effluent gas was analyzed by FTIR and GC-MS. XRD measurements were performed using a Rigaku MiniFlex II/AP diffractometer with Cu Kα radiation. Raman spectra were obtained using a JASCO NRS-5500 spectrophotometer at a laser wavelength of 532 nm. High-angle annular dark-field scanning transmission electron microscopy (HAADF-STEM) images were recorded on an FEI Titan G2 microscope equipped with an energy-dispersive X-ray (EDX) analyzer. XPS spectra were measured on a JEOL JPC-9010MC spectrometer in a modified ultrahigh vacuum (UHV) chamber employing Mg Kα radiation. All the XPS spectra were corrected for charging by referencing the O 1s peak to 532.0 eV and analyzed after Shirley's background subtraction. Curve-fitting analysis was performed using Fityk software ver 1.3.1. The function used for curve fitting is Gaussian. Note that a series of as-prepared catalysts (calcined at 500 °C) were used for characterization. The Ni/WO_3(10)/ZrO_2 used for CL-DRM at 750 °C was also analyzed in similar ways without further treatment. For XPS measurement, the catalysts were treated under CH_4 or CO_2 at 750 °C and then transferred to a chamber without exposure to air.

5.2.4 *In situ*/*operando* XAS study

W L_3-/L_1-edge, Ni K-edge, and Zr K-edge X-ray absorption near-edge structure (XANES) measurements were performed on a medium-length hard X-ray bending magnet (BL14B2) beamline at SPring-8 (Japan, Harima) using a Si (311) double-crystal monochromator (Proposal Nos. 2020A1695 and 2022A1827). W L_3-/L_1-edge and Zr K-edge XANES studies were performed in transmission mode. A sample pellet prepared using 40 mg of the material (φ = diameter of the pellet, φ = 7 mm) was introduced into a quartz cell equipped with Kapton film windows and gas lines connected to the mass spectrometer for *in situ* analysis. The material was heated to 750 °C in He (100 mL/min), and then the spectrum was recorded (corresponding to before the reaction). A reaction gas containing CH_4 (1% CH_4/He, 100 mL/min) was allowed to flow for 10 min, followed by a reaction gas containing CO_2 (1% CO_2/He, 100 mL/min) for 10 min. Subsequently, the reaction gas was switched to 1% CH_4/He and changed again to 1% CO_2/He for 6 min. Ni K-edge XANES spectra were obtained in the fluorescence mode. A sample pellet prepared using 50 mg of the material (φ = 10 mm) was introduced into a quartz cell equipped with Kapton film windows and connected to gas lines. XAS spectra were analyzed using Athena software ver. 0.9.25 included in the Demeter package[58]. Note that, for the analysis of W L_3-edge EXAFS spectra of Ni/WO_3(10)/ZrO_2, the normalized EXAFS was converted to units of $Å^{-1}$, and then Fourier transformed over the range of 3.0–11.0 $Å^{-1}$ because of the absorption edge of Hf L_2-edge.

5.3 Results and discussion

5.3.1 Screening of supports, active metal species, and WO_3 loading amount

Figure 1 shows the concentration profile of the outlet gas in the CL-DRM over Ni/WO_3(10)/ZrO_2 and Ni-modified WO_3 (Ni/WO_3) and ZrO_2 (Ni/ZrO_2), each having 0.5 wt% of Ni. 1% CH_4/He and 1% CO_2/He gas flowed alternately over the materials every 5 min. The average amount of CO for three redox cycles and the total amount of CO formed for a series of WO_3-based materials are summarized in Table 1. Ni/WO_3 and Ni/ZrO_2 exhibited very low activity for the CH_4 oxidation and CO_2 reduction, resulting in less amount of CO during CH_4 flow (0.06 and 0.10 mmol/g CO for Ni/WO_3 and Ni/ZrO_2, respectively, Table 1, entries 1 and 2). In contrast, Ni/WO_3(10)/ZrO_2 (Ni = 0.5 wt%) efficiently promoted CH_4 oxidation and CO_2 reduction to yield 1.16 and 2.04 mmol/g of CO, respectively, which is the highest among all materials (Table 1, entry 3). H_2 (4.06 mmol/g) was produced during CH_4 flow, confirming the POM to CO and H_2. The molar ratio of the generated H_2 and CO (H_2/CO) was higher than the theoretical H_2/CO molar ratio of 2, which indicates that a side reaction in which CH_4

decomposed to form H_2 and coke also occurred. The coke reacted with CO_2 to form CO, producing more CO during CO_2 flow (2.04 mmol/g) than CH_4 flow (1.16 mmol/g). The desorbed CO_2 species was not detected during CH_4 flow, indicating that accumulation of CO_2 as carbonate species was unlikely to occur. $WO_3(10)/ZrO_2$ without Ni modification exhibited a quite low activity in the CL-DRM reaction (Table 1, entry 4). The Ni modification dramatically improved the CL-DRM activity of $WO_3(10)/ZrO_2$, indicating the cooperative work of tungstate and Ni species in CL-DRM.

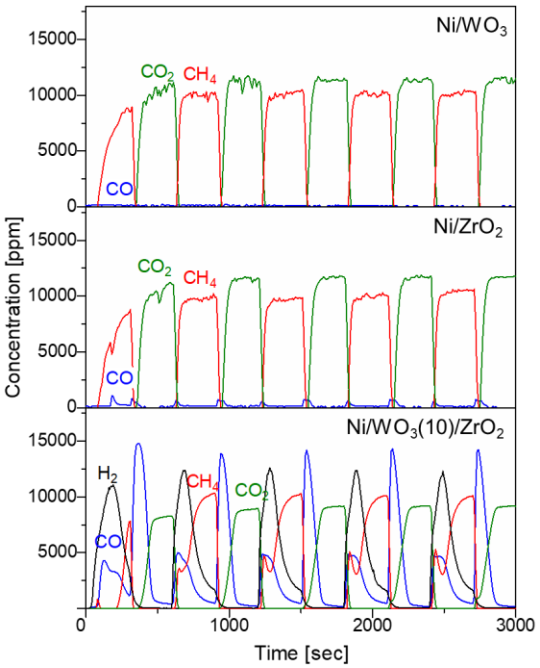

Figure 1. Effluent concentration profiles of CO_2, CH_4, CO, and H_2 in CL-DRM over Ni/WO_3, Ni/ZrO_2, and $Ni/WO_3(10)/ZrO_2$. Conditions: 40 mg material, 750 °C, 100 mL/min flow rate. The redox cycle of 1% CH_4/He (5 min) and 1% CO_2/He (5 min) was repeated five times.

Table 1. Results of CL-DRM over metal loaded metal oxide materials.

Entry	Material	Average value of CO of 3 cycles[a] [mmol/g]		
		CH_4 oxidation	CO_2 reduction	Total
1	Ni/WO_3	0.06	0.04	0.10
2	Ni/ZrO_2	0.10	0.10	0.19
3	$Ni/WO_3(10)/ZrO_2$	1.16	2.04	3.20
4	$WO_3(10)/ZrO_2$	0.08	0.06	0.14
5	$Ni/WO_3(10)/Al_2O_3$	0.12	0.06	0.18
6	$Ni/WO_3(10)/SiO_2$	0.07	0.00	0.07
7	$Ni/WO_3(10)/MgO$	0.00	0.00	0.00
8	$Ni/WO_3(10)/TiO_2$	0.67	0.49	1.16
9	$Fe/WO_3(10)/ZrO_2$	0.12	0.03	0.15
10	$Co/WO_3(10)/ZrO_2$	0.95	1.79	2.74
11	$Cu/WO_3(10)/ZrO_2$	0.08	0.01	0.09
12	$Ni/WO_3(6.2)/ZrO_2$	0.71	1.13	1.54
13	$Ni/WO_3(19.5)/ZrO_2$	1.10	0.75	1.85
14	$Ni/WO_3(30)/ZrO_2$	0.05	0.00	0.05

Conditions:40 mg material, 750 °C, and 100 mL/min flow rate. The redox cycle of 1% CH_4/He (5 min) and 1% CO_2/He (5 min) was repeated five times. [a] Average values of the second, third, and fourth cycles are used.

Ni (0.5 wt%) was loaded with WO_3 (10.0 wt%)-loaded metal oxides (Al_2O_3, SiO_2, MgO, or TiO_2) to prepare the $Ni/WO_3(10)/Al_2O_3$, $Ni/WO_3(10)/SiO_2$, $Ni/WO_3(10)/MgO$, and $Ni/WO_3(10)/TiO_2$ materials. Al_2O_3, SiO_2, and MgO were ineffective supports (Table 1, entries 5–7). $Ni/WO_3(10)/TiO_2$ showed moderate activity in CL-DRM; however, the amount of CO formed (1.16 mmol/g, Table 1, entry 8) was lower than that formed for $Ni/WO_3(10)/ZrO_2$ (3.20 mmol/g, Table 1, entry 3). Instead of Ni, base metals (Fe, Co, and Cu) were loaded on $WO_3(10)/ZrO_2$, and their activities were compared with $Ni/WO_3(10)/ZrO_2$. The total amount of CO formed for $Co/WO_3(10)/ZrO_2$ (Table 1, entry 10) was lower than that formed for $Ni/WO_3(10)/ZrO_2$. Modification with Fe or Cu (Table 1, entries 9 and 11) did not significantly improve the CL-DRM activity of $WO_3(10)/ZrO_2$. These results indicate that the combination of Ni, WO_3, and ZrO_2 is ideal for the CL-DRM.

In addition, the WO_3 loading amount (6.2–30.0 wt%) on $Ni/WO_3/ZrO_2$ was screened (Table 1, entries 3 and 12–14). The total amount of CO produced increased with WO_3 loading up to 10.0 wt%. Further increase in loading amount to 19.5 wt% decreased the total amount of CO produced to 1.85 mmol/g (Table 1, entry 13). The CL-DRM reaction barely proceeded for a WO_3 loading amount of 30.0 wt%, producing less CO (Table 1, entry 14). Based on

these results, 10.0 wt% of WO_3 was the optimal loading amount over the $Ni/WO_3/ZrO_2$ for an efficient CL-DRM reaction. The total amount of CO produced (Figure 2, green symbols) shows a volcano-type dependence on WO_3 loading, and the material with 10.0 wt% WO_3 shows the largest value. The molar ratio of the CO generated during CH_4 flow on WO_3 in $Ni/WO_3/ZrO_2$ (denoted as CO_{CH4}/WO_3) was also determined (Figure 2, red symbols). The CO_{CH4}/WO_3 values for materials with 6.2 and 10.0 wt% of WO_3 are 2.64 and 2.70, respectively, where the amount of W involved in redox reaction was estimated as approximately 90%. The molar amount of loaded WO_3 was about 5 times higher than that of loaded Ni in $Ni/WO_3(10)/ZrO_2$. Almost all of tungstate species are involved the CL-DRM despite the relatively low loading amount of Ni, implying that the tungstate species far from Ni species also cooperatively work. Above 10.0 wt%, CO_{CH4}/WO_3 monotonically decreased with WO_3 loading, implying that the unreactive WO_3 species increased with WO_3 loading above 10.0 wt%.

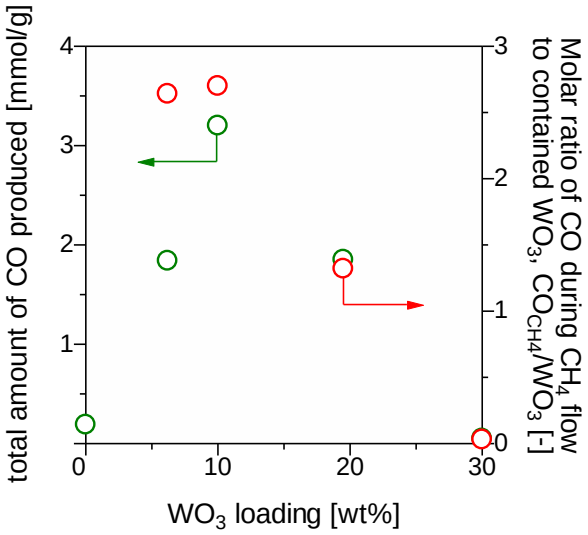

Figure 2. Relationship between WO_3 loading amount and the total amount of CO produced. The total amount of CO formed (green) and the CO generated during CH_4 flow on WO_3 in $Ni/WO_3/ZrO_2$ (red) used in CL-DRM (CO_{CH4}/WO_3) are shown. The amount of CO produced is the average of second, third, and fourth cycle values.

In the literature, on the acid catalysis of WO_3/ZrO_2[36], the effect of WO_3 loading on the catalytic activity has been discussed in terms of the surface W density. It is evident that three dimensional clusters and/or domains are dominant tungstate species on intermediate W density (4–8 W atoms/nm^2) catalysts, which show higher catalytic activity. In contrast, highly dispersed tungstate species on low W density (0–4 W atoms/nm^2) catalysts and surface crystalline WO_3 on high W density (> 8 W atoms/nm^2) catalysts exhibit low catalytic activity [36]. To elucidate the active tungstate species for CL-DRM, the surface W density for a series

of Ni-modified WO_3/ZrO_2 was calculated based on the WO_3 loading amount and specific surface area (Table 2). All WO_3/ZrO_2 materials showed a high specific surface area in the 105–139 m^2/g range. The surface areas did not markedly decrease after the Ni loading. The WO_3 surface density values were 1.4, 1.9, 3.7, and 7.0 W atoms/nm^2 for materials containing 6.2, 10.0, 19.5, and 30.0 wt% WO_3, respectively. The results indicate that dispersed tungstate species, such as isolated monotungstate and/or oligomeric polytungstate species, are dominant on $Ni/WO_3/ZrO_2$ containing 6.2 or 10.0 wt% WO_3, whereas larger tungstate species, including three-dimensional clusters and/or domains, are the main W species on $Ni/WO_3(30)/ZrO_2$. The material with 10.0 wt% WO_3 produced the highest amount of CO (Figure 2), indicating that dispersed tungstate species are more active than larger tungstate species in CL-DRM. The above trend differs for acid catalysis, in which three-dimensional tungstate nanoclusters and/or domains are responsible for highly active acid sites. For $Ni/WO_3(19.5)/ZrO_2$, the WO_3 surface density was close to 4.0 W atoms/nm^2, which indicates that dispersed and larger tungstate species possibly co-existed. The WO_3 surface density (1.7 W atoms/nm^2) for $Ni/WO_3(10)/Al_2O_3$ was similar to that for $Ni/WO_3(10)/ZrO_2$ (2.0 W atoms/nm^2). The amount of CO produced in the case of $Ni/WO_3(10)/Al_2O_3$ was less compared to that in the case of $Ni/WO_3(10)/ZrO_2$ (Table 1), indicating that the activity of surface monotungstate species depends on the support material.

Table 2. Specific surface area of the materials and the corresponding WO_3 surface densities

Material	Specific surface area[a] [m^2/g]	WO_3 surface density[b] [W atoms/nm^2]
$WO_3(6.2)/ZrO_2$	115	1.4
$WO_3(10)/ZrO_2$	135	1.9
$WO_3(19.5)/ZrO_2$	146	3.5
$WO_3(30)/ZrO_2$	112	7.0
$WO_3(10)/Al_2O_3$	148	1.8
$Ni/WO_3(6.2)/ZrO_2$	105	1.5
$Ni/WO_3(10)/ZrO_2$	127	2.0
$Ni/WO_3(19.5)/ZrO_2$	139	3.7
$Ni/WO_3(30)/ZrO_2$	121	6.4
$Ni/WO_3(10)/Al_2O_3$	157	1.7

[a]Specific surface area was determined by N_2 adsorption measurements. [b]WO_3 surface density was estimated from its specific surface area.

XRD analysis of WO_3/ZrO_2 with different WO_3 loading amounts was performed to examine the presence of crystalline WO_3 (Figure 3). For $WO_3(30)/ZrO_2$, small peaks

assignable to crystalline WO_3 (2θ = 23°–25°) were detected, along with strong peaks attributed to tetragonal ZrO_2. In contrast, materials with lower WO_3 loading amounts showed diffraction peaks for tetragonal and hexagonal ZrO_2, whereas no diffraction peaks were observed for WO_3, indicating the absence of crystalline WO_3 in these materials. In the context of ZrO_2 phase, the WO_3 loading induced the structural change of ZrO_2 from monoclinic phase to tetragonal one because the addition of tungstate specie stabilizes metastable tetragonal phase[36]. To investigate the effect of crystal phase of ZrO_2, the Ni/WO_3(10)/ZrO_2 having mainly monoclinic phase was prepared and then applied to CL-DRM reaction (data not shown). Although the CO formation amount slightly decreased (data not shown), the effluent concentration profiles were similar to those obtained using the original one (data not shown), suggesting that different crystal phase did not significantly affect the CL-DRM. The Figure 4 shows the Raman spectra of WO_3/ZrO_2 with WO_3 loadings of 6.2, 10.0, and 19.5 wt%. The bands below 700 cm^{-1} are attributed to ZrO_2. The Raman band attributed to crystalline WO_3 (820 cm^{-1}) was absent in all materials, which is consistent with the XRD results. The peak at approximately 900–1000 cm^{-1} was attributed to the W=O vibration of isolated monotungstate or oligomeric polytungstate species on the ZrO_2 surface. This peak shifted to higher wavenumbers (from 920 to 970 cm^{-1}) as the WO_3 loading amount increased. A similar peak shift was reported in a previous study by Wachs et al., and the peak shift was due to the transformation of surface monotungstate to polytungstate species[59]. The peaks specified for monoclinic for monoclinic ZrO_2 were observed at 306, 345, 378, 534, 554, and 614 cm^{-1}, while the peak at 329 cm^{-1} was attributed at tetragonal ZrO_2. The peaks at 473 and 634 cm^{-1} were assignable to both monoclinic and tetragonal ZrO_2[60–63]. These observations showed the presence of both phase, which is consistent with the results of XRD.

Based on the above results, the effect of the WO_3 surface density on the total amount of CO produced in CL-DRM (Figure 5) can be explained as follows: isolated monotungstate or oligomeric polytungstate species on low-W density materials are responsible for CL-DRM activity in the co-presence of Ni species. The inert nature of the materials loaded with the highest amount of WO_3 indicates that crystalline WO_3 is inactive.

Detailed characterization of the optimum Ni/WO_3(10)/ZrO_2 material was conducted. The XRD patterns of WO_3(10)/ZrO_2 and Ni/WO_3(10)/ZrO_2 were similar, and crystalline Ni or NiO peak was not observed for Ni/WO_3(10)/ZrO_2 (Figure 6). STEM and EDX analyses revealed that Ni and W species were highly dispersed on ZrO_2 (Figure 7). These results indicate that dispersed monotungstate and Ni species co-exist on the surface of the ZrO_2 support before the reaction. We performed the NH_3-TPD measurement for Ni/WO_3(10)/ZrO_2

to assess the surface acid sites. The TPD profile showed the desorption peak centered at around 400 °C (data not shown). The similar desorption peak was observed in NH_3-TPD measurement for WO_3/ZrO_2 regardless of different WO_3 loading amount and presence/absence of metal modifier[41].

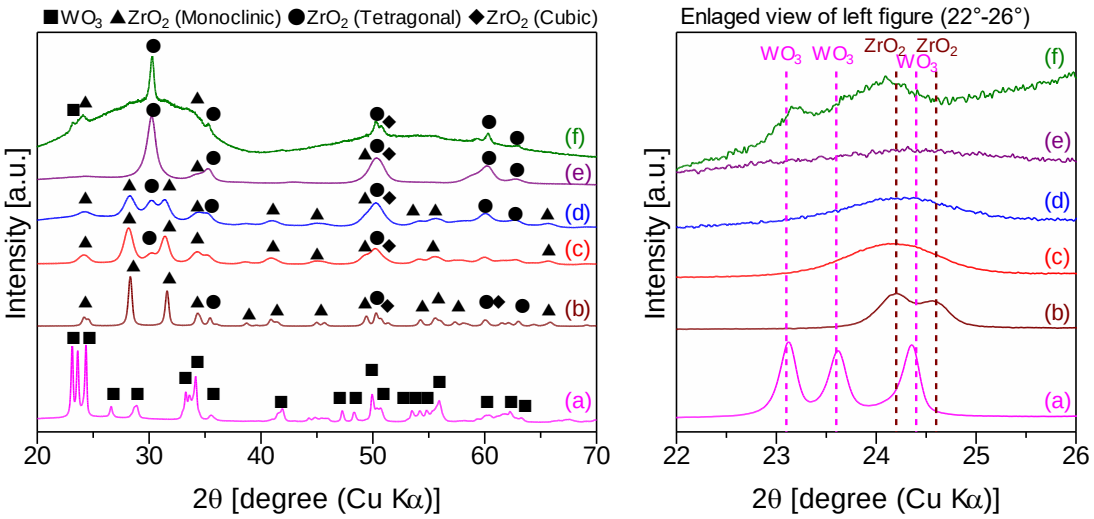

Figure 3. XRD patterns for (a) WO_3, (b) ZrO_2, (c) $WO_3(6.2)/ZrO_2$, (d) $WO_3(10)/ZrO_2$, (e) $WO_3(19.5)/ZrO_2$, and (f) $WO_3(30)/ZrO_2$

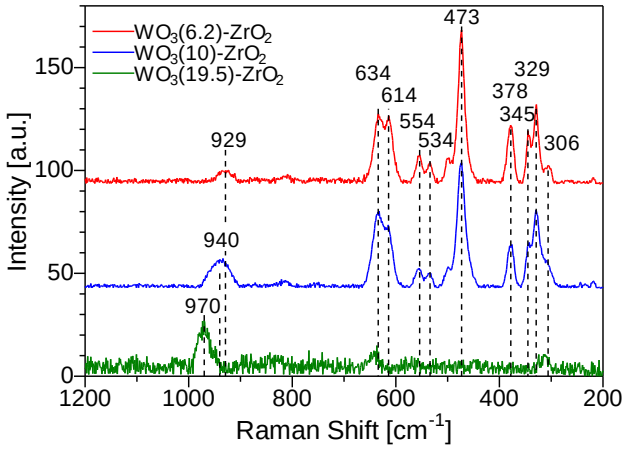

Figure 4. Raman spectra of $WO_3(6.2)/ZrO_2$, $WO_3(10)/ZrO_2$, and $WO_3(19.5)/ZrO_2$

.

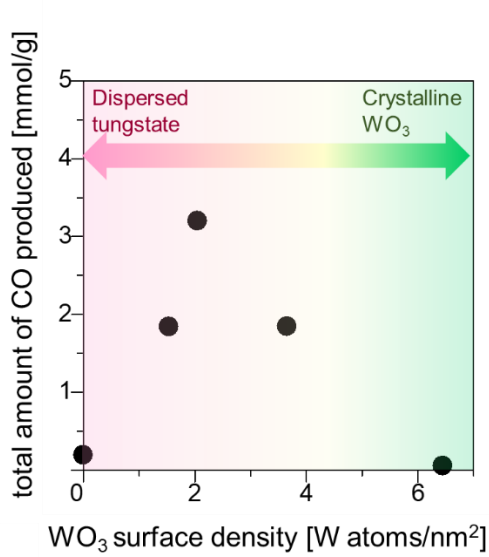

Figure 5. Relationship between the total amount of CO produced (first cycle) in CL-DRM and WO_3 surface density.

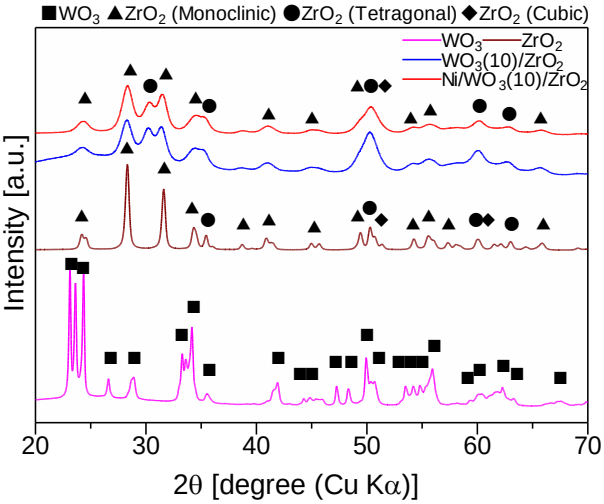

Figure 6. Relationship between the total amount of CO produced (first cycle) in CL-DRM and WO_3 surface density.

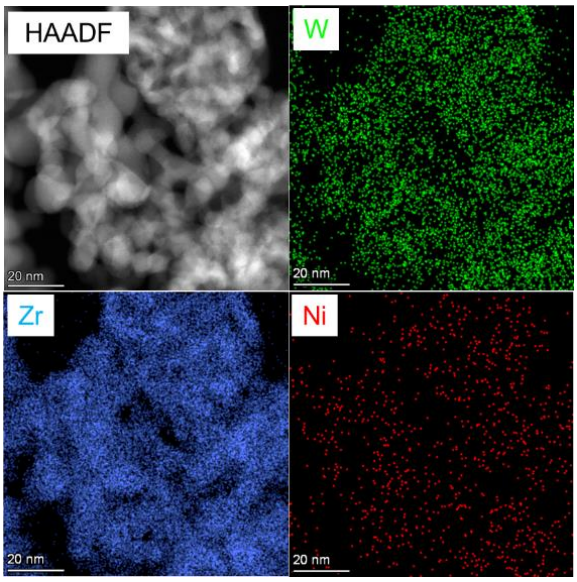

Figure 7. STEM image and elemental mapping obtained via EDX spectroscopy for Ni/WO_3(10)/ZrO_2.

5.3.2 Redox property of dispersed tungstate species in Ni/WO_3(10)/ZrO_2

The above results demonstrate that dispersed tungstate species play a key role in CL-DRM over Ni/WO_3(10)/ZrO_2. To gain insight into the role of tungstate species, CH_4-TPSR and CO_2-TPSR were successively performed for Ni/WO_3(10)/ZrO_2. For the CH_4-TPSR, the prepared materials were used without any pre-treatment. For the CO_2-TPSR, the samples used in the CH_4-TPSR were cooled down to room temperature under He flow and used for the measurement without exposure to air. During the CH_4-TPSR (Figure 8a), CH_4 was consumed, and CO and H_2 were formed above 650 °C. The first reduction peak was observed at 660 °C, and the second reduction peak was observed above 690 °C. The temperatures for CH_4 consumption and CO and H_2 formation were nearly the same for the first reduction peak indicating that tungstate species oxidized CH_4 to yield CO and H_2 at 660 °C. In the case of the second peak, the CO formation peak was lower than that of the CH_4 consumption peak indicating partial conversion of the CH_4 to coke. After performing the CH_4-TPSR, the Ni/WO_3(10)/ZrO_2 sample was cooled under He and then used for the CO_2-TPSR experiment. As shown in Figure 8b, CO formation co-occurred with CO_2 consumption at around 550–700 °C, demonstrating that CO_2 oxidized the CH_4-reduced Ni/WO_3(10)/ZrO_2 to yield CO. In CH_4-TPSR, the amount of CH_4 consumption and CO formation was determined as 1.91 mmol/g and 1.28 mmol/g, respectively, while CO_2 was hardly detected, resulting in 0.63 mmol/g of coke accumulation. In CO_2-TPSR, the CO formation amount (2.15 mmol/g) was larger than the CO_2 consumption amount (1.60 mmol/g) by 0.55 mmol/g, which is similar to the coke formation amount, indicating the occurrence of the Boudouard reaction. WO_3(10)/ZrO_2 and Ni/WO_3(30)/ZrO_2 were used for CH_4-TPSR and CO_2-TPSR control experiments. However,

the reduction and oxidation peaks were not observed. These results indicate that surface monotungstate species are reduced through POM in the presence of Ni species and subsequently reoxidized by CO_2. The occurrence of CH_4 decomposition over interface over Ni and WO_3/ZrO_2 was also reported by Kumar et al[61].

XPS experiments were performed to identify the changes in the oxidation state of W in $Ni/WO_3(10)/ZrO_2$ after the CL-DRM cycles (Figure 9). The material after CH_4 treatment and subsequent CO_2 treatment at 750 °C was transferred to an XPS chamber without exposure to air. The XPS spectrum of the W 4f region for $Ni/WO_3(10)/ZrO_2$ exhibited $4f_{5/2}$ and $4f_{7/2}$ peaks at 39.3 and 37.4 eV, respectively, which were assigned to W^{6+}. After the CH_4 treatment, the W 4f peaks significantly shifted to lower binding energies and overlapped with the Zr^{4+} peak at 32.8 eV, which indicates the reduction of W^{6+} species. The overlapped peaks around 41.0–29.0 eV were deconvoluted into the following 5 pairs: W^{6+} (37.3 and 35.3 eV), W^{5+} (36.0 and 34.0 eV), W^{4+} (34.7 and 32.7 eV), W^0 to W^{3+} (33.2 and 31.2 eV), and Zr^{4+} (37.7 and 35.3 eV) [64]. The peak due to W^0 to W^{3+} was the largest, which indicates that low-valent W species (W^0 to W^{3+}) were mainly formed after the CH_4 treatment. Following the reaction of CH_4-treated $Ni/WO_3(10)/ZrO_2$ with CO_2, the W^{6+} species were regenerated. The XPS spectrum for W^{6+} species was similar to that obtained before CH_4 treatment, confirming the re-oxidation of the reduced W species by CO_2. Reduction of W in $Ni/WO_3(10)/Al_2O_3$ by CH_4 dominantly afforded W^{5+} species, whereas the reduction of W species in Ni/WO_3 was not observed. The reduction of the W in $Ni/WO_3(10)/ZrO_2$ was also supported by the XPS spectra in the W 4d region (data not shown).

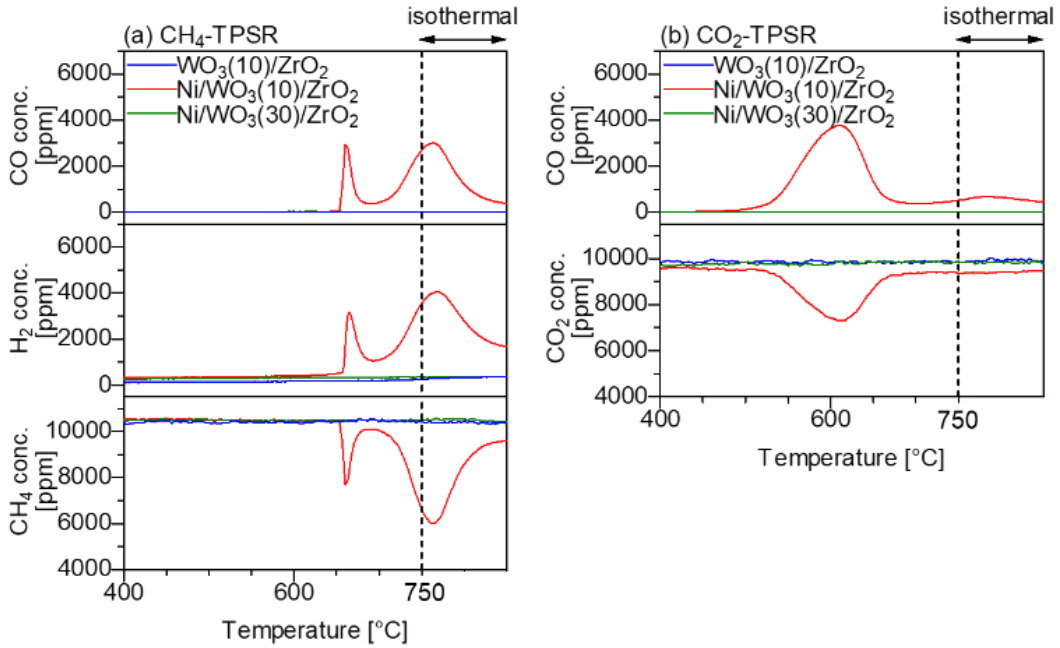

Figure 8. (a) CH_4-TPSR profiles. Conditions: 40 mg material, 100 mL/min of 1% CH_4/He, temperature rise

of 20 °C/min (from 50 to 750 °C). (b) CO_2-TPSR profiles. Conditions: 40 mg material, 100 mL/min of 1% CO_2/He, temperature rise of 20 °C/min (from 50 to 750 °C).

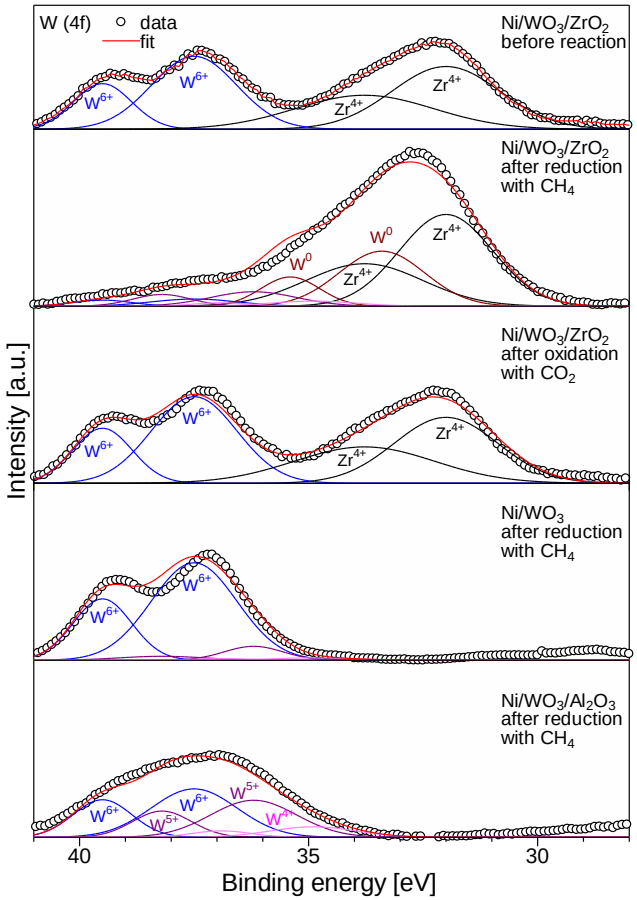

Figure 9. W 4f XPS spectra of Ni/WO_3(10)/ZrO_2 before reaction, after reduction with CH_4, after oxidation with CO_2, Ni/WO_3 and Ni/WO_3(10)/Al_2O_3 after reduction with CH_4. Reaction temperature is 750ºC. All measurements on the CH_4-treated materials were performed without exposure to air.

5.3. *In situ*/*operando* XANES study of Ni/WO_3(10)/ZrO_2 during CL-DRM

In situ W L_3-edge EXAFS Fourier transform (FT) spectra of Ni/WO_3(10)/ZrO_2 were analyzed to obtain the information of local structure of tungstate species. Note that the ubiquitous presence of Hf impurities in ZrO_2 limit the extent of EXAFS analysis, and thus the discussion of EXAFS spectra of WO_3/ZrO_2 catalysts is qualitative [65,66]. The EXAFS FT spectrum of He-treated Ni/WO_3(10)/ZrO_2 (before CL-DRM reaction) showed the main scattering peak at approximately 1.4 Å (uncorrected for phase-shift) with small peaks around 2.5–3.5 Å (Figure 12). The former peak is ascribed to W–O shell similar to the one of WO_3 whereas the latter peaks are assignable to W–Zr contributions resulting from anchorage of tungstate species on ZrO_2 support (approximately 2.7 Å) and/or W–W contributions of edge-sharing WO_6 units unique to polytungstate species (approximately 3.2 Å) [65]. Longer-distance W–W contributions of corner-sharing WO_6 units unique to bulk WO_3 (approximately 3.7 Å) were hardly observed. These observations indicated the dispersed tungstate species were

dominant and that crystalline WO_3 species were scarcely formed even at 750 °C. After the reaction with CH_4, the peak corresponding to W–O shell disappeared and a new peak assignable to other W–O shell similar to the one of low-valent W oxides (WO_2) appeared at approximately 1.7 Å. When the CH_4-treated sample was successively reacted with CO_2, the spectrum returned to the one obtained before the reaction and longer-distance W–W contributions of crystalline WO_3 were hardly observed, indicating that dispersed tungstate species was recovered by the reaction by CO_2.

In situ W L_1-edge XANES measurements were further performed for Ni/WO_3(10)/ZrO_2. Under the He flow at 750 °C, the XANES spectrum showed the absorption edge similar that for WO_3 and the stronger pre-edge peak compared to that of WO_3 (Figure 13). The pre-edge peak is assigned to the transition from 2s to d-p orbitals, and its intensity increases with decrease of the symmetry of tungstate species[39,43,67]. Tetrahedral W units show large pre-edge peaks intensity while octahedral W units exhibit small one. Moderate pre-edge peaks are observed for distorted octahedral W units. The larger pre-edge peak for Ni/WO_3(10)/ZrO_2 indicates that less symmetric W units exist over for Ni/WO_3(10)/ZrO_2 compared to WO_3. In the XANES spectrum after the re-oxidation with CO_2, both the absorption edge and pre-edge were almost same as those before the reaction with CH_4, supporting that the original tungstate species were recovered. Regarding the oxidation state after the reaction with CH_4, the absorption edge shifted toward lower energy value where the energy at normalized adsorption of 0.5 was present between WO_2 (W^{4+}) and W foil (W^0), which also showed the formation of low-valent W species, consisting with the observation in XPS and W L_3-edge XAS measurements.

In situ Ni K-edge XANES measurements were performed to investigate the state of the Ni species during CL-DRM (Figure 14). During CH_4 flow, the absorption edge for Ni/WO_3(10)/ZrO_2 and Ni/WO_3(30)/ZrO_2 shifted to lower energies (Figures 14a and 14b). When the gas was changed from CH_4 to CO_2, the absorption edge returned to a higher value. In contrast, the XANES spectra for Ni/WO_3(10)/Al_2O_3 and Ni/WO_3 remained unchanged under CH_4 flow (Figures 14c and 14d). *In situ* Zr K-edge XANES measurements were performed for Ni/WO_3(10)/ZrO_2 and WO_3(10)/ZrO_2 during the CL-DRM (Figure 15). For both materials, the edge positions did not change markedly by treatments with CH_4 and CO_2. Summarizing the results of *operando*/*in situ* W L_3-/L_1-, Ni K-, and Zr K-edge XANES and other spectroscopic results, it is concluded that the CL-DRM occurs because of the redox reaction of tungstate species in Ni/WO_3(10)/ZrO_2 and the dispersed tungstate species on ZrO_2 are

specifically reduced under CH_4 flow in the co-presence of Ni species.

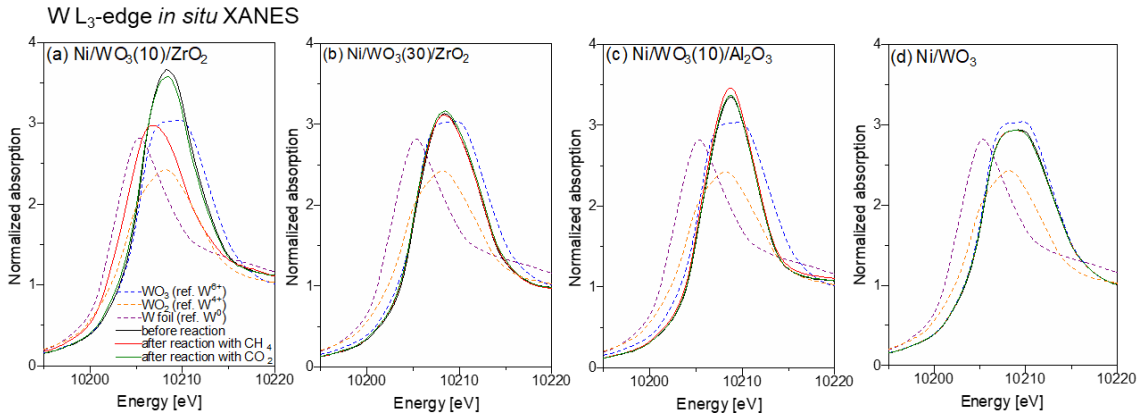

Figure 10. W L_3-edge *in situ* XANES spectra of (a) $Ni/WO_3(10)/ZrO_2$, (b) $Ni/WO_3(30)/ZrO_2$, (c) $Ni/WO_3(10)/Al_2O_3$, and (d) Ni/WO_3 at 750 °C before and after the successive flow of 1% CH_4/He (10 min) and then 1% CO_2/He (10 min).

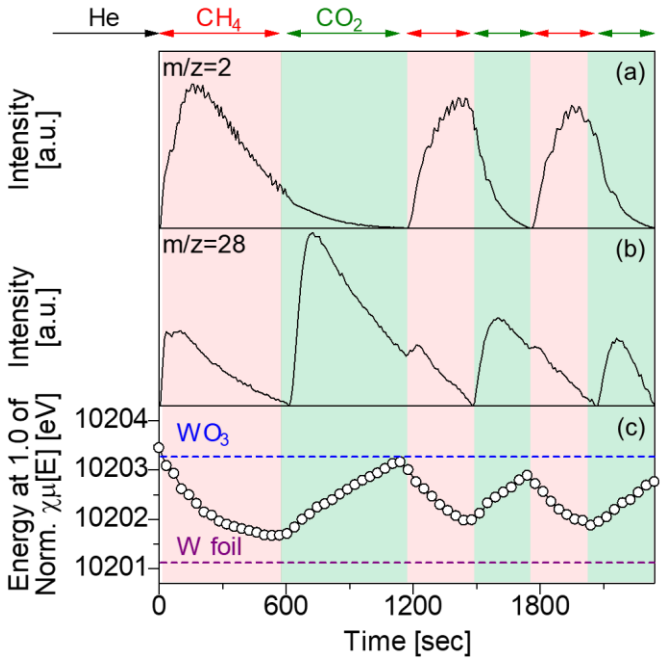

Figure 11. *Operando* W-L_3 edge XANES results for $Ni/WO_3(10)/ZrO_2$ at 750 °C under flowing of 1% CH_4/He or 1% CO_2/He (100 mL/min). MS signals for (a) H_2 and (b) CO, and (c) energy at the normalized adsorption of 1.0 in XANES spectra ($E_{1.0}$). The flowing gas was successively changed from CH_4 (10 min) to CO_2 (9.5 min), and then CH_4/CO_2 cycles were repeated every 5 min.

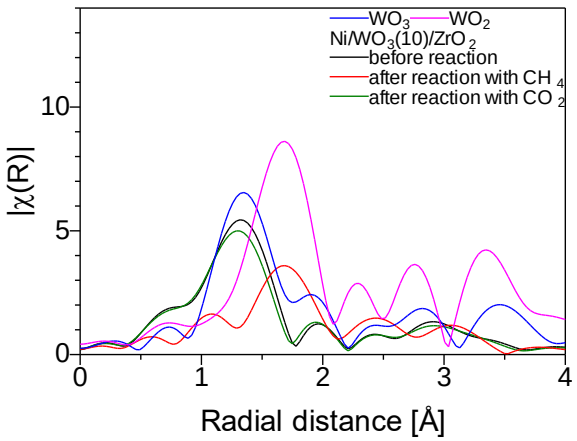

Figure 12. *In situ* W L_3-edge EXAFS FT spectra of $Ni/WO_3(10)/ZrO_2$ at 750 °C before and after successive flow of 1% CH_4/He (10 min) and then 1% CO_2/He (10 min).

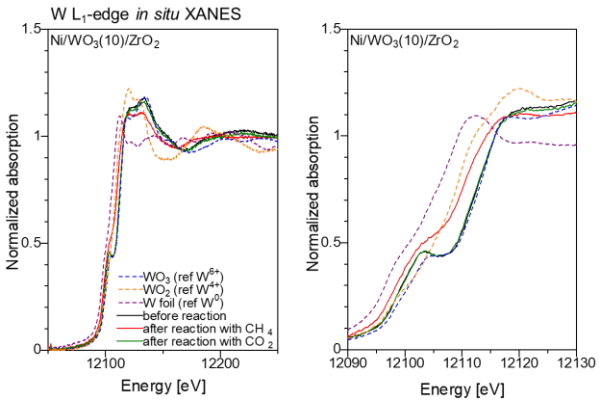

Figure 13. W L_1-edge *in situ* XANES spectra of $Ni/WO_3(10)/ZrO_2$ before and after the successive flow of 1% CH_4/He (10 min) and then 1% CO_2/He (10 min). For clarity, enlarged spectra are presented in the right panel.

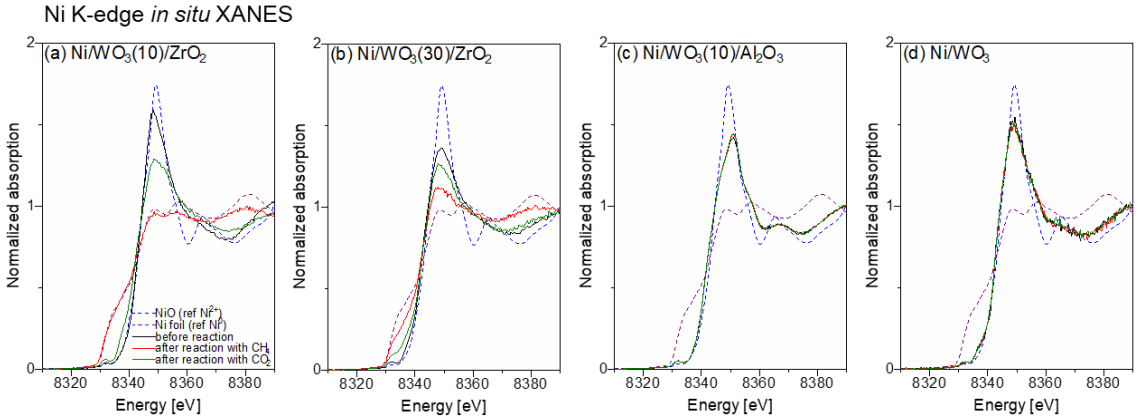

Figure 14. Ni K-edge *in situ* XANES spectra of (a) $Ni/WO_3(10)/ZrO_2$, (b) $Ni/WO_3(30)/ZrO_2$, (c) $Ni/WO_3(10)/Al_2O_3$, and (d) Ni/WO_3 at 750 °C before and after the successive flow of 1% CH_4/He (10 min) and 1% CO_2/He (10 min).

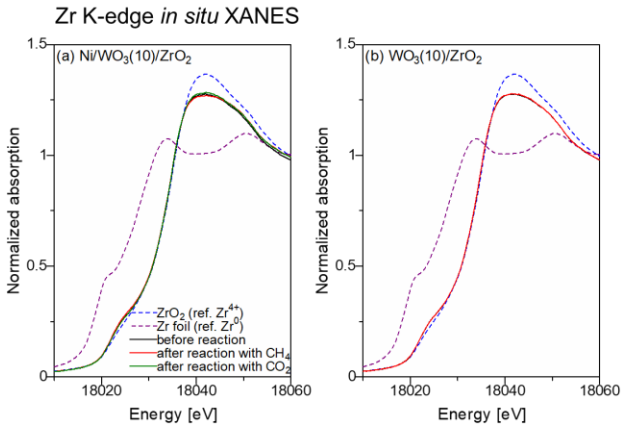

Figure 15. Zr K-edge *in situ* XANES spectra of (a) Ni/WO_3(10)/ZrO_2, and (b) WO_3(10)/ZrO_2 at 750 °C before and after the successive flow of 1% CH_4/He (10 min) and 1% CO_2/He (10 min).

5.3.4 Cooperative work of dispersed tungstate species and Ni on ZrO_2 in CL-DRM

Based on the results obtained in CL-DRM tests and characterizations, dispersed tungstate species on ZrO_2 serve as active oxygen storage sites in CL-DRM and work cooperatively with Ni species to promote POM to form CO and H_2. In this paragraph, the details of cooperative work including possible roles of Ni and ZrO_2 are discussed. To compare the reactivity for CH_4 between tungstate and Ni species, the CH_4-TPSR experiments were performed using Ni/ZrO_2 and $WO_3(10)/ZrO_2$ with elevating the temperature to 900 °C (Figure 17). Although a very small amount of CH_4 consumption was observed around 650 °C, CH_4 was largely consumed above 800 °C in the TPSR profile for Ni/ZrO_2. In higher temperature region, H_2 was concomitantly formed with CH_4 consumption but CO formation was hardly observed. When $WO_3(10)/ZrO_2$ was used, CO and H_2 were gradually generated with the CH_4 consumption above 750 °C. These results showed that dispersed tungstate species are main active sites for POM rather than Ni species. In the screening of metal oxide supports, reducible metal oxides (ZrO_2 and TiO_2) are effective supports whereas non-reducible ones (Al_2O_3, SiO_2, and MgO) were inactive (Table 1), showing that metal oxide supports also play a key role in CL-DRM. A possible role of ZrO_2 is the promotion of POM to CO and H_2 *via* reverse hydrogen spillover mechanism [19,68]. To examine the hydrogen spillover characteristics of ZrO_2 in this reaction system, a physical mixture of Ni/ZrO_2 and $WO_3(10)/ZrO_2$ was used for CH_4-TPSR and CL-DRM. In the TPSR, CH_4 consumption and CO/H_2 formation peaks were observed above 700 °C where the profiles were similar to those for $Ni/WO_3(10)/ZrO_2$ (Figure 17). In the CL-DRM, the substantial amount of CO was formed (1.12 mmol/g) using the physical mixture whereas the use of Ni/ZrO_2 or $WO_3(10)/ZrO_2$ independently yielded the very small amount of CO (0.19 and 0.14 mmol/g, respectively, Table 1). These control experiments using the physical mixture suggest that the hydrogen species that generated by POM are transferred from the surface of $WO_3(10)/ZrO_2$ to the one of Ni/ZrO_2 [69]. From the above results, a cooperative work of dispersed tungstate species and Ni over ZrO_2 in POM can be explained below, dispersed tungstate species serve as main active sites to promote the oxidation of CH_4, giving CO and surface hydrogen species. The generated hydrogen species spills over onto ZrO_2 surface to migrate to Ni species where the recombination of hydrogen species and successive desorption of H_2 occur [19]. Possible key roles of ZrO_2 and supported Ni species are the promotion of POM *via* reverse hydrogen spillover mechanism and the recombination of hydrogen species, respectively, which enable almost all of the dispersed tungstate species to be involved into CL-DRM as active oxygen storage sites. In the context of CO_2 reduction step, the reduced W species were re-oxidized

with concomitant formation of CO, as revealed by *operando* W L_3-edge XAS measurement. Even though metallic Ni species was also re-oxidized, the loading amount was quite low, which made the involvement of Ni as reduction sites negligible. The previous ZrO_2 or Al_2O_3-supported WO_3 materials for CL-type POM were prepared with high WO_3 loading amount (30–50 wt%), resulting in the formation of crystalline WO_3 phase detectable by XRD. Their application for CL-type POM and redox reactions were thus limited to high reaction temperature conditions (900–1000 ºC)[52–54]. The present study demonstrated the lower temperature CL-type POM (750 °C) using WO_3-based materials by (1) controlling dispersion of surface tungstate species (active oxygen storage sites), (2) utilizing reducible ZrO_2 supports (reverse hydrogen spillover), and (3) modifying with Ni (recombination sites of surface hydrogen species).

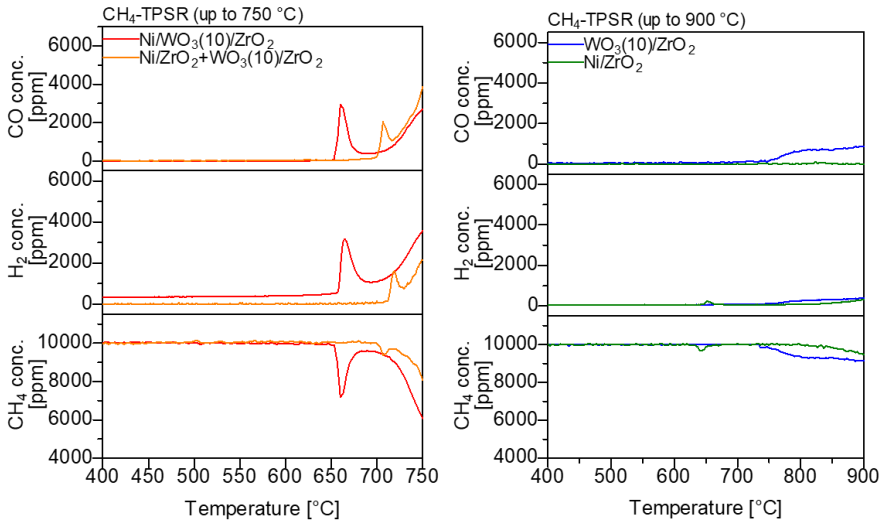

Figure 17. CH_4-TPSR profiles for $Ni/WO_3(10)/ZrO_2$, Ni/ZrO_2, $WO_3(10)/ZrO_2$, and a physical mixture of Ni/ZrO_2 and $WO_3(10)/ZrO_2$. Conditions: 40 mg material, 100 mL/min of 1% CH_4/He, temperature rise of 20 °C/min (from 50 to 750 or 900 °C).

5.3.5 Long-term CL-DRM over $Ni/WO_3(10)/ZrO_2$

Recently, Goula et al. studied the conventional (steady-state) DRM reaction at 750 °C using ZrO_2 materials loaded with Ni and WO_3 and reported that the conversion of CH_4 and CO_2 decreased with increasing reaction time[70]. In this study, we performed a long-term CL-DRM reaction using $Ni/WO_3(10)/ZrO_2$ under a cyclic feed of 1% CH_4/He (2 min) and 1% CO_2/He (2 min) for 750 cycles. Long-term CL-DRM was performed for 50 h, whereas the accumulated time for CH_4 and CO_2 flows was 25 h. The reaction time is discussed in terms of the accumulated time for comparison with steady-state CL-DRM. The conversion values were calculated based on the concentration of the residual CH_4 and CO_2 in the effluent gas (for details of the calculation, refer to SI). The initial conversion values (circles in Figure 17) were approximately 51% and 50% for CH_4 and CO_2, respectively. After the initial decrease in conversion (from 50% to approximately 40% after 6 h), the conversion values remained unchanged for the next 18 h. The average concentration of generated CO in a single cycle was approximately 6000 ppm. The total cycle number in the present CL-DRM over $Ni/WO_3/ZrO_2$ is the highest among the previously reported CL-DRM systems (Table S2)[15–31]. In another conventional DRM experiment performed at 750 °C, 1% CH_4/1% CO_2/He continuously flowed over $Ni/WO_3(10)/ZrO_2$. Initially, more than 99% of CH_4 and CO_2 were converted in conventional DRM (squares in Figure 17); however, the conversions monotonically decreased with time. After 18 h, the conversion was below 20%. A monotonic decrease in the amount of CO formed was also observed (data not shown). The total CO formation amount in CL-DRM was calculated as 1.84 mol/g, which was higher than that in the steady-state DRM (0.79 mol/g).

The characterization of the spent $Ni/WO_3(10)/ZrO_2$ used in CL-DRM was conducted using XRD, N_2 adsorption, Raman spectroscopy, STEM and EDX. The XRD pattern did not contain any diffraction peak derived from bulk WO_3 or Ni species and showed the diffraction pattern of ZrO_2 similar to the one in fresh $Ni/WO_3(10)/ZrO_2$ (data not shown). The good specific surface area value was maintained (115 m^2/g), resulting in the low surface W density value (2.0 to 2.3 atoms/nm^2) even after the reaction (Table S3) while the peak shift of W=O ascribed to conversion of monotungstate species to polytungstate species was observed (data not shown). Although the small structural change was indicated, their aggregation into crystalline WO_3 species unlikely occurred during CL-DRM cycle. In STEM and EDX observations, the tungstate species maintained their dispersed state on ZrO_2 whereas nanosized Ni species were observed (data not shown), indicating that dispersed Ni species were aggregated during the reaction. Because hydrogen species generated around tungstate

species from CH_4 possibly spill over onto ZrO_2 surfaces, as discussed above, almost all of tungstate species are involved into CL-DRM even a large amount of tungstate specie are not close to nanosized Ni species. Temperature programmed oxidation (TPO) measurements were also performed for the $Ni/WO_3(10)/ZrO_2$ after long-term CL-DRM and steady-state DRM (data not shown). The TPO profiles showed that the relative formation amount of CO and CO_2 were higher for the sample after CL-DRM than the one after steady-state DRM. The N_2 adsorption measurement of the spent $Ni/WO_3(10)/ZrO_2$ after conventional DRM revealed that the specific surface area significant decreased (Table S3), which might be a possible reason of the loss of activity in conventional DRM.

Furthermore, the CL-DRM under higher concentration conditions (30% CH_4 and CO_2) was carried out using a higher amount of $Ni/WO_3(10)/ZrO_2$. Under a cyclic feed of 30% CH_4/He (2 min) and 30% CO_2/He (2 min) for 75 cycles, the conversion values of CH_4 and CO_2 monotonically decreased from approximately 80% to 40% for 5 h (data not shown). When the feed time of 30% CH_4/He was extended to 3 min, the decrease of CH_4 and CO_2 conversion values suppressed and were leveled off within 25 cycles (almost 2 h) where approximately 70% and 40% conversion were maintained for CH_4 and CO_2, respectively (Figure 18). The high CO selectivity (> 97%) and good H_2/CO ratio in POM step (approximately 2, after 25 cycles) were also obtained (data not shown). The CL-DRM in previously reported studies were performed under relatively low concentration conditions (Table S2). The developed $Ni/WO_3(10)/ZrO_2$ has potential to be applied to high-concentration CL-DRM reactions.

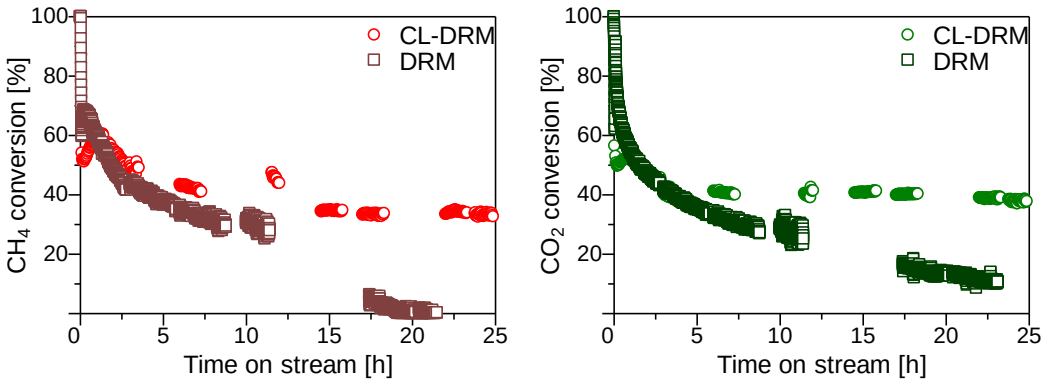

Figure 16. Time on stream of CH_4 conversion and CO_2 conversion in CL-DRM and conventional DRM using $Ni/WO_3/ZrO_2$ (40 mg) at 750 °C. For CL-DRM, 1% CH_4 (2 min)/1% CO_2 (2 min) cycle was repeated 750 times for 50 h. For DRM, 1% CH_4/1% CO_2 continuously flowed over the material for 25 h.

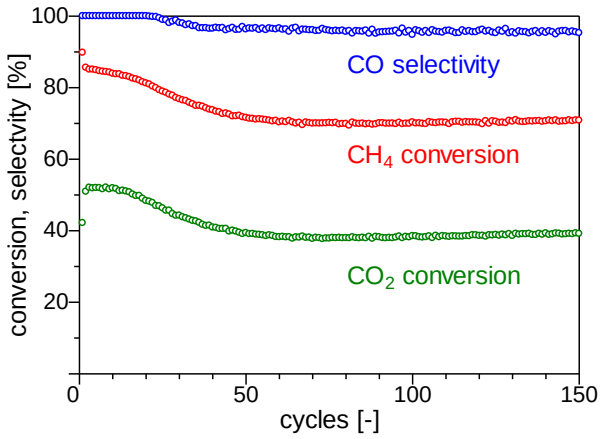

Figure 17. Time on stream of CH_4 conversion, CO_2 conversion, and CO selectivity in CL-DRM under high-concentration conditions. Reactions conditions: 2.5 g of $Ni/WO_3(10)/ZrO_2$. 750 °C, 50 mL/min flow rate. The GHSV value was approximately 1000 h^{-1}. 30% CH_4 (2 min)/30% CO_2 (3 min) cycle was repeated 180 cycles for 12 h.

5.4 Conclusions

In this study, we developed Ni/WO_3/ZrO_2 as an effective material for CL-DRM under isothermal conditions (750 °C). The performance of Ni/WO_3/ZrO_2 strongly depended on the WO_3 loading amount, and 10.0 wt% was the optimal WO_3 loading amount (Ni/WO_3(10)/ZrO_2). The combination of ZrO_2 and Ni was found to be ideal for CL-DRM. The Ni/WO_3(10)/ZrO_2 material exhibited good durability in long-term CL-DRM reactions and were applicable to high-concentration CL-DRM. Comprehensive characterization of a series of WO_3-loaded materials with different WO_3 loadings (6.2, 10.0, 19.5, and 30.0 wt%) and supports (ZrO_2 and Al_2O_3) showed that surface dispersed tungstate species on ZrO_2 function as active oxygen storage sites while dispersed tungstate species on Al_2O_3 or crystalline WO_3 species on ZrO_2 are inert even with Ni modification, demonstrating that low-loading WO_3/ZrO_2 materials uniquely serve as oxygen storage sites with Ni modification. ZrO_2 and Ni play key roles to promote CL-type POM step by reverse hydrogen spillover and re-combination of hydrogen species. The cooperative work of dispersed tungstate species with active metal for hydrogen recombination would be useful for catalyst design for oxidative upgrading of light alkanes including CH_4. XPS and *operando*/*in situ* XAS studies showed that the redox reaction of dispersed tungstate species between W^{6+} and $W^{0–3+}$ contributes to CL-DRM and that the dispersed state was maintained during the redox reaction.

5.5 References

(1) A. T. Ashcroft; A. K. Cheetham; M. L. H. Green; P. D. F. Vernon. Partial Oxidation of Methane to Synthesis Gas Using Carbon Dioxide. *Nature* **1991**, *352*, 225–226.

(2) Jang, W. J.; Shim, J. O.; Kim, H. M.; Yoo, S. Y.; Roh, H. S. A Review on Dry Reforming of Methane in Aspect of Catalytic Properties. *Catal. Today* **2019**, *324*, 15–26.

(3) Ruan, C.; Huang, Z. Q.; Lin, J.; Li, L.; Liu, X.; Tian, M.; Huang, C.; Chang, C. R.; Li, J.; Wang, X. Synergy of the Catalytic Activation on Ni and the CeO_2-TiO_2/$Ce_2Ti_2O_7$ Stoichiometric Redox Cycle for Dramatically Enhanced Solar Fuel Production. *Energy Environ. Sci.* **2019**, *12*, 767–779.

(4) Pakhare, D.; Spivey, J. A Review of Dry (CO_2) Reforming of Methane over Noble Metal Catalysts. *Chem Soc Rev*. **2014**, 22, 7813–7837.

(5) Álvarez, A.; Bansode, A.; Urakawa, A.; Bavykina, A. V.; Wezendonk, T. A.; Makkee, M.; Gascon, J.; Kapteijn, F. Challenges in the Greener Production of Formates/Formic Acid, Methanol, and DME by Heterogeneously Catalyzed CO_2 Hydrogenation Processes. *Chem Rev*. **2017**, 117, 9804–9838.

(6) Yang, H.; Xu, Z.; Fan, M.; Gupta, R.; Slimane, R. B.; Bland, A. E.; Wright, I. Progress in Carbon Dioxide Separation and Capture: A Review. *J. Environ. Sci.* **2008**, *20*, 14–27.

(7) Lahijani, P.; Zainal, Z. A.; Mohammadi, M.; Mohamed, A. R. Conversion of the Greenhouse Gas CO_2 to the Fuel Gas CO via the Boudouard Reaction: A Review. *Renew. Sustain. Energy Rev.* **2015**, *41*, 615–632.

(8) Sun, S.; Sun, H.; Williams, P. T.; Wu, C. Recent Advances in Integrated CO_2 capture and Utilization: A Review. *Sustain. Energy Fuels*. **2021**, 18, 4546–4559.

(9) Sternberg, A.; Jens, C. M.; Bardow, A. Life Cycle Assessment of CO_2-Based C1-Chemicals. *Green Chem.* **2017**, *19*, 2244–2259.

(10) Li, D.; Xu, R.; Gu, Z.; Zhu, X.; Qing, S.; Li, K. Chemical-Looping Conversion of Methane: A Review. *Energy Technol.* **2020**, *8*. 1900925.

(11) Zhu, X.; Imtiaz, Q.; Donat, F.; Müller, C. R.; Li, F. Chemical Looping beyond Combustion-a Perspective. *Energy Environ. Sci*. **2020**, 3, 772–804.

(12) Takanabe K. Catalytic Conversion of Methane:Carbon Dioxide Reforming and Oxidative Coupling. *J. Japan Pet. Inst.* **2012**, *55*, 1–12.

(13) Amin, A. M.; Croiset, E.; Epling, W. Review of Methane Catalytic Cracking for Hydrogen Production. *Int. J. Hydrogen Energy* **2011**, *36*, 2904–2935.

(14) Franz, R.; Pinto, D.; Uslamin, E. A.; Urakawa, A.; Pidko, E. A. Impact of Promoter Addition on the Regeneration of Ni/Al_2O_3 Dry Reforming Catalysts. *ChemCatChem* **2021**, *13*, 5034–5046.

(15) Jin, B.; Li, S.; Liu, Y.; Liang, X. Engineering Metal-Oxide Interface by Depositing ZrO_2 Overcoating on Ni/Al_2O_3 for Dry Reforming of Methane. *Chem. Eng. J.* **2022**, *436*, 135195.

(16) Zhang, M.; Zhang, J.; Zhang, Q.; Han, Y. Dry Reforming of Methane over the Ni/Y_2O_3-ZrO_2 Catalysts: Effects of the Tunable Surface Oxygen Species by Modulating the Zirconium Precursors. *Appl. Catal. A Gen.* **2022**, *639*, 118639.

(17) Georgiadis, A. G.; Siakavelas, G. I.; Tsiotsias, A. I.; Charisiou, N. D.; Ehrhardt, B.; Wang, W.; Sebastian, V.; Hinder, S. J.; Baker, M. A.; Mascotto, S.; Goula, M. A. Biogas Dry Reforming over Ni/LnOx-Type Catalysts (Ln = La, Ce, Sm or Pr). *Int. J. Hydrogen Energy* **2023**. (in press)

(18) Rudolph, B.; Tsiotsias, A. I.; Ehrhardt, B.; Dolcet, P.; Gross, S.; Haas, S.; Charisou, N. D.; Goula, M. A.; Mascotto, S. Nanoparticle Exsolution from Nanoporous Perovskites for Highly Active and Stable Catalysts. *Adv. Sci.* **2023**, *10*, 1–12.

(19) Otsuka, K.; Wang, Y.; Sunada, E.; Yamanaka, I. Direct Partial Oxidation of Methane to Synthesis Gas by Cerium Oxide. *J. Catal.* **1998**, *175*, 152–160.

(20) More, A.; Veser, G. Physical Mixtures as Simple and Efficient Alternative to Alloy Carriers in Chemical Looping Processes. *AIChE J.* **2017**, *63* (1), 51–59.

(21) Rydén, M.; Ramos, P. H_2 Production with CO_2 Capture by Sorption Enhanced Chemical-Looping Reforming Using NiO as Oxygen Carrier and CaO as CO_2 Sorbent. *Fuel Process. Technol.* **2012**, *96*, 27–36.

(22) Hu, J.; Galvita, V. V.; Poelman, H.; Detavernier, C.; Marin, G. B. Pressure-Induced Deactivation of Core-Shell Nanomaterials for Catalyst-Assisted Chemical Looping. *Appl. Catal. B Environ.* **2019**, *247*, 86–99.

(23) Zhao, Y.; Jin, B.; Liang, Z. Synergistic Enhanced Ca-Fe Chemical Looping Reforming Process for Integrated CO_2 Capture and Conversion. *Ind. Eng. Chem. Res.* **2020**, *59*, 1298–1307.

(24) Najera, M.; Solunke, R.; Gardner, T.; Veser, G. Carbon Capture and Utilization via Chemical Looping Dry Reforming. *Chem. Eng. Res. Des.* **2011**, *89*, 1533–1543.

(25) Zheng, Y.; Li, K.; Wang, H.; Tian, D.; Wang, Y.; Zhu, X.; Wei, Y.; Zheng, M.; Luo, Y. Designed Oxygen Carriers from Macroporous $LaFeO_3$ Supported CeO_2 for Chemical-Looping Reforming of Methane. *Appl. Catal. B Environ.* **2017**, *202*, 51–63.

(26) Zhang, L.; Xu, W.; Wu, J.; Hu, Y.; Huang, C.; Zhu, Y.; Tian, M.; Kang, Y.; Pan, X.; Su, Y.; Wang, J.; Wang, X. Identifying the Role of A-Site Cations in Modulating Oxygen Capacity of Iron-Based Perovskite for Enhanced Chemical Looping Methane-to-Syngas Conversion. *ACS Catal.* **2020**, *10*, 9420–9430.

(27) Xia, X.; Chang, W.; Cheng, S.; Huang, C.; Hu, Y.; Xu, W.; Zhang, L.; Jiang, B.; Sun, Z.; Zhu, Y.; Wang, X. Oxygen Activity Tuning via FeO_6 Octahedral Tilting in Perovskite Ferrites for Chemical Looping Dry Reforming of Methane. *ACS Catal.* **2022**, *12*, 7326–7335.

(28) Zhu, Y.; Jin, N.; Liu, R.; Sun, X.; Bai, L.; Tian, H.; Ma, X.; Wang, X. Bimetallic $BaFe_2MAl_9O_{19}$ (M = Mn, Ni, and Co) Hexaaluminates as Oxygen Carriers for Chemical Looping Dry Reforming of Methane. *Appl. Energy* **2020**, *258*, 114070

(29) Cheng, Z.; Zhang, L.; Jin, N.; Zhu, Y.; Chen, L.; Yang, Q.; Yan, M.; Ma, X.; Wang, X. Effect of Calcination Temperature on the Performance of Hexaaluminate Supported CeO_2 for Chemical Looping Dry Reforming. *Fuel Process. Technol.* **2021**, *218*, 106873.

(30) Guerrero-Caballero, J.; Kane, T.; Haidar, N.; Jalowiecki-Duhamel, L.; Löfberg, A. Ni, Co, Fe Supported on Ceria and Zr Doped Ceria as Oxygen Carriers for Chemical Looping Dry Reforming of Methane. *Catal. Today* **2019**, *333*, 251–258.

(31) Han, Y.; Tian, M.; Wang, C.; Kang, Y.; Kang, L.; Su, Y.; Huang, C.; Zong, T.; Lin, J.; Hou, B.; Pan, X.; Wang, X. Highly Active and Anticoke Ni/CeO_2 with Ultralow Ni Loading in Chemical Looping Dry Reforming via the Strong Metal-Support Interaction. *ACS Sustain. Chem. Eng.* **2021**, *9*, 17276–17288.

(32) Löfberg, A.; Kane, T.; Guerrero-Caballero, J.; Jalowiecki-Duhamel, L. Chemical Looping Dry Reforming of Methane: Toward Shale-Gas and Biogas Valorization. *Chem. Eng. Process. Process Intensif.* **2017**, *122*, 523–529.

(33) Miyazaki, S.; Li, Z.; Maeno, Z.; Toyao, T.; Ito, M.; Nakajima, Y.; Shimizu, K. I. Operando Ce K-Edge XANES Study of Low-Loading Ni/CeO_2 in Chemical Looping Dry Reforming of Methane. *Chem. Lett.* **2022**, *51*, 914–918

(34) Löfberg, A.; Guerrero-Caballero, J.; Kane, T.; Rubbens, A.; Jalowiecki-Duhamel, L. Ni/CeO_2 Based Catalysts as Oxygen Vectors for the Chemical Looping Dry Reforming of Methane for Syngas Production. *Appl. Catal. B Environ.* **2017**, *212*, 159–174.

(35) Das, S.; Ashok, J.; Bian, Z.; Dewangan, N.; Wai, M. H.; Du, Y.; Borgna, A.; Hidajat, K.; Kawi, S. Silica–Ceria Sandwiched Ni Core–Shell Catalyst for Low Temperature

Dry Reforming of Biogas: Coke Resistance and Mechanistic Insights. *Appl. Catal. B Environ.* **2018**, *230*, 220–236.

(36) Zhou, W.; Soultanidis, N.; Xu, H.; Wong, M. S.; Neurock, M.; Kiely, C. J.; Wachs, I. E. Nature of Catalytically Active Sites in the Supported WO_3/ZrO_2 Solid Acid System: A Current Perspective. *ACS Catal*. **2017**, 7, 2181–2198.

(37) Vance, B. C.; Kots, P. A.; Wang, C.; Hinton, Z. R.; Quinn, C. M.; Epps, T. H.; Korley, L. S. T. J.; Vlachos, D. G. Single Pot Catalyst Strategy to Branched Products via Adhesive Isomerization and Hydrocracking of Polyethylene over Platinum Tungstated Zirconia. *Appl. Catal. B Environ.* **2021**, *299*, 120483.

(38) Shi, D.; Wang, H.; Kovarik, L.; Gao, F.; Wan, C.; Hu, J. Z.; Wang, Y. WOx Supported on γ-Al_2O_3 with Different Morphologies as Model Catalysts for Alkanol Dehydration. *J. Catal.* **2018**, *363*, 1–8.

(39) Aihara, T.; Miura, H.; Shishido, T. Effect of Perimeter Interface Length between 2D WO_3 Monolayer Domain and γ-Al_2O_3 on Selective Hydrogenolysis of Glycerol to 1,3-Propanediol. *Catal. Sci. Technol.* **2019**, *9*, 5359–5367.

(40) Sudarsanam, P.; Gupta, N. K.; Mallesham, B.; Singh, N.; Kalbande, P. N.; Reddy, B. M.; Sels, B. F. Supported MoOx and WOx Solid Acids for Biomass Valorization: Interplay of Coordination Chemistry, Acidity, and Catalysis. *ACS Catal.* **2021**, *11*, 13603–13648.

(41) Baertsch, C. D.; Soled, S. L.; Iglesia, E. Isotopic and Chemical Titration of Acid Sites in Tungsten Oxide Domains Supported on Zirconia. *J. Phys. Chem. B* **2001**, *105*, 1320–1330.

(42) Zhou, W.; Ross-Medgaarden, E. I.; Knowles, W. V.; Wong, M. S.; Wachs, I. E.; Kiely, C. J. Identification of Active Zr–WOx Clusters on a ZrO_2 Support for Solid Acid Catalysts. *Nat. Chem.* **2009**, *1*, 722–728.

(43) Kitano, T.; Hayashi, T.; Uesaka, T.; Shishido, T.; Teramura, K.; Tanaka, T. Effect of High-Temperature Calcination on the Generation of Brønsted Acid Sites on WO_3/Al_2O_3. *ChemCatChem* **2014**, *6*, 2011–2020.

(44) Cortés-Jácome, M. A.; Angeles-Chavez, C.; López-Salinas, E.; Navarrete, J.; Toribio, P.; Toledo, J. A. Migration and Oxidation of Tungsten Species at the Origin of Acidity and Catalytic Activity on WO_3-ZrO_2 Catalysts. *Appl. Catal. A Gen.* **2007**, *318*, 178–189.

(45) Triwahyono, S.; Yamada, T.; Hattori, H. IR Study of Acid Sites on WO_3-ZrO_2. *Appl.*

Catal. A Gen. **2003**, *250*, 75–81.

(46) Aihara, T.; Kobayashi, H.; Feng, S.; Miura, H.; Shishido, T. Effect of WO_3 Loading on the Activity of $Pt/WO_3/Al_2O_3$ Catalysts in Selective Hydrogenolysis of Glycerol to 1, 3-Propanediol. *Chem. Lett.* **2017**, *46*, 1497–1500

(47) Occhiuzzi, M.; Cordischi, D.; Gazzoli, D.; Valigi, M.; Heydorn, P. C. WOx/ZrO_2 Catalysts Part 4. Redox Properties as Investigated by Redox Cycles, XPS and EPR. *Appl. Catal. A Gen.* **2004**, *269*, 169–177.

(48) Aihara, T.; Miura, H.; Shishido, T. Investigation of the Mechanism of the Selective Hydrogenolysis of C-O Bonds over a $Pt/WO_3/Al_2O_3$ Catalyst. *Catal. Today* **2020**, *352*, 73–79.

(49) Hadjiivanov, K.; Lukinskas, P.; Knözinger, H. Detection of Reduced Wn+ Sites on WO_3-ZrO_2 and Pt/WO_3-ZrO_2 Catalysts by Infrared Spectroscopy of Adsorbed NO. *Catal. Letters* **2002**, *82*, 73–77.

(50) Yuan, K.; Yamazaki, Y.; Jin, X.; Nozaki, K. Multifunctional WO_3-ZrO_2-Supported Platinum Catalyst for Remarkably Efficient Hydrogenolysis of Esters to Alkanes. *J. Am. Chem. Soc.* **2023**. 145, 3454-3461.

(51) Aihara, T.; Asazuma, K.; Miura, H.; Shishido, T. Highly Active and Durable WO_3/Al_2O_3 catalysts for Gas-Phase Dehydration of Polyols. *RSC Adv.* **2020**, *10*, 37538–37544.

(52) Kodama, T.; Shimizu, T.; Satoh, T.; Shimizu, K. I. Stepwise Production of CO-Rich Syngas and Hydrogen via Methane Reforming by a WO_3-Redox Catalyst. *Energy* **2003**, *28*, 1055–1068

(53) Kwak, J. H.; Han, G. Y.; Bae, J. W.; Yoon, K. J. Tungsten Oxides Supported on Nano-Size Zirconia for Cyclic Production of Syngas and Hydrogen by Redox Operations. *Korean J. Chem. Eng.* **2014**, *31*, 961–971

(54) Shimizu, T.; Shimizu, K.; Kitayama, Y.; Kodama, T. Thermochemical Methane Reforming Using WO_3 as an Oxidant below 1173 K by a Solar Furnace Simulator. *Sol. Energy* **2001**, *71*, 315–324.

(55) Chen, S.; Zeng, L.; Tian, H.; Li, X.; Gong, J. Enhanced Lattice Oxygen Reactivity over Ni-Modified WO_3-Based Redox Catalysts for Chemical Looping Partial Oxidation of Methane. *ACS Catal.* **2017**, *7*, 3548–3559

(56) Al-Fatesh, A. S.; Golaviya, J.; Shrivastava, V. K.; Ibrahim, A. A.; Osman, A. I.; Fakeeha, A. H.; Abasaeed, A. E.; Bagabas, A. A.; Lanre, M. S.; Kumar, R.; Hussain, A.; Lin, K. S. A Highly Active and Cost-Effective Tungsten Modified Ni-Based Catalyst for the Production of Hydrogen via Methane Dry Reforming. *Catal. Commun.* **2022**,

171, 106510.

(57) Bayahia, H.; Fakeeha, A. H.; Al-Zahrani, S. A.; Alreshaidan, S. B.; Al-Awadi, A. S.; Alotibi, M. F.; Kumar, R.; Al-Fatesh, A. S. COx -Free H_2 Production via Catalytic Decomposition of CH_4 over Fe Supported on Tungsten Oxide-Activated Carbon Catalyst: Effect of Tungsten Loading. *Arab. J. Chem.* **2023**, *16*, 104781.

(58) Ravel, B.; Newville, M. ATHENA, ARTEMIS, HEPHAESTUS: Data Analysis for X-Ray Absorption Spectroscopy Using IFEFFIT. *Journal of Synchrotron Radiation*. **2005**, 12, 537–541.

(59) Kim, T.; Burrows, A.; Kiely, C. J.; Wachs, I. E. Molecular/Electronic Structure-Surface Acidity Relationships of Model-Supported Tungsten Oxide Catalysts. *J. Catal.* **2007**, *246*, 370–381.

(60) Ross-Medgaarden, E. I.; Knowles, W. V.; Kim, T.; Wong, M. S.; Zhou, W.; Kiely, C. J.; Wachs, I. E. New Insights into the Nature of the Acidic Catalytic Active Sites Present in ZrO_2-Supported Tungsten Oxide Catalysts. *J. Catal.* **2008**, *256*, 108–125.

(61) Patel, R.; Al-Fatesh, A. S.; Fakeeha, A. H.; Arafat, Y.; Kasim, S. O.; Ibrahim, A. A.; Al-Zahrani, S. A.; Abasaeed, A. E.; Srivastava, V. K.; Kumar, R. Impact of Ceria over WO_3–ZrO_2 Supported Ni Catalyst towards Hydrogen Production through Dry Reforming of Methane. *Int. J. Hydrogen Energy* **2021**, *46*, 25015–25028.

(62) Al-Fatesh, A. S.; Patel, R.; Srivastava, V. K.; Ibrahim, A. A.; Naeem, M. A.; Fakeeha, A. H.; Abasaeed, A. E.; Alquraini, A. A.; Kumar, R. Barium-Promoted Yttria-Zirconia-Supported Ni Catalyst for Hydrogen Production via the Dry Reforming of Methane: Role of Barium in the Phase Stabilization of Cubic ZrO_2. *ACS Omega* **2022**. 7, 16468-16483.

(63) Al-Fatesh, A. S.; Khatri, J.; Kumar, R.; Kumar Srivastava, V.; Osman, A. I.; AlGarni, T. S.; Ibrahim, A. A.; Abasaeed, A. E.; Fakeeha, A. H.; Rooney, D. W. Role of Ca, Cr, Ga and Gd Promotor over Lanthana-Zirconia–Supported Ni Catalyst towards H_2-Rich Syngas Production through Dry Reforming of Methane. *Energy Sci. Eng.* **2022**, *10*, 866–880.

(64) Lin, F.; Li, C. P.; Chen, G.; Tenent, R. C.; Wolden, C. A.; Gillaspie, D. T.; Dillon, A. C.; Richards, R. M.; Engtrakul, C. Low-Temperature Ozone Exposure Technique to Modulate the Stoichiometry of WOx Nanorods and Optimize the Electrochromic Performance. *Nanotechnology* **2012**, *23*, 255601.

(65) Carrier, X.; Marceau, E.; Carabineiro, H.; Rodríguez-González, V.; Che, M. EXAFS Spectroscopy as a Tool to Probe Metal-Support Interaction and Surface Molecular

Structures in Oxide-Supported Catalysts: Application to Al_2O_3-Supported Ni(Ii) Complexes and ZrO_2- Supported Tungstates. *Phys. Chem. Chem. Phys.* **2009**, *11*, 7527–7539.

(66) Barton, D. G.; Soled, S. L.; Meitzner, G. D.; Fuentes, G. A.; Iglesia, E. *Structural and Catalytic Characterization of Solid Acids Based on Zirconia Modified by Tungsten Oxide*. *J Catal.* **1999**, 181, 57-72.

(67) Yamazoe, S.; Hitomi, Y.; Shishido, T.; Tanaka, T. XAFS Study of Tungsten L_1- And L_3-Edges: Structural Analysis of WO_3 Species Loaded on TiO_2 as a Catalyst for Photo-Oxidation of NH_3. *J. Phys. Chem. C* **2008**, *112*, 6869–6879.

(68) Shun, K.; Mori, K.; Masuda, S.; Hashimoto, N.; Hinuma, Y.; Kobayashi, H.; Yamashita, H. Revealing Hydrogen Spillover Pathways in Reducible Metal Oxides. *Chem. Sci.* **2022**, *13*, 8137–8147.

(69) Nakagawa, Y.; Tazawa, S.; Wang, T.; Tamura, M.; Hiyoshi, N.; Okumura, K.; Tomishige, K. Mechanistic Study of Hydrogen-Driven Deoxydehydration over Ceria-Supported Rhenium Catalyst Promoted by Au Nanoparticles. *ACS Catal.* **2018**, *8*, 584–595.

(70) Charisiou, N. D.; Siakavelas, G.; Papageridis, K. N.; Baklavaridis, A.; Tzounis, L.; Goula, G.; Yentekakis, I. V.; Polychronopoulou, K.; Goula, M. A. The Effect of WO_3 Modification of ZrO_2 Support on the Ni-Catalyzed Dry Reforming of Biogas Reaction for Syngas Production. *Front. Environ. Sci.* **2017**, *5*, 1–13.

Chapter 5

General conclusion

In this thesis, the author described the studies on the unsteady–state catalytic systems for direct CO_2 capture and reduction. General conclusions are summarized as follows.

In **Chapter 1**, unsteady–state catalytic systems for direct CO_2 capture and reduction.

In **Chapter 2**, I successfully developed Pt-Na/Al_2O_3 as an effective DFM for selective CO formation through CCR at a mild reaction temperature (350 °C). Among the basic promoters tested, Na was the best for CO formation, whereas Mg resulted in the lowest CO selectivity. Notably, the optimized Pt-Na/Al_2O_3 was applicable for continuous CCR operation, where CO_2 capture capacity and CO productivity were maintained for at least 100 h. We also conducted a comprehensive characterization of Pt, Pt-Na, and Pt-Mg/Al_2O_3 using microscopic (STEM and EDX) and spectroscopic (XRD, XAS, XPS, and FTIR) techniques. The Na-modified Pt NPs were formed in Pt-Na/Al_2O_3, whereas the Mg species remained in a highly dispersed state on Al_2O_3 in Pt-Mg/Al_2O_3. The electronic states of the Pt NPs were slightly affected by basic promoters regardless of whether or not modified structures had formed. We also conducted *in situ* FTIR measurements during CCR, where the adsorbed CO species were hardly observed over Pt-Na/Al_2O_3. The Na
species on Pt NPs not only served as CO_2 absorption sites but also suppressed the adsorption of generated CO, leading to high selectivity for CO. These results reveal the effect of basic promoters on the surface structures of metal NPs and product selectivity, demonstrating the importance of the choice and loading of basic promoters during the development of DFMs for CCR. Unfortunately, CO productivity of the present DFM system decreased in the presence of steam, although high CO selectivity was retained. Several important challenges, including inhibition by steam and application for higher CO_2 concentration, still remain in CCR over DFMs.

In **Chapter 3**, Herein, I revealed the mechanism of the CCR of CH_4 over Ni-Ca based DFMs using various *in situ* and *operando* spectroscopic studies. Under O_2-free conditions, only a small part of the Ni^0 species was oxidized by CO_2 during the CO_2 storage step, whereas a part of the bulk CaO reacted with CO_2 to yield bulk $CaCO_3$ layers
on CaO. In the subsequent H_2-reduction step, the bulk $CaCO_3$ was reduced by H_2 to yield CaO and gas-phase products (CH_4 and H_2O). In the presence of O_2 during the CO_2 capture step, the Ni^0 species underwent complete oxidation by O_2 to yield NiO, followed by CO_2 capture via the interaction between the CaO surface and CO_2 to yield $CaCO_3$ layers on the CaO particles. When the gas flow was switched to H_2, NiO was partially reduced by H_2 to provide Ni^0 sites, which served as active sites for the H_2-reduction of adjacent $CaCO_3$ layers to yield CaO and gas-phase products, CH_4 and H_2O.

In **Chapter 4**, I developed a new method for the continuous production of O_2-free CO_2, CH_4, and CO from the atmosphere and a simulated exhaust gas (CO_2/O_2/He mixture). The developed process is suitable for continuous operation over a low-temperature swing of 40–200 °C on a Rb-beta sorbent combined with a methanation system at 300 °C and a RWGS system (for syngas synthesis) at 650 °C. The results of this study revealed that the developed process is almost twice as effective as CCR for CO_2 capture and hydrogenation. We also provided evidence that the energy efficiency of the tandem methanation process based on the overall energy input and output is comparatively high because of the low power input required to operate the system and the high CH_4 production. This approach is promising for CO_2 utilization via direct air and post-combustion gas capture and conversion to green fuels. In the future, we expect that our flexible process, in combination with efficient catalysts, will contribute to a carbon-neutral society.

In **Chapter 5**, I successfully developed Ni/WO_3/ZrO_2 as an effective material for CL-DRM under isothermal conditions (750 °C). The performance of Ni/WO_3/ZrO_2 strongly depended on the WO_3 loading amount, and 10.0 wt% was the optimal WO_3 loading amount (Ni/WO_3(10)/ZrO_2). The combination of ZrO_2 and Ni was found to be ideal for CL-DRM. The Ni/WO_3(10)/ZrO_2 material exhibited good durability in longterm CL-DRM reactions and was applicable to high-concentration CL-DRM. Comprehensive characterization of a series of WO_3-loaded materials with different WO_3 loadings (6.2, 10.0, 19.5, and 30.0 wt%) and supports (ZrO_2 and Al_2O_3) showed that surface dispersed tungstate species on ZrO_2 function as active oxygen storage sites while dispersed tungstate species on Al_2O_3 or crystalline WO_3 species on ZrO_2 are inert even with Ni modification, demonstrating that low-loading WO_3/ZrO_2 materials uniquely serve as oxygen storage sites with Ni modification. ZrO_2 and Ni play key roles to promote the CL-type POM step by reverse hydrogen spillover and recombination of hydrogen species. The cooperative work of dispersed tungstate species with active metal for hydrogen recombination would be useful for catalyst design for oxidative upgrading of light alkanes including CH_4. XPS and *operando*/*in situ* XAS studies showed that the redox reaction of dispersed tungstate species between W^{6+} and W^{0-3+} contributes to CL-DRM and that the dispersed state was maintained during the redox reaction.

Throughout all the studies, this thesis highlights the significance of designing advanced catalytic systems for efficient CO_2 capture and utilization, based on mechanism suggested by *operando* spectroscopies. The findings demonstrate the crucial role of promoters, supports, and active site interactions in determining the performance of catalytic

systems under various operating conditions. Key achievements include the development of novel DFMs for selective CO and CH_4 production, the elucidation of mechanisms behind unsteady-state CO_2 hydrogenation, and the innovative application of chemical looping techniques for reforming and oxidation processes. These insights not only contribute to the fundamental understanding of unsteady-state catalysis but also provide practical solutions for advancing carbon-neutral technologies. By leveraging these results, the thesis underscores the potential of heterogeneous catalysis to address global challenges in sustainable energy and environmental management.

Acknowledgment

The present thesis is the summary of the author's work carried out during Master and Doctor course at Institute for Catalysis, Hokkaido University.

I greatly appreciate Prof. Dr. Kenichi Shimizu for his great support. I couldn't complete the thesis without his great advice and support. I never forget his kindness.

I greatly appreciate Prof. Dr. Zen Maeno for his daily support and valuable encouragement. His kind and sincere advice make me to be a researcher. I remember his valuable comment for the future.

I also appreciate Prof. Dr. Takashi Toyao for his great help to complete this work. I could always discuss with him thanks to his kindness to give me a time for discussion.

I also appreciate Dr. Akihiko Anzai for his daily support. His valuable encouragement gives me the power to make the thesis. I never forget his kindness.

I would like to be thankful to Prof. Dr. Shinya Furukawa, Dr. Shunsaku Yasumura, Dr. Shinya Mine Dr. Kenichi Kon and Mr. Wataru Onodera for their kindness in assisting this thesis and invaluable suggestion and the great help to complete this work.
I also would like to thank all other members of Prof. Shimizu's laboratory.

Finally, I would like to express my best regards to my family for their kind support, understanding and encouragement.

Shinta Miyazaki